Modeling interstellar bubbles: near and far

Silvia Verdolini

Modeling interstellar bubbles: near and far

Proefschrift

ter verkrijging van
de graad van Doctor aan de Universiteit Leiden,
op gezag van Rector Magnificus prof.mr. C.J.J.M. Stolker,
volgens besluit van het College voor Promoties
te verdedigen op donderdag 20 februari 2014
klokke 13.45 uur

door

Silvia Verdolini
geboren te Jesi
in 1984

Promotiecommisie

Promotor:	Prof. dr. A. G. G. M. Tielens
Overige leden:	Prof. dr. H. J. A. Röttgering
	Prof. dr. S. F. Portegies Zwart
	Dr. J. Brinchmann
	Dr. B. Groves — Max Planck Institute for Astronomy

a Giulia, Pia e Silvano

Il futuro di un fiume è alla sorgente.
Erri De Luca

Table of Contents

I

Introduction

High mass stars dominate the mechanical energy injection into the interstellar medium (ISM), through stellar winds and supernova explosions, and thus the turbulent pressure which helps support clouds against galactic- and self-gravity. Stars with masses larger than 10 $M_\odot$ end their lives in powerful supernova explosions, which release large amounts of energy and momentum and inject most of the metals (elements heavier than hydrogen and helium) contained in a galaxy back into the ISM. Thus, massive stars are responsible of the chemical enrichment of galaxies. They are also the source of intermediate mass elements which play an important role in interstellar dust. Massive stars control the ultraviolet (UV) photon energy budget and the cosmic ray flux, which are important heating, ionization, and dissociation sources of the interstellar gas. Clearly, there is a complex feedback between stars and the ISM that determines the structure, composition, chemical evolution, and observational characteristics of the ISM in galaxies.

Despite their importance, little is known about the origin and early evolution of massive stars. One observable stage of massive star formation is when the forming star is luminous enough to emit a considerable fraction of high energy photons, and starts to ionize the gas in its neighborhood. This is what astronomers call H ɪɪ region. It consists primarily of hydrogen, hence the name – the term H ɪɪ refers to ionized hydrogen – and it has temperatures of around 10,000 K. Because massive stars evolve very rapidly and they do not move far from their birth site, they are good signposts of recent star formation. Hence, emission from H ɪɪ regions provides a direct handle on the environment in which massive stars are formed.

Figure 1.1 – The Orion Nebula as observed by the *Hubble Space Telescope*. An example of Compact H II region. The gas is ionized by few hot, massive stars – known as the Trapezium – located at the center of the region. Credit: NASA/ESA.

One of the key questions in astronomy is what is the cosmic history of star formation, or in other words, how the early universe evolved into the beautiful collection of galaxies and stars that we can see in the sky today. It is still not clear what are the conditions for star formation and how it evolved during the lifetime of the universe. Moreover, it is under discussion how important is mechanical and radiative feedback by massive stars for the evolution of the ISM of galaxies.

1.1 High mass stars and the interstellar medium of galaxies

1.1.1 High mass star formation

Despite their very crucial role, the formation of massive stars remains poorly understood and still under debate. High-mass star formation is generally taken to be a scaled up version of the low-mass star case. However, more complex physical processes take place and complicate its formation scenario. Starting from a giant molecular cloud, a likely sequence of events that leads to the formation of massive stars is as follows (Zinnecker & Yorke 2007):

compression - a cold dense molecular core or filament forms by gravo-turbulent cloud fragmentation in a giant molecular cloud.

collapse - a protostellar embryo forms by gravitational collapse of portions of the core. For a star to form, the force of gravity must overcome the pressure, magnetic forces, internal turbulence and rotation.

Table 1.1 – Typical properties of classes of H II regions.

Type of region	Size (pc)	Density (cm^{-3})	Ionized Mass ($M_\odot$)	Number of ionizing stars[a]
HyperCompact	~ 0.003	$\gtrsim 10^6$	$\sim 10^{-3}$	~ 1
UltraCompact	$\lesssim 0.05$	$\gtrsim 10^4$	$\sim 10^{-2}$	~ 1
Compact	$\lesssim 0.5$	$\gtrsim 5 \times 10^3$	~ 1	~ 1
Classical	~ 10	$\sim 10^2$	$\sim 10^5$	few
Giant	$\sim 10^2$	~ 30	10^3-10^6	$\sim 10^2$
Starburst nuclei	$> 10^2$	~ 10	10^6-10^8	$\sim 10^3$

(a) Calculated assuming 10^{48} photons s^{-1} per star.

accretion - material accretes onto the protostellar object as it evolves towards the main sequence. For low mass objects accretion happens through a disk. Only when all the material has been accreted the star starts nuclear burning in its core. Instead, high-mass objects accretion continues as they evolve towards the main sequence, meaning that the radiation pressure of the photons coming from the star acts against the force of gravity.
disruption - as the first high-mass star forms in a complex, it influences its environment with stellar winds, outflows, UV radiation, and eventually a supernovae explosion. Such feedback eventually disrupts the birth cloud, leaving as a result a OB association or OB star cluster.

1.1.2 H II regions

From the moment that a newly formed massive star begins to ionize its surroundings by emitting a copious amount of UV radiation, an H II region is formed. Since the star is deeply embedded into its natal molecular cloud, the H II region stage is one of the first observable stages of the birth of a massive star. When an H II region forms around a protostar, there is a competition between the expansion of the ionized material and the accretion of gas onto the protostar that is still ongoing. As accretion stops and the expansion takes over, the H II region expands progressively into the surroundings.

Observationally, H II regions are visible at multiple wavelengths due to the variety of physical mechanisms involved in their formation. The gas that is ionized by the central star is observable at radio wavelengths due to the thermal Bremsstrahlung (free-free) emission (scattering of free electrons off ions). In the infrared (IR), the *Galactic Legacy IR Mid-Plane Survey Extraordinaire* (GLIMPSE) showed over 5,000 H II regions detected from dust emission. The dust present in the ISM absorbs the UV light from the star and re-emits it at IR wavelength. Such observations show the beautiful morphologies of different layers of the photo-dissociation region. The optical spectra is dominated by hydrogen and helium recombination lines, and collisionally excited optical forbidden line emission from trace ions such as [O II], [O III], [S II] and [N II] showing different layers of the H II region ionized gas. X-rays can emerge from such a cloud showing both the ionizing star and the characteristics of the hot plasma around it.

Figure 1.2 – Segment of an IR portrait of dust and stars radiating in the inner Milky Way. Blue is IRAC 3.6 μm, green is IRAC 8 μm, and red is MIPSGAL 24 μm. Credit: NASA/JPL-Caltech/Univ. of Wisconsin.

Wood & Churchwell (1989) divided H II regions into morphological classifications based on their Radio emission. The classification is summarized in Table 1.1. The smallest and densest regions observed are called HyperCompact H II region, and are bright at millimeter wavelengths. UltraCompact H II regions have sizes of < 0.1 pc, high electron densities and high emission measures. The Compact H II regions are still buried in their parent molecular clouds, with radii of 0.1 to few pc. The more extended H II regions reach tens of pc (Classical) up to hundreds of pc (Giant) in radius. Figure 1.1 shows the Orion Nebula, an example of a Compact H II region: powered by few massive stars, it has a radius of $\sim$ 1.7 pc.

It seems natural to assume that the classification represents an evolutionary sequence of the expanding H II region: when the massive star forms, a HyperCompact H II region develops, which then expands to become an UltraCompact H II region. However, age is not the only parameter that determines the large range of H II regions. The combined effect of age, number of massive stars powering the region and environment density is at the base of the H II region classification.

1.1.3 Interstellar bubbles

Besides ionizing hydrogen (and other elements) in their surroundings, massive stars – with their UV radiation – excite polycyclic aromatic hydrocarbons (PAHs) in the swept up shell, lighting them up at IR wavelengths, and heat dust to moderate temperatures that radiates at mid-IR wavelengths. Large-scale surveys have been designed to identify such structures: the *Spitzer Space Telescope* with GLIMPSE at 3.6/4.5/5.8/8.0 μm (Benjamin et al. 2003) and MIPSGAL at 24/70 μm (Carey et al. 2009). Thanks to the Milky Way Project (Simpson et al. 2012), a citizen science initiative, the number of known IR bubbles in the inner Galactic plane is about 5100, an order of magnitude more than previous studies. Churchwell et al. (2006, 2007) catalogued about 600 bubbles and found a good correlation of IR bubbles with known H II regions and relatively low contamination from supernova remnants, asymptotic giant branch star bubbles and planetary nebulae reported in the literature. This demonstrate that bubbles are tracers of star formation activity (Deharveng et al. 2010).
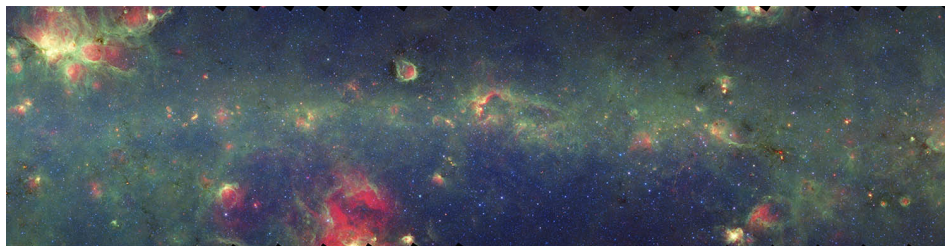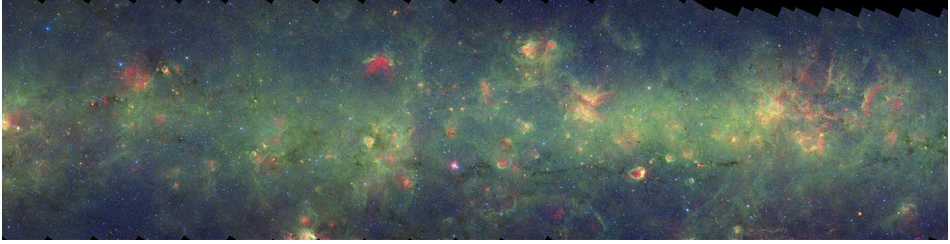
Figure 1.3 – Segment of an IR portrait of dust and stars radiating in the inner Milky Way. Blue is IRAC 3.6 μm, green is IRAC 8 μm, and red is MIPSGAL 24 μm. Credit: NASA/JPL-Caltech/Univ. of Wisconsin.

Figure 1.2 and 1.3 show two sections of the galactic plane as seen by GLIMPSE and MIPSGAL survey. The striking feature is the complexity and variety of bubbles. Some regions are spatially extended and with a intricate morphology, other are smaller and more regular circular regions. Such large number of objects allow statistical studies important to solve longstanding questions, such as triggered star formation. Kendrew et al. (2012) found a strong positional correlation of massive young stellar objects and H II regions with interstellar bubbles.

1.1.4 H II regions: dynamics

When a high mass star ionizes the gas around it, there are important dynamical effects on its surroundings. In a uniform medium, the ionization front expands rapidly into the surrounding medium till the Strömgren radius, where the total recombination rate integrated over the nebula equates the total number of ionizing photons. Such expansion is so fast that the gas does not have time to react dynamically. The photon flux at the ionization front drops, and the expansion changes nature. The overpressure caused by the ionization and heating of the H II region drives the expansion in the neutral medium (Spitzer 1978). A sketch of the structure of such H II region is shown in Figure 1.4 (A). Other physical mechanisms can alter the expansion of an H II region, such as the radiation pressure on the gas (Krumholz & Matzner 2009), that would create the same morphological structure as the overpressure case, but with the additional force pushing the swept-up shell due to radiation. Another mechanism proposed is the presence of stellar winds (Castor et al. 1975), that generates and onion-like structure (Figure 1.4 (B)). In the inside the free-flowing stellar wind is divided by the shocked stellar wind by the reverse shock; and the swept-up shell expands outward into the ISM.

In the case of non uniform medium, the H II region breaks open and gas inside the bubble flows outwards, giving it the name of champagne flow models (Figure 1.4 (C)). Expansion of an H II region in a non uniform medium in the presence of stellar winds has also been studied. The overall shape would be a similar cometary-like region, but the inside of the bubble would contain the same reverse shock between free-flowing stellar wind and the shocked gas. When a star moves through the medium, a similar cometary
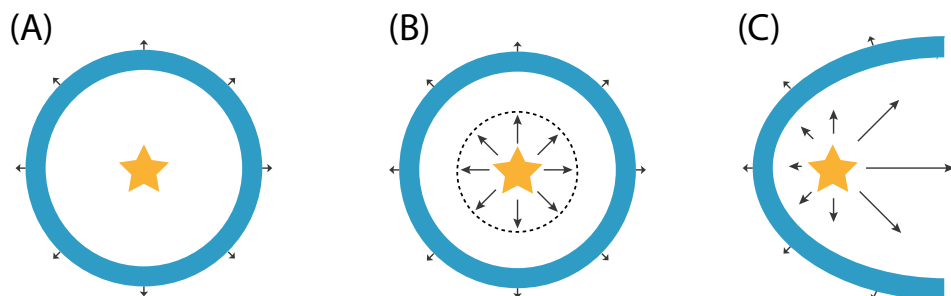
Figure 1.4 – Sketches of H II regions (A) driven by overpressure of the ionized gas (Spitzer 1978); (B) driven by stellar winds (Castor et al. 1975); and (C) in presence of a density gradient in the medium (champagne flow model, van Buren et al. 1990). Credit: Bram Ochsendorf.

shape is achieved.

Many factors contribute to the formation and evolution of H II regions. Looking at the most famous example of an H II region, the Orion Nebula (Figure 1.1), it is easy to realize that the physics involved in such source is more complicated than the simplified description given above. Indeed, non-uniformity of the medium determines deviations from sphericity; stellar winds, and supernovae explosions might trigger second generations of star formation; dynamical movement of stars also changes the morphology.

1.2 Star-forming galaxies

Astronomers have put huge effort in investigating the formation and evolution of galaxies. Wide-field surveys of the local Universe have provided a detailed and statistically robust description of the galaxy population today. Such results mark the endpoint of the description of the formation and evolution of galaxies. Understanding the properties of high redshift galaxies and their similarities and differences with the local galaxy population is crucial to explain the evolution of galaxies.

Galaxies are characterized according to the main source of ionization/excitation of elements. One main division of galaxies is between star-forming and active galactic nuclei (AGN) dominated galaxies. In this work, we only focus on star-forming galaxies since the light coming from these galaxies originates mainly from stars and their associated H II regions. The collective effect of H II regions affects the characteristics of the galaxy, and their emission provides a way to characterize the environment in which massive star form. Therefore, connecting detailed studies of H II regions to galaxies' studies is important to understand their properties and possibly to disentangle differences between the local and high redshift universe.
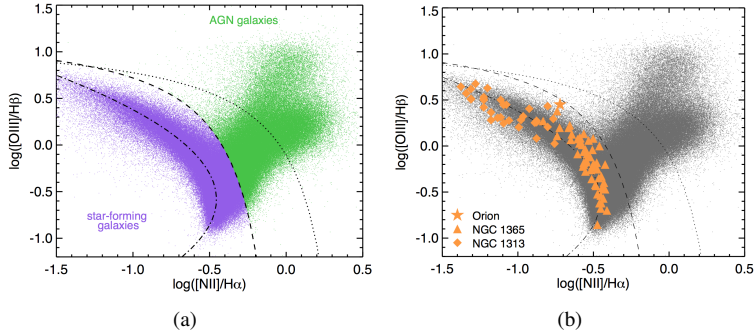
Figure 1.5 – BPT diagram for (a) galaxies from the SDSS catalog (Brinchmann et al. 2004) divided into star-forming and AGN dominated galaxies; (b) H II regions in galaxies at z = 0 with blue symbols (Roy & Walsh 1997, Walsh & Roy 1997, Sánchez et al. 2007), and galaxies from the SDSS catalog with gray dots. The dashed line is the (Kauffmann et al. 2003) line, an empirical separation of star-forming galaxies and AGNs based on the SDSS galaxies. The dotted line is the (Kewley et al. 2001) theoretical limit for star-forming galaxies. The dot-dashed line is a fit to the star-forming galaxies from the SDSS galaxies (Brinchmann et al. 2008).

1.2.1 Line diagnostic diagrams

Optical and IR emission lines from H II regions are an important diagnostic used to study galaxies. Line ratio of emission lines are often used as diagnostics of physical properties such as metallicity, electron density, electron temperature, and hardness of the ionizing radiation.

The Baldwin et al. (1981) diagram (hereafter the BPT diagram) is a commonly used tool to study extragalactic H II regions and their host galaxies. The most used combination is [O III] $\lambda5007$/Hβ versus [N II] $\lambda6584$/Hα. In the galactic context, such plot is also used to classify galaxies since it allows a clear distinction between star-forming and AGN dominated galaxies (Figure 1.5(a)). Star-forming galaxies lie along a narrow sequence, while AGN are found offset due to their much harder ionizing spectrum.

The horizontal axis, [N II]/Hα, strongly depends on the metallicity within the star-forming region that increases with increasing [N II]/Hα. Changes in metallicity correspond to changes in the abundance of an emitting species relative to hydrogen. The results is a weaker emission in lines such as nitrogen and oxygen relative to hydrogen recombination lines such as Hα and Hβ. Instead, the vertical axis of [O III]/Hβ is associated with the average ionization state and temperature of the photoionized gas in the galaxy. Instead, for AGN and shocks the ionization/excitation always leads to a high value of line emission.

In the same plot, single H II regions cover a sequence that overlaps with the star-forming sequence of the SDSS galaxies (Brinchmann et al. 2004). The location on this sequence is controlled by physical properties of the H II region, such as metallicity, density of the ISM, ionization parameter, and age. Understanding how the star-forming sequence

7

is connected to single H II regions on the BPT diagram can be helpful to assess physical properties of unresolved H II regions in galaxies.

The interpretation of emission lines requires significant modeling of both the internal structure and dynamical evolution of the emitting regions. Models of the BPT diagram, or in general any line emission, are produced using photoionization model codes such as Cloudy (Ferland et al. 2013) or MAPPINGS (Sutherland & Dopita 1993, Dopita et al. 2000). It is possible to create a set of predicted H II regions' line emission that can be compared to the observed BPT diagram for a set luminosity of the central star or star cluster, density of the ambient medium, and age. Such modeling is important in understanding H II regions' structures and in constraining their physical properties. By matching observations and a grid of models on the BPT diagram, it is possible to derive an approximate cluster age and ionization state of the region, even if the region is unresolved.

1.3   Thesis outlook

Key questions in star formation theory are the formation of massive stars and their feedback in their environment over cosmic time. This thesis tackles some aspects of this cosmic history of star formation and the way massive stars drive the evolution of galaxies. Specifically, we addressed the analysis of optical observations of star forming galaxies deriving the gas physical conditions of the H II regions associated with its massive star. We also numerically simulated the dynamical expansion of H II region driven by stellar winds and driven by the overpressure of the ionized gas. We carried out comparison of theories and numerical prediction with observations of both the H II region and the interstellar bubbles.

In Chapter 2 we address all aspects of UltraCompact H II regions. Focusing on a prototypical region, G29.96-0.02, we investigate the missing X-ray emission from stellar wind bubbles in H II regions. We conduct a broad study, combining X-ray observations of the hot gas with spectroscopic study of the properties of the ionizing star, and a hydrodynamical study of the dynamical evolution of these regions. We construct three-dimensional hydrodynamical model of the UltraCompact H II region including photoionization and wind effects, radiative processes, mass loading, and bow shock from stellar motion through the cloud. We find that champagne flow models are best at explaining the morphology and the gas dynamics, and that mass loading is necessary to cool the shocked stellar wind gas as the X-ray observations show.

In Chapter 3 we present a class of H II regions formed by champagne flow mechanisms to explain the cometary shape of the dust emission seen inside H II regions. Ochsendorf et al. 2013 (submitted) suggested that the arc-like structure seen at 24 μm is the result of the interaction between radiation pressure from the star with the dust contained in the flow of ionized gas photo evaporated from the birth molecular cloud. We show that in the presence of a champagne flow, the ionized gas inside the H II region reaches velocities at the star location high enough to set up the conditions for a dust wave. Such modeling can also reproduce the observed variety of morphologies of H II regions and their emission characteristics.

In **Chapter 4** we step out, and look at the effects of H II regions on larger scales. Physical parameters of H II regions, such as age, radius and density of the ambient medium, are important in understanding the interaction of massive stars with their surroundings, the mechanisms driving the expansion of the ionized gas, and the link between star-forming galaxies and single H II regions. We select two well-studied H II regions in the nearby galaxy NGC 6822: Hubble V and Hubble X. We obtain well constrained physical parameters of two star-forming regions in the nearby universe and use such information to understand the star-forming sequence of SDSS galaxies in optical line diagnostic diagrams and their relation with single H II regions. We find that the emission characteristics of the star-forming galaxies are consistent with most of their light coming from the few brightest H II regions rather than the most dim ones.

Finally, in **Chapter 5** and **6** we revisit the question of how H II region line emission depends on the physics of winds and radiation pressure. The emission line ratios [O III]/Hβ and [N II]/Hα have been adopted as an empirical way to distinguish between the fundamentally different mechanisms of ionization in emission-line galaxies. However, detailed interpretation of these diagnostics requires calculations of the internal structure of the emitting H II regions, and these calculations depend on the assumptions one makes about the relative importance of radiation pressure and stellar winds. We construct models of single H II regions including and excluding radiation pressure and winds in Chapter 5, and in Chapter 6 we describe a population synthesis code that uses these models to simulate galactic collections of H II regions with varying physical parameters. We show that the choice of physical parameters has significant effects on galactic emission line ratios, and that in some cases the line ratios can exceed previously claimed theoretical limits.

II

X-ray emission from stellar wind driven bubbles: the prototypical UltraCompact H II region, G29.96-0.02

We investigate the missing X-ray emission from stellar wind bubbles in H II regions. Ultra Compact H II regions are unique laboratories to study the interaction of stellar winds with its surroundings; in particular we focus our study on G29.96-0.02 because it is so well-studied at all wavelengths. We address all aspects of UC H II regions: the characteristics of the ionizing star and the energetics involved in the stellar winds, the dynamics of the region and its evolution and expansion. We conduct a broad study, combining X-ray observations of the hot gas with a spectroscopic study of the properties of the ionizing star, and a hydrodynamical study of the dynamical evolution of these regions. We obtained *H*- and *L*-band spectra of the central star of G29.96-0.02 using the ISAAC instrument. Combined with the *K*-band spectrum from Martín-Hernández et al. (2003), we have selected five stellar emission and absorption lines to constrain the stellar parameters. We use a genetic algorithm on the lines to constrain the mass-loss properties of G29.96-0.02. We observed G29.96-0.02 with Chandra X-ray Observatory and found that the hard X-ray emission comes primarily from the star and that it is atypical for single O stars. Furthermore, we found some evidence for a diffuse X-ray component in the soft X-ray band, but no detection for a diffuse hard component. We carried out three-dimensional hydrodynamic numerical simulations using FLASH HC code to understand the dynamics of the region: bow shock, modified champagne flow and modified champagne flow with mass loading. We compare these dynamical studies with observations: we use the radio emission to compare the overall morphology, [Ne II] 12.8 μm line emission to understand the dynamics of the gas and X-rays to unravel the hot gas temperature. We find that champagne flow models are best at explaining the morphology and the gas dynamics, and that mass loading is necessary to cool the shocked stellar wind gas by one order of magnitude to match the X-ray observations.

Silvia Verdolini, Milan Raicevic, Frank Tramper, Arjan Bik, Alex de Koter, Leisa K. Townsley, Patrick S. Broos, Eric D. Feigelson, Alexander G. G. M. Tielens

to be submitted

2.1   Introduction

Recent observations of X-ray emission from H II regions have shed new light on the driving mechanism of H II region evolution. On one hand, compact H II regions like the Orion Nebula and M 17 are associated with diffuse soft X-ray emission at 10^7 K plasma temperatures on parsec scales (Townsley et al. 2003, Güdel et al. 2008, Townsley et al. 2011). This emission is attributed to shocked OB winds which fill bubbles in the molecular cloud. The classical 'Strömgren sphere' of 10,000 K gas is a 'Strömgren shell' on the periphery of these bubbles. On the other hand, the earlier stages of UltraCompact (UC) H II region evolution, with one possible exception (Tsujimoto et al. 2006), show no indication of hot diffuse plasma (e.g., Broos et al. 2007, Oskinova et al. 2010).

The failure to detect hard X-rays from UC H II regions is puzzling. Standard theory of OB stars requires the acceleration of strong winds by resonant coupling of photospheric ultraviolet radiation to an extended atmosphere driving mass loss rates of 10^{-4}-10^{-6} M$_\odot$ yr^{-1} with terminal wind velocities of 1000-2000 km s^{-1} (Castor et al. 1975). These winds sweep up surrounding molecular cloud material. This causes a reverse shock propagating into the wind, resulting in plasmas with temperatures of 10^7-10^8 K and X-ray luminosities of $\geq 10^{34}$ erg s^{-1} (Weaver et al. 1977, van Buren et al. 1990, Harper-Clark & Murray 2009, Arthur 2012). This hard X-ray emission is not observed even at much lower luminosity levels. The absence of hard X-rays might be due to blowout into the turbulent cloud (Mac Low et al. 2007), or shocks weakened by conduction (Weaver et al. 1977, Cowie & McKee 1977, Arthur 2012), mass loading (Hartquist et al. 1986, Pittard et al. 2001b,a), turbulent layers with strong magnetic fields (Kahn & Breitschwerdt 1990), or efficient grain cooling (van Buren et al. 1990). Existing hydrodynamical models of UC H II regions generally treat low energy radiation to model champagne flows or radio morphologies, but do not model in detail the high energy X-rays expected from shocked stellar winds with these effects.

The present paper examines the prototypical and well-studied UC H II region G29.96-0.02 (hereafter G29.96) based on two new observational constraints. First we measure the stellar photosphere and wind properties from near-infrared spectroscopy, finding a spectral type of O5-O6 with $\dot{M} \sim 7 \times 10^{-6}$ M$_\odot$ yr^{-1}. Second we detect a small number of soft X-ray photons within the UC H II region that can be attributed to a plasma with temperature ~0.3 keV and X-ray luminosity $\sim 6 \times 10^{32}$ erg s^{-1}. No hard X-rays are seen. We then construct three-dimensional hydrodynamical model of the UC H II region including photoionization and wind effects, radiative processes, mass loading, and bow shock from stellar motion through the cloud. Viable mass loaded models with realistic radio morphology and [Ne II] 12.8 μm emission line champagne outflow, and with sufficiently weak hard X-ray emission are obtained. The model predictions could be confirmed with deeper X-ray observations.

The rest of this paper is organized as follows. We describe the source G29.96 in Section 2.2. In Section 2.3, we present our new high resolution infrared spectroscopy of the star to determine the mass loss rate and characteristic of the stellar wind and X-ray observations showing a soft diffuse emission indicating a temperature of the gas inside the H II region of about few 10^6 K. In Section 2.4, we describe the numerical method

used in our hydrodynamical calculations that we apply in Section 2.5 and compare to observations in Section 2.6. We conclude in Section 2.7.

2.2   The prototypical UltraCompact H II region: G29.96-0.02

G29.96 is a typical cometary UC H II region, one of the brightest sources at 2 cm wavelength. The cometary shape was first observed by Wood & Churchwell (1989) at radio wavelengths; it is characterized by a bright arc of emission at the head trailing off into a low-surface brightness tail (see Figure 2.1). It is at a distance of 6.2 kpc (Russeil et al. 2011) with a size of ∼ 0.15 pc.
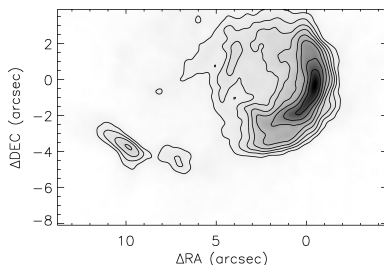
Figure 2.1 – 2 cm continuum map Fey et al. (1995) as readapted by Zhu et al. (2008). The (0,0) position correspond to the peak emission of the [Ne II] line. Contours represent 70%, 50%, 35%, 25%, 17.5%, 12.5%, 9% and 6% of the maximum value in the map.

Zhu et al. (2005) and Zhu et al. (2008) used [Ne II] 12.8 μm fine-structure line mapping as a tool to examine a large sample of compact and UC H II regions with a range of shape and sizes, including G29.96 (see Figure 2.2). The small thermal width of the neon line and the high dynamic range of the maps provide a unique view of the kinematics of UC H II regions. The channel maps show a morphology change from a thin arc-like structure in the blueshifted channels to a cometary shape (as seen in radio) at the molecular cloud velocity to a thicker arc-like structure in redshifted channels.

G29.96 is embedded in a molecular cloud that produces ∼ 15 magnitudes of visual extinction (Martín-Hernández et al. 2002). Just in front of the edge of the H II region at about two arcsec east there is a well studied hot molecular core that is probably not heated by the ionizing star of G29.96, but by a young, deeply embedded massive star currently forming in it. Molecular transitions of NH_3 (Cesaroni et al. 1994) and mid-infrared high angular resolution images (De Buizer et al. 2002) showed that the hot core is characterized by small structures (∼ 0.1 pc), with kinetic temperatures greater than 50 K and up to 200 K, densities approximating 10^7 cm^{-3}, and masses of a couple hundred solar masses. The region around G29.96 is a star forming complex that contains a filament seen in absorption with *Spitzer* with multiple massive cores (Pillai et al. 2011, Beltran et al. 2013). Using a detailed photoionization model of G29.96 Morisset et al. (2002) found
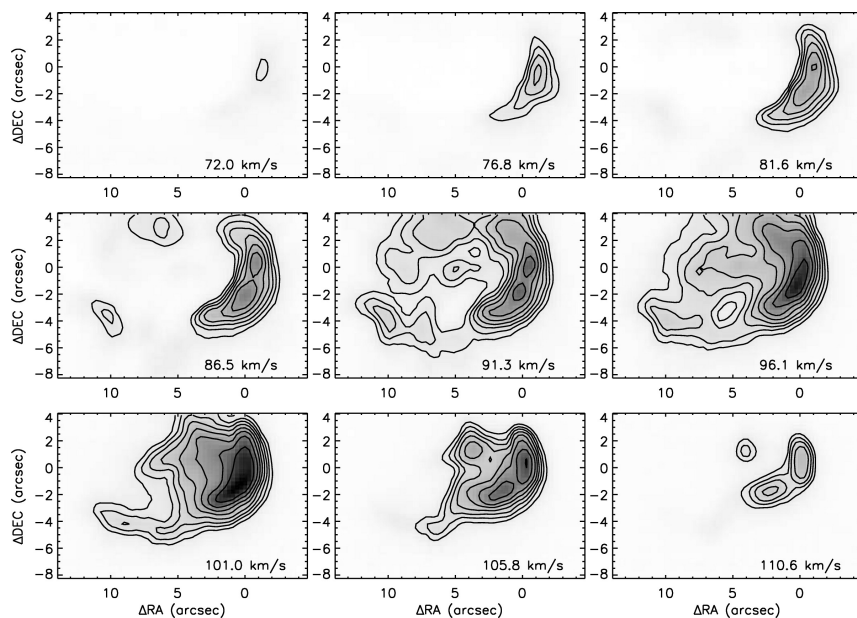
Figure 2.2 – Channel maps of [Ne II] line observations (Zhu et al. 2008). The individual maps sample a single velocity slice in the data cube, representing a width equal to about 4 kms^{-1}. Contours are drawn at 70%, 50%, 35%, 25%, 17.5%, 12.5%, 9%, and 6% of the maximum value of all channels. The molecular cloud velocity is V_{LSR} =98 kms^{-1}.

that the radio and infrared data on G29.96 are best reproduced using a nebular model with two density components: a diffuse ($n_e \sim 680$ cm^{-3}) extended (~1 pc) component surrounding a compact (~ 0.1 pc) dense ($n_e \sim 57\,000$ cm^{-3}) core. G29.96 seems to be associated with a small cluster of stars (Fey et al. 1995, Watson et al. 1997, Pratap et al. 1999). The main ionizing star is located in the focus of the bright arc. The first spectroscopic observations by Watson & Hanson (1997) constrained its spectral type to O5V-O8V. Better spectroscopic observations provided a refinement of the spectral type of O5V-O6V (Martín-Hernández et al. 2003), consistent with other observational constraints on the effective temperature of the central star.

Including the new observations presented in this paper, all the important parameters of the source G29.96 are well constrained. The radio image illustrates the morphology of the ionized gas (Figure 2.1). The presence of a hot core in front of the radio arc-structure indicates that the H II region is expanding in a high density medium, with a density distribution typical of a molecular cloud on scales of ~ 0.1 pc. The near-infrared observations of the effective temperature, the surface gravity and the characteristics of the stellar wind. The [Ne II] line emission reveals the dynamics of the ionized gas, that can be compared with the gas hydrodynamics of the simulations. Finally X-ray observations measure the presence and characteristics of hot gas inside the H II region, directly probing the interaction of the ionizing star and its wind with its surroundings.

Since first discovered, a number of models have been suggested in the literature to explain UC H II region: bow shock (Tenorio-Tagle 1979), champagne flow (Mac Low et al. 1991), turbulence (Peters et al. 2010), and mass loading (Dyson et al. 1995). In view of more recent observations of the source G29.96, the first two models seems preferred for this source. Indeed, Arthur & Hoare (2006) conducted a numerical study testing the bow shock and champagne flow models and combinations of the two models. They suggested that the best fit is reproduced by a combination of the two classical models: a star with a stellar wind moving though a medium (bow shock) with a density gradient (champagne flow).

We present in this work tailored three-dimensional simulations aimed at disentangling the interaction mechanisms between stellar wind and surrounding medium in the specific case of G29.96. We show that both bow shock and champagne flow models predict the presence of hot gas inside the H II region, that is not observed. To solve this problem, we introduce mass loading from photo evaporation or ablation in the hot gas. In a series of papers Dyson et al. (1995), Redman et al. (1996), Williams et al. (1996) proposed mass loading in order to explain the lifetime problem and the shape at radio wavelength of UC H II regions. They use the spatial distribution of the proplyd around the star to (artificially) create the morphology of the region. Instead we assume radial symmetry of the proplyds and explore whether mass loading can reproduce the temperature of the hot gas, as observed in X-ray.

2.3 Observations

2.3.1 IR observation of the star and its wind

2.3.1.1 H- and L-band spectra

We obtained H- and L-band spectra of the central star of G29 using the ISAAC instrument (Moorwood et al. 1998), mounted at UT1 of ESO's *Very Large Telescope* (VLT) on Paranal, Chile. The observations where performed in service mode with the H-band observations executed on April 14, 2009. The L-band data are split in 4 observations and were obtained on August 27, September 23 and October 1st 2009.

The medium resolution setting in combination with a narrow slit (0.3″) was used to obtain a resolution of R=10,000 for the H-band spectrum and R=6,700 in the case of the L-band spectrum. The spectral setting for the H-band observations covers the wavelength range 1.669 μm to 1.748 μm, while the L-band spectra cover the wavelength range from 3.858 - 4.124 μm. After each science observations a standard star (HD 181939) of spectral type A0V, using the same instrument settings, was executed. For both datasets, a nodding offset of 25″ was applied as well as a small random jitter of 3″ to allow a sky subtraction without contamination of the surrounding nebular emission of the UC H II region. For the H-band a Detector Integration Time (DIT) of 300 seconds per frame was chosen. Four nod cycles (8 frames) were used to take the final spectrum resulting in a total integration time of 40 minutes. In the L-band, the sky background is much brighter, therefore a short DIT is required in order not to saturate the sky background. For the L-band observations
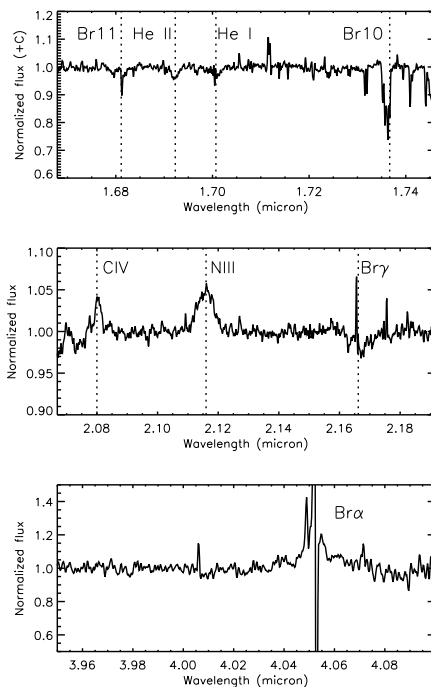
Figure 2.3 – *H-* , *K-* and *L*-band spectra of the central star of G29.96.

we chose a DIT of 5 sec with NDIT = 31, such that each frame is saved after averaging 31 observations of 5 sec. In total we applied 32 nodding cycles split over 4 observing blocks to acquire the final spectrum. The total integration time for the *L*-band spectrum is 3 hours and 26 min.

2.3.1.2   Data reduction

The spectroscopic data are reduced using the ESO pipeline for ISAAC version 6.1.2 in combination with Gasgano. The *H*-band data are corrected using dark and flat field frames taken the morning after the respective observations. The wavelength calibration of the *H*-band data is performed using Ar and Xe arc spectra. After that the final 2-dimensional spectrum was constructed by applying all the calibration files and subtracting the offset positions for the sky subtraction.

For the *L*-band spectra, the wavelength calibration frames were providing a different wavelength solution for each observation, even though the observations were all taken with the same central wavelength. In order to improve the wavelength calibration, we constructed the final two-dimensional spectrum by applying the dark, flat and subtraction of the background first. After that the spectrum was extracted, the 5 emission lines (Hy-

drogen, He I) from the H II region were identified covering the entire observed range of the spectrum. Using their known wavelengths, a 2nd order polynomial fit was performed to derive a wavelength solution for the observed spectra. This results in all the four observations on the same wavelength scale and allows the combination of the entire L-band dataset.

The 1-dimensional spectra are extracted using the iraf task *doslit* and combined to a final spectrum (Figure 2.3). Nebular emission is subtracted using a median average in the cross-dispersion direction. This resulted in reducing the contribution of the H II region to a minimum, but not all the emission could be subtracted due to variations of the nebular emission on the slit. When extracting the H-band spectra, it turned out that half of the frames had a large detector artifact on the position where the spectrum of the central star was placed. This artifact covered one of the lines of interest for this paper (He I, 1.7007 μm). To recover this line we re-reduced the spectra using only half the dataset and extracted the spectra of half of the frames, resulting a spectrum with a usable He I line.

The standard star observations for both the H-band and L-band are reduced identical to the science observations. As the standard star is of spectral type A0V, its H-band spectrum also has hydrogen lines. These lines are removed by fitting them with a gaussian profile, resulting in a atmospheric transmission spectrum at the airmass of the science observations. The telluric lines are finally removed using the iraf task *telluric*. For the L-band observations we decided not to apply the telluric correction as the Br α line is the only line used and is not affected by any telluric absorption.

As additional dataset, we use the K-band spectrum (2.068 - 2.192 μm) from Martín-Hernández et al. (2003). We re-reduced the spectrum using the latest version of the ESO pipeline and corrected for nebular contamination in a identical way as the H-band spectrum. The final reduced spectra are plotted in Figure 2.3.

2.3.1.3   Mass loss rate

We use the genetic algorithm method developed by Mokiem et al. (2005) to constrain the mass-loss properties of G29.96. This method fits synthetic line profiles produced by the non-LTE atmosphere code FASTWIND (Puls et al. 2005) to observed spectral lines. The most important properties that are constrained by the fits are the effective temperature T_{eff}, surface gravity log g and the mass-loss rate $\dot{M}$. Errors on the derived parameters are calculated as described by Tramper et al. (2011).

To constrain the mass-loss properties of G29.96, we use the observed Br 11, He II $\lambda16923$, He I $\lambda17007$, Br γ and Br α lines. The resulting best-fit parameters are $T_{\text{eff}} = 39.8^{+7.6}_{-1.9}$ kK, log $g = 3.66^{+0.28}_{-0.16}$ and log $\dot{M} = -5.15^{+0.1}_{-0.2}$ M$_\odot$ yr^{-1}. Although the mass-loss sensitive lines suffer severely from nebular contamination, the mass-loss rate can, in this particular case of a strong wind, still be constrained by fitting the line wings. Figure 2.4 shows the best-fit Br α line profile, as well as profiles for the 95% probability boundary values.

Given the spectral type O5.5 (Martín-Hernández et al. 2002), we can derived stellar parameters from Martins et al. (2005): effective temperature is 40,000 K, luminosity log($L/$ L$_\odot$) is 5.41, and mass is 34.17 M$_\odot$. The empirical mass-loss rate recipe of Vink
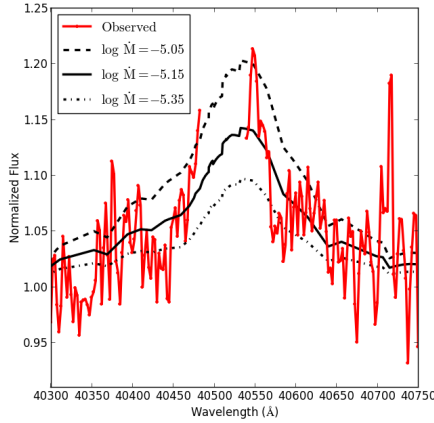
Figure 2.4 – Observed Br α emission with overplotted the best fit model (black solid line) and models for the 95% probability boundary values of $\dot{M}$ (dashed and dashed-dotted lines). Nebular contamination has been clipped from the observed spectrum.
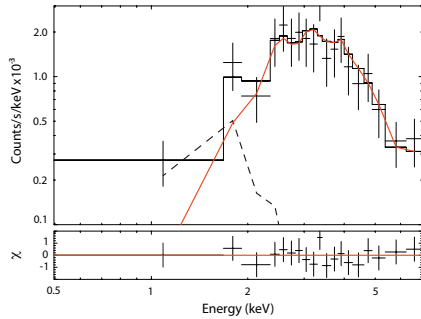
Figure 2.5 – ACIS spectra of G29.96. Stellar component with full line and diffuse component with dashed line.
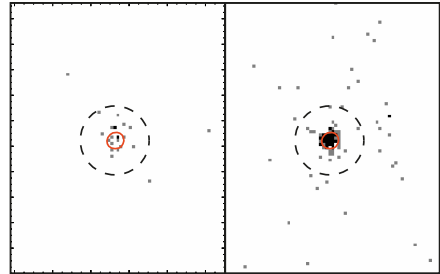
Figure 2.6 – X-ray image of G29.96: 0.5-2 keV events on the left and 2-8 keV on the right. The small aperture has a radius of 2.7 arcsec and contains the diffuse component; the big aperture (dashed line) AE extraction polygon encloses 83% of the O-star PSF.

et al. (2000) would predict a mass-loss rate log $\dot{M} = -6.08^{+0.28}_{-0.03}$ M$_\odot$yr^{-1} depending on the terminal velocity assumed. We adopt values of the terminal wind velocity ranging from 1000 to 3000 km s^{-1}. Such empirical value is about eight times lower than our derived value with Fastwind models. However considering the uncertainties in the derivation of the spectral type and the approximations of the Vink et al. (2000) empirical recipe, we can consider the ionizing star a normal O5.5-O6 star with a typical mass-loss rate. Consistently, we assume that the terminal wind velocity has a typical value of 2000 km s^{-1}.

Table 2.1 – X-ray luminosity and surface brightness. We assume a distance of 6.2 kpc (Russeil et al. 2011).

		Soft (0.5-2 keV)	Hard (2-8 keV)
Observations			
Star (inner 1.31 arcsec^2)	L_X (erg s^{-1})	2.4×10^{33}	1.2×10^{33}
Annular region (diffuse)	L_X (erg s^{-1})	6.7×10^{32}	6.0×10^{31}
	S_b (erg s^{-1} arcsec^{-2})	3.1×10^{31}	2.8×10^{30}
Champagne Flow Simulations			
no mass loading	L_X (erg s^{-1})	5.9×10^{32}	7.8×10^{32}
with mass loading	L_X (erg s^{-1})	2.1×10^{32}	5.7×10^{32}

2.3.2 X-ray observations

G29.96 was observed by the Chandra X-ray Observatory using the ACIS Imaging Array in 2009 February, for 27.5 ks. The aimpoint of the telescope was placed on the UC H ɪɪ region, to achieve the highest spatial resolution and sensitivity possible. A total of 172 X-ray point sources were found across the entire 17′ × 17′ field of view. Details of this observation are given in Townsley et al 2014 (submitted).

The third-brightest source in the field (with 105 net counts) is the O star ionizing the UC H ɪɪ region, with an ACIS source name of 184604.07-023921.5 (which defines the coordinates of the X-ray source). The X-ray spectrum of this source is well-fit in *XSPEC* by a simple absorbed thermal plasma, with the model form *tbabs*apec*, with the plasma abundance frozen to solar values (Figure 2.5). The fit gives an absorbing column of $N_H \sim 12 \times 10^{22}$ cm^{-2} (90% confidence range [8×10^{22}, 1.8×10^{23}]) and a thermal plasma temperature of kT ~ 1.8 keV (90% confidence range [1.2, 3.3] keV). Using a conversion is $N_H \sim 1.6 \times 10^{21} A_V$, our derived N_H amounts to $A_V \sim 75$ mag.

The ionizing star of G29.96 is a hard X-ray source with an X-ray luminosity of 3.5×10^{33} erg s^{-1} (90% confidence range [1.4×10^{33}, 1.3×10^{34}]), see Table 2.1. This hard X-ray emission is atypical for single O stars, and likely indicates that it is a colliding-wind binary and/or has a substantial magnetic field.

The observed stellar X-ray luminosity represents only a small fraction ($\simeq 4 \times 10^{-4}$) of the mechanical luminosity of the star and, hence, whatever process converts wind kinetic energy into X-ray, it is not very efficient. We note that the column density of absorbing gas is much larger than the gas column density associated with the dust absorbing the H ɪɪ region (A_V ~15 mag, Martín-Hernández et al. 2002). Hence, much of the X-ray absorbing column is associated with the stellar wind, reinforcing that only a small portion of the wind had been converted into hot, X-ray emitting gas.

We performed two concentric extractions of the X-ray data, within an *inner* region (dashed line polygon in Figure 2.6) and the *outer* region (full line circle in Figure 2.6). We are interested in the photometry of the annular region between the *outer* and *inner*

region, which we will refer to as the *annular* extraction. The annular extraction has two background components: the wings of the PSF of the star, and the large-scale 'flat' background. The number of counts expected from the wings of the star can be calculated using the fraction of the PSF enclosed by the inner aperture, which is energy dependent. We have direct measurements of this PSF fraction at 1.5 and 4.5 keV. The 1.5 keV value is suitable for the soft band; for the hard band we estimate a PSF fraction at the median energy of the events in that band (3.5 keV) by interpolating between the two measurements. We find that the annular region contains very little wing contamination in the soft band (~1 count), but significant contamination in the hard band (~32 counts). The number of counts expected from the large-scale "flat" background (instrumental and astrophysical) can be estimated using a hand-drawn background region – 382 times larger than the red aperture – that avoids other detected point sources and areas with off-nominal exposure time. In summary, the data indicate an excess of 12.6±3.77 counts in the soft band that could be attributed to diffuse X-ray emission, and 6.13±7.01 counts in the hard band (i.e. consistent with a null detection). As in all massive star-forming regions, there may be a population of unresolved low-mass stars near the O star that would complicate interpretation of the "diffuse" emission.

We use the program PIMMS[1] NASA/GSFC HEASARC (first described in Mukai (1993)) to derive the intrinsic luminosity of the soft components. We use the APEC plasma model with adopted temperature kT=3.4 keV (T = 4×10^7 K, see Section 2.5) and an absorbing gas column corresponding to A_V ~15 mag. We summarize the luminosity found for the diffuse component in Table 2.1. We also calculate the intrinsic surface brightness of the diffuse components by dividing by the area of the annulus (~ 2.6 arcsec^2) to consistently compare with a plasma that uniformly fill the entire radio UC H II region (Figure 2.5).

In conclusion, there is no evidence for an extended hard X-ray component down to a limit of 1.6×10^{31} erg s^{-1} for an adopted plasma temperature of kT=3.4 keV (see above for assumptions). We do find some evidence for a diffuse component of about 12.6 counts in the soft X-ray band indicating a plasma temperature of ~0.3 keV.

2.4   Numerical method

We use the code FLASH HC, a modified version of the FLASH code (Fryxell et al. 2000) extended with a Hybrid Characteristics radiative transfer scheme developed by Rijkhorst et al. (2006). The FLASH code is a block-structured, adaptive mesh refinement (AMR) hydrodynamics code with modular design and scalable to tens of thousands of processors. The Hybrid Characteristics (hereafter HC) is a ray-tracing radiative transfer scheme designed specifically with FLASH block structure in mind. To obtain the intensity at each simulation cell, column densities along rays that connect each cell with a source of radiation are computed. Total column density in one such ray is obtained by adding the contribution of each block intersected by the ray, which is in turn interpolated from ray

---

[1] http://heasarc.gsfc.nasa.gov/Tools/w3pimms.html

segments precomputed on each block. The use of interpolation eliminates the overhead associated with recomputing column densities in neighbouring rays. On the other hand, limiting the interpolation to the coarse, block level minimizes numeric diffusion that can be caused by it. This makes the HC scheme both highly efficient and precise. Furthermore, the algorithm is highly parallel, as most of the work is performed independently on each block as intended by FLASH design. We have made several improvements to the HC scheme since its introduction by Rijkhorst et al. (2006), some of which have already been described in Raicevic (2010) and one will be detailed here[2]. We present tests of the code in Appendix 2.8. The updated version of the scheme was employed in the radiative transfer code comparison project by Iliev et al. (2009).

2.4.1 New approach to find blocks cut by a ray

One of the steps of the hybrid characteristic method is finding all the blocks that are cut by a single ray, which is a non-trivial problem since the blocks are distributed among different processors. Rijkhorst et al. (2006) solved this problem by representing the whole block structure using a uniform grid array stored on each processor, with the resolution corresponding to the highest refinement level of the AMR grid. The list of block cut by each ray is then obtained by tracing the ray over this helper array. Unfortunately, the fact that the helper array is itself not distributed among processors makes it a memory bottleneck, artificially limiting the highest refinement level the AMR structure can reach. One solution for this problem was presented by Peters et al. (2010) who removed the helper array and instead used a custom function that finds the list of cut block by walking the AMR tree structure. We use a very similar approach to theirs, with the difference that the crux of our implementation is a function already present in the FLASH code's particle module which reports the global block number for a point placed anywhere within the simulation volume. Starting at the beginning of each ray, we move a point along it and query the tree structure through the aforementioned function to obtained the list of cut blocks. The point is moved in steps of size of the last block found, in order to avoid unnecessary queries. This new approach finds the same lists of cut blocks as the original one while significantly reducing the memory cost of ray tracing, which is crucial for achieving high enough spatial resolution of the AMR grid needed for physical problems of our interest.

2.4.2 Changes to the chemistry solver

The biggest change to the HC scheme introduced in Raicevic (2010) was the update of the chemistry equation solver, which was redesigned to guarantee photon conservation in respect of both spatial and temporal discretization. As shown in Abel et al. (1999), in order for the photo-ionization rate Γ_{ph} not to depend on the spatial size of the volume elements in a simulation volume, it should be set directly to correspond to the number of photons that is absorbed by the volume element. Assuming a hydrogen-only medium:

---

[2] The code is available upon email request.

$$\Gamma_{\text{ph}} \propto \frac{N_{\gamma,\text{in}}(1 - e^{-\Delta\tau})}{N_{\text{HI}}}, \tag{2.1}$$

where $N_{\gamma,\text{in}}$ is the number of photons entering the volume element, $\Delta\tau$ is its optical depth and N_{HI} is the number of neutral hydrogen atoms found in the element. Both $\Delta\tau$ and N_{HI} are linear functions of the hydrogen neutral fraction of the volume element, x_{HI}. We adopted the version of Eq. 2.1 photoionization rate as formulated in Mellema et al. (2006). Assuming that the time step is short enough that x_{HI} remains constant in all volume elements, this formulation will guarantee the correct number of ionizations in the simulation volume irrespective of the spatial resolution. However, ensuring this criterion usually requires extremely short time steps, which makes the RT component of a simulation by far the most expensive. The need for short time steps can be significantly relaxed if the chemistry solver takes into account the change of x_{HI} during a time step, as shown in Mellema et al. (2006). Due to the change of the neutral fraction in the simulation volume during a longer time step, both $N_{\gamma,\text{in}}$ (which is a description of the total column density between the volume element and the source) and x_{HI} (which describes the column density within the volume element itself) are not constant. In order to take these changes into account, Mellema et al. (2006) used a short characteristics ray tracing scheme to construct rays in an outward manner starting from the source and using the time-averaged optical depths of individual cells. The way that the volume elements are crossed in the scheme allow it to automatically take the change in $N_{\gamma,\text{in}}$ into account, but makes the parallelization of the algorithm difficult.

Due to the highly parallel nature of the HC algorithm, it is impossible to adapt it to the Mellema et al. (2006) prescription which depends on the order of cell crossings. However, we can take into account the changes of the neutral fraction x_{HI} *within the volume element* with little effort. In Raicevic (2010), it was shown that just that is enough to correctly track D-type ionization front using several orders of magnitude longer time steps than before possible. In order to make this possible, we replaced the originally used DORIC solver (Frank & Mellema 1994), which solves the chemistry equations in an efficient manner by iterating on their analytic solutions, by the Livermore Solver for Ordinary Differential Equations (LSODE, Hindmarsh 1980) with which we directly integrate the same equations taking into account the time dependence of x_{HI}. While the new solver is significantly less efficient than the original one, the ability to employ much longer time steps for the whole RT calculation makes the change worthwhile.

2.4.3 Cooling

For the cooling rate, we use a sum of collisional ionization, collisional excitation, recombinations and Bremsstrahlung cooling rates (Theuns et al. 1998). We added Oxygen cooling lines. See Table 2.2.

Table 2.2 – Cooling rates (ergs cm^{-3}s^{-1}) of the elements considered. We adopt the following nomenclature: $T_n \equiv T/(10^n$ K) with T in K; H I $= n_{\text{H I}}/n_{\text{H}}$, where $n_{\text{H I}}$ is the density of neutral hydrogen and n_{H} is the total hydrogen density; H II $= n_{\text{H II}}/n_{\text{H}}$, where $n_{\text{H II}}$ is the density of ionized hydrogen; n_e is the number of free electrons; and g_f is the Gaunt factor.

Cooling	Approx	El.
Collisional ionization	$c_1 = 2.54 \times 10^{-21} T^{1/2} \exp(-157809.1/T)(1 + T_5^{1/2})^{-1} n_e \text{H I}$	H I
Recombination	$c_4 = 8.7 \times 10^{-27} T^{1/2} T_3^{-0.2}(1 + T_6^{0.7})^{-1} n_e \text{H II}$	H II
Collisional excitation	$c_8 = 7.5 \times 10^{-19} \exp(-118348/T)(1 + T_5^{1/2})^{-1} n_e \text{H I}$	H I
Bremsstrahlung	$c_{10} = 1.42 \times 10^{-27} g_f T^{1/2} n_e \text{H II}$ $g_f = 1.1 + 0.34 \exp\{-[(5.5 - \log_{10} T)^2]/3\}$	H II
Line emission	$c_{\text{O III}} = 5 \times 10^{-23} (n_e \text{H II})^2 T_4^{1/2} \exp(-29000/T)$	[O III]
Line emission	$c_{\text{O I}} = 2.5 \times 10^{-29} (n_e/ \text{H II})^2 T^{0.67} \exp(-228/T)$	[O I]

2.4.4 Stellar winds

The stellar wind is implemented in the simulation as a source term centered in a region around the location of the star. At each time step our modified version of `hydro_sweep` function restores the wind conditions in the wind source region. Even though the stellar wind region is part of the computational domain, effectively it behaves as an inflow boundary. We chose the optimal radius of the stellar wind generator, that satisfy both requirement of being small enough that the stellar wind reaches its terminal velocity outside the wind generator region and large enough that the spherical surface can be resolved reasonably well in cartesian coordinates. We always use the highest refinement level around the star source term to make sure it is as spherical as possible at all times.

At each time step, we set the density of the wind ρ_w the temperature of the wind T_w and the radial velocity of the stellar wind v_w in the wind generator region. We assume a stellar wind velocity $v_w = 2000$ km s^{-1}, and we derive density and temperature of the wind from the mass loss rate $\dot{M}$ as follows:

$$\rho_w = \frac{\dot{M}}{4\pi v_w R_\star^2}, \tag{2.2}$$

$$T = \frac{\mu m_{\text{H}} v_w^2}{3k}, \tag{2.3}$$

where $R_\star$ is the radius of the star, that in our simulations corresponds to the radius of the source term, in general some orders of magnitude bigger that the actual star radius; ρ_w and T_w are respectively the density and temperature of the wind, k is the Boltzmann

constant, μ is the mean mass per particle and m_H the mass of a hydrogen atom. We have assumed that the velocity of the wind is close to the expansion velocity of an adiabatic gas into vacuum. From Eq. 2.2 and Eq. 2.3 we can derive the density of the wind, ρ_w, and an approximate value for the temperature of the wind, T_w. We also give the gas in the stellar wind source terms a radial velocity equal to the stellar wind terminal velocity.

2.4.5   Star moving

We simulate the movement of the star as the medium moving in the opposite direction and we keep the star position fixed. In this way we avoid waste of computation time in recalculating the movement of the grid. We give a bulk velocity along the positive x-axis to the ambient material at the initial time step. We set the negative x-boundary as an inflow boundary with material going in at the velocity of the star $v_\star$.

2.4.6   Mass loading

With mass loading we refer to the general idea that the injection of mass in the wind will cool it down, making it invisible in X-rays. Mass loading occurs when gas from embedded clumps is stripped away and injected in the surrounding medium. The mechanism of injection of mass into the medium can be photoionization or hydrodynamic ablation.

The aim of this paper is to understand the effects of mass injection in shaping and determining the energy budget of the UC H II region, therefore we assume that mass loading happens as a localized injection of mass that we artificially include in the simulations. At this point we are not interested in understanding which of the mechanisms is responsible for the mass loading. We implement mass loading as localized sources of mass, such as proplyds in Orion nebulae. Henney & Arthur (1998) model the volume density of proplyd in Orion as

$$\rho_p(D) = \frac{\rho_0}{(1 + D^2/D_0^2)^\alpha}, \tag{2.4}$$

where D is the distance from the source, D_0 the inner radius within which there are no proplyds, ρ_0 is the central stellar density and $\alpha=1.29$ is a parameter derived from observations of Orion. By assuming that the proplyd fraction f_p as a function of the projected radius d depends only on the parameter α and that the proplyd and stellar profiles have the same ρ_0 and D_0, they derive

$$f_p(D) = \frac{\Gamma(\alpha - 1/2)}{\sqrt{\pi}\Gamma(\alpha)} \left[1 + \left(\frac{d}{D_0} \right)^2 \right]^{1-\alpha}, \tag{2.5}$$

where Γ is usual gamma function.

We randomly pick the radial positions of each clump using Eq. 2.5, so that the resulting distribution follows Eq. 2.4. Besides location, every clump is the same: it is characterized by a radius, a mass loss rate and a velocity of the gas injected. Numerically we implemented it in the same way as we did for the stellar wind. Given mass loss rate and velocity of the gas lost we derive density and temperature of the gas injected (similar

Table 2.3 – Fiducial parameters

Star parameters		
Type	O5.5	
$\mathbb{N}_{Lyc}$	8.5×10^{48} s^{-1}	
Stellar wind		
$\dot{M}$	7×10^{-6} M$_\odot$ yr^{-1}	
v_w	2000 km s^{-1}	
$R_\star$	4×10^{16} cm	
Star moving		
$v_\star$	20 km s^{-1}	

Mass Loading distribution of clumps		
number of clumps	50	
D_0	$\sim 6 \times 10^{16}$ cm	
α	1.29	
Mass Loading gas injection		
$\dot{M}_c$	10^{-6} M$_\odot$ yr^{-1}	
R_c	5×10^{15} cm	
v_c	10 km s^{-1}	

to Eq. 2.2 and 2.3). Since proplyds are gravitationally bound we do not change their location during the simulation.

2.5 G29.96: simulations

We carry out three dimensional simulations aimed at explaining the observed morphology and dynamics of G29.96. We follow the Arthur & Hoare (2006) study and carry out three models: bow shock model, modified champagne flow model (ionizing star with stellar wind in a medium with a density gradient), and the addition of mass loading on the modified champagne flow model. We present numerical models of the three theoretical scenarios in three-dimensions with initial parameters suitable for G29.96 as derived from observations.

2.5.1 Bow shock model

The source of ionizing photons is assumed to move in a uniform medium of density 5×10^4 cm^{-3} and velocity 10 km s^{-1}. The box is 1 pc in each direction. The maximum refinement level is 6, with smallest refined element being ~0.01 pc. The source is kept steady in the computational box, and the medium is moving at the velocity of the star. The stellar wind is launched from a spherical region of radius 0.013 pc around the location of the star.

In Figure 2.7 and 2.8 top row, we show the number density, velocity field, temperature and ionization front after 10,000 yr and 20,000 yr from the start of the simulation. At the beginning of the simulation the ionization front expands up to the Strömgren radius, 0.02 pc, on a recombination timescale 1.3 yr. Later, the ionization front is taken over by the stellar wind that shocks the gas heating it up, and sweeps up a dense thin shell of neutral material, in which the ionization front is trapped. As the swept-up shell expands, the stellar wind creates a reverse shock with the shocked gas at a radius of ~0.05 pc. The result is a stratified structure similar to the Castor et al. (1975) solution. Close to the star there is the free-flowing new stellar wind material that has a density of about 10 cm^{-3} and
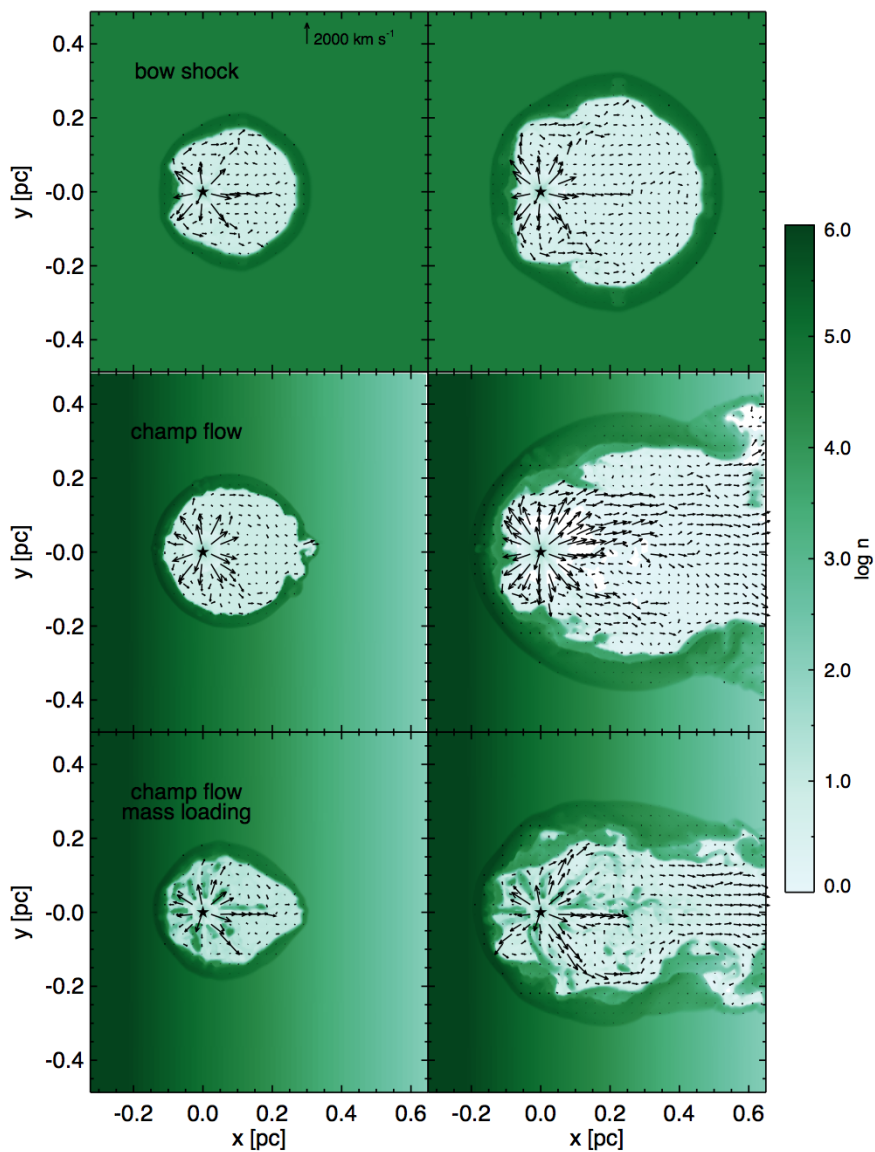
Figure 2.7 – Number density (in cm^{-3}) together with the velocity field (in km s^{-1}) for the bow shock model (top row), the modified champagne flow (middle row), and modified champagne flow model with mass loading (bottom row) at age 10,000 yr (left column), and 20,000 yr (right column) of a slice of 3D simulations through the location of the source. In the bow shock model the medium is uniform and the star moves through it. For the other two models the star is not moving and the density profile has a gradient.
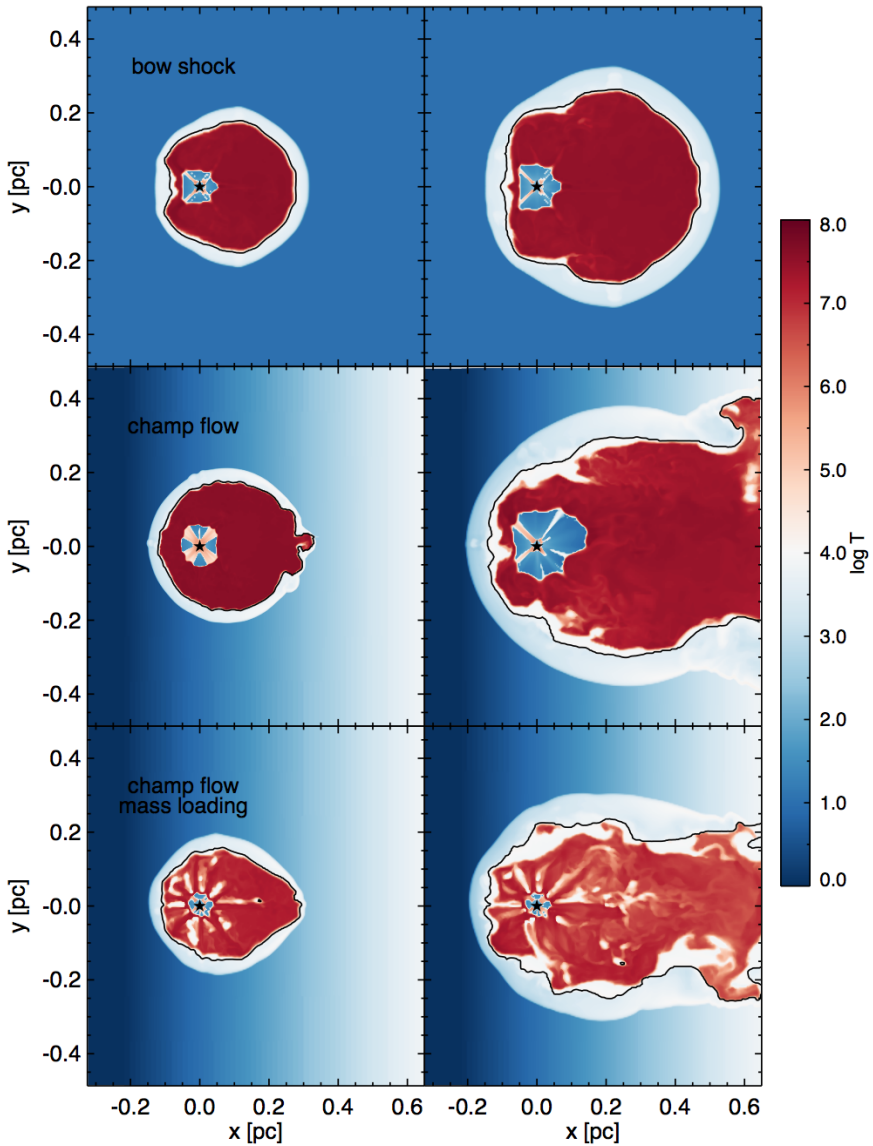
Figure 2.8 – Gas temperature (in K) together with the ionization front (marked in black) for the bow shock model (top row), the modified champagne flow (middle row), and modified champagne flow model with mass loading (bottom row) at age 10,000 yr (left column), and 20,000 yr (right column) of a slice of 3D simulations through the location of the source.

temperature 100 K, the amount of thermal pressure injected by the star is fixed, and as the gas expands radially, the volume occupied increases and density and temperature drop consequently. The free-flowing stellar wind is separated from the shocked stellar wind gas by the reverse shock. The shocked gas has a temperature up to 4×10^7 K and density of 10 cm^{-3}. The contact discontinuity divides the shocked hot gas from the swept-up and photoionized gas that has a density of about 1000 cm^{-3} and temperature 10^4 K. The shell of ionized gas extends up to the ionization front that is trapped inside the swept-up shell of neutral material with density up to 10^6 cm^{-3} and temperatures of few hundred Kelvin.

The movement of the star through the medium creates the bow shock that at an early phase is an elongate sphere with the star located offset from the center. At age 20,000 yr, the star is completely offset in the H II region and gas is flowing from head to tail. The swept-up material is located in a thick dense shell that does not break up before leaving the box. Indeed, the high density of the medium prevents this to happen, and such a high density is needed to keep the size of the region as small as observed (0.2-0.3 pc in radius).

The shocked stellar wind gas is turbulent, primarily due to Rayleigh-Taylor instabilities creating at first the typical mushroom hat shape and then evolve into more chaotic motions along two vortices. It is particularly visible at the head of the region, where gas with high pressure is pushed by the stellar wind into the medium and against the ram pressure due to the movement of the star. The instability sets up at the beginning of the simulation, creating a mushroom-like shape. At a later stage, the instability propagates and becomes Kelvin-Helmholtz unstable as the gas moves along the walls of the H II region.

2.5.2 Modified champagne flow model

We set up an ionizing star at fixed location with a stellar wind in a medium with a density gradient that follows an exponential profile $n = n_0 \exp(x/H)$, where n_0 is the density at the location of the star, equal to 5×10^4 cm^{-3} and H is the scale height set equal to 0.1 pc.

In Figure 2.7 and 2.8 middle row, we show the number density, temperature and ionization fraction after 10,000 yr and 20,000 yr from the start of the simulation. As in the case of the bow shock simulation, the overall structure consists of a free-flowing stellar wind region, hot shocked stellar wind, ionized gas shell and swept-up dense neutral material. Since the medium is not uniform the ionized region is not a sphere, the H II region expands further to the low density side creating an egg-like shape.

After 10,000 yr the H II region breaks open towards the low density side. The ionization front is trapped in the swept-up shell of the stellar wind. At the tail of the region, the swept-up shell is thinner than at the head. With time the swept-up shell becomes progressively thinner till the point where thin shell instabilities start to take place. Those instabilities corrugate the shell and facilitate the shell to break up and photons to escape (see Appendix 2.8 for more details on the thin shell instability). The shocked gas inside the bubble is at about $\sim 4 \times 10^7$ K. At 20,000 yr, the H II region is completely open and the ionized gas accelerates and escapes, and the ionization front penetrates deeper into the swept-up shell. As in the case of the bow shock model, Rayleight-Taylor instabilities dominate inside the hot bubble, making it turbulent.
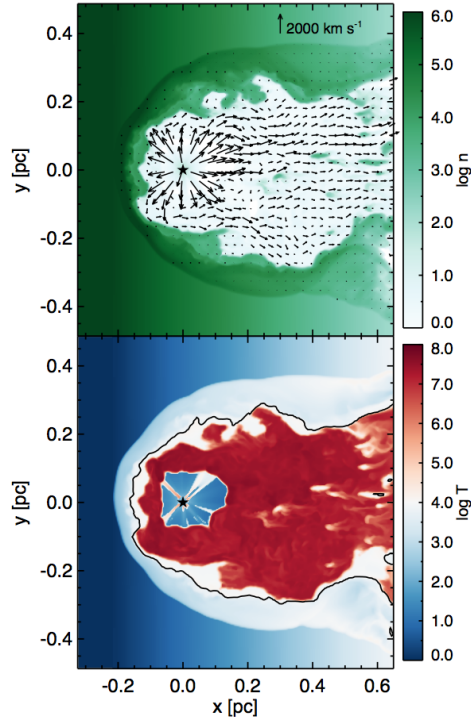
Figure 2.9 – Number density (in cm^{-3}) together with the velocity field (in km s^{-1}) (top), and gas temperature (in K) with ionization front marked in black (bottom) for the modified champagne flow model with mass loading after 5,000 yr from the full evaporation of all proplyd of a slice of the 3D simulation through the location of the source.

2.5.3 Modified champagne flow with mass loading

In Section 2.6, we explain why the bow shock model is not in good agreement with the observation characteristics of G29.96, while the modified champagne flow model can reproduce all the observations but the X-rays. This is due to the high temperatures of the gas inside the bubble as caused by the reverse shock. Therefore, we introduce mass loading from photo evaporating proplyds to the modified champagne flow only, our preferred model. The addition of gas inside the bubble will lower its temperature. We study here the typical temperatures that can be reached.

We run the champagne flow model, as described in Section 2.5.2, with the addition of a population of proplyds that are photo evaporating (as described in Section 2.4.6). We consider a population of proplyd as found in Orion and with mass loss rates typical of

photo evaporation processes.

Figure 2.7 and 2.8, bottom row, show the results of including mass loading in the champagne flow model. When compared with the original models (Figure 2.7 and 2.8, middle row), it is clear that the overall shape has not changed, but the inside of the bubble has structures due to the additional gas from proplyds that creates a turbulent medium, efficiently mixing cold and hot gas. The average temperature of the gas inside the bubble decreases by about an order of magnitude, while the density increases.

Considering a typical mass of a proplyd of 2×10^{-2} $M_\odot$ with constant mass loss rate of 10^{-6} $M_\odot$ yr^{-1}, the lifetime of a proplyd is 20,000 yr. After 20,000 yr all the proplyds should have run out of gas, therefore we continue to run the simulation without mass loading for another 5,000 yr to investigate how long it takes to increase the temperature of the bubble again. Results are shown in Figure 2.9. After 5,000 yr, the gas around the star has reached again the high temperatures of the initial champagne flow model, because all the evaporated gas is transported towards the tail of the region.

2.6   Comparison with observations

In this section we carry on a detailed comparison of out simulations with observations. We compare with the [Ne II] 12.8 μm fine-structure line mapping (Zhu et al. 2008), the 2 cm radio maps (Wood & Churchwell 1989) and the X-ray SED.

2.6.1   Simulated radio emission measure maps

We generate simulated emission measure maps for the radio emission by assuming Bremsstrahlung radiation. First, we rotate rigidly the box around one axis at a given angle, the viewing angle. Then, we pick a line of sight along any of the new axis, depending how we want to project the object. Since our simulations are approximately axis-symmetric along the x-axis cutting through the source, it is interesting to rotate along the y-axis cutting through the source and look at the object head and tail at different viewing angles. After the box rotation, the radio continuum maps are generated by first calculating cell by cell the free-free absorption coefficient at frequency ν (Rybicki & Lightman 1979)

$$\alpha_\nu^{ff} = 3.7 \times 10^8 T^{-0.5} Z^2 n_e^2 \nu^{-3}(1 - \exp(-h\nu/kT))g_\nu, \tag{2.6}$$

where T is the gas temperature, Z is the atomic number, n_e is the electron density, h is the Plank constant, k the Boltzmann constant in cgs, and g_ν is the gaunt factor at frequency ν. The optical depth at distance r is

$$\tau_\nu = \int_0^r \alpha_\nu^{ff} ds. \tag{2.7}$$

We integrate again to find the brightness temperature $T_{b\nu}$ as

$$T_{b\nu} = \int_0^\tau T e^{-\tau_\nu} d\tau_\nu. \tag{2.8}$$
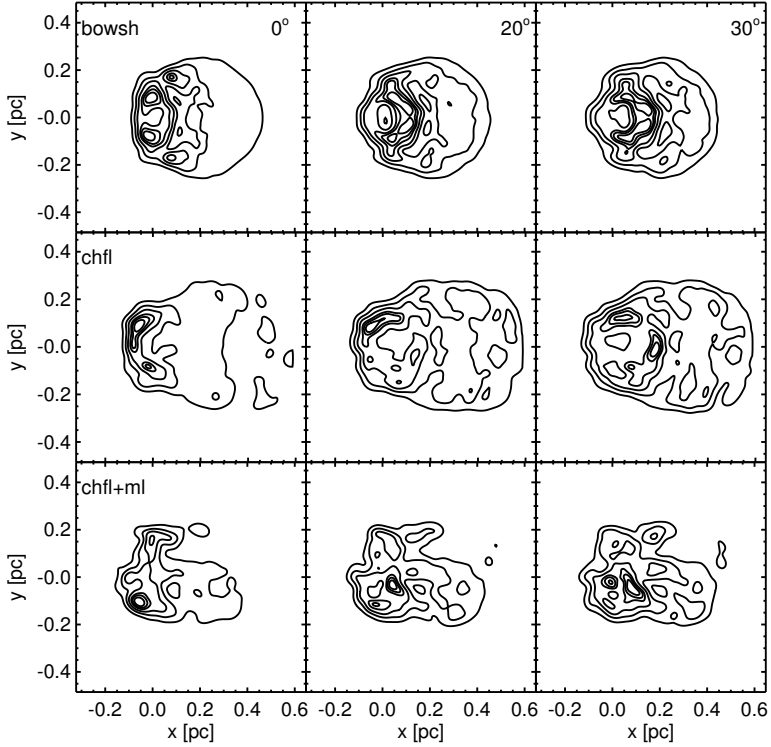
Figure 2.10 – Simulated radio emission measure maps for the three models at age 20,000 yr: bow shock model (top row), champagne flow model (central row), and champagne flow with mass loading model (bottom row). We rotate the source by 0, 20 and 30 degrees (respectively, from left to right columns) rigidly around the y axis and then project onto the plane of the sky.

We finally derive the surface brightness (Mac Low et al. 1991)

$$S = 2 \times 10^{23} k T_{bv} \Omega_{bm} / \lambda^2 \text{ Jy beam}^{-1}, \tag{2.9}$$

where Ω_{bm} is the solid angle subtended by the beam. We then convolve the image with a gaussian with a full-width-half-maximum typical of the radio observations of Wood & Churchwell (1989).

Figure 2.10 shows the radio expected emission of the bow shock, modified champagne flow and modified champagne flow with mass loading model. We change the orientation of the source by 0, 20 and 30 degrees with the head towards the observer. The best models that matches the observations is the champagne flow model that can reproduce the cometary shape of the radio emission (Arthur & Hoare 2006). The head is brighter

and has an arc-like structure, and the extended emission follows the cometary shape of the region. Since the swept-up shell of the bow shock model does not break open, the resulting radio emission is more spherical than arc-like. For this reason, we believe that in the conditions of G29.96 – very high ambient medium density – this model is not appropriate to explain this region. When we introduce mass loading, the region is more turbulent and it is hard to discern the cometary shape.

The orientation of the source with respect to the observer is important for the morphology of the radio emission. We find that the best match is achieved with a very small angle of rotation, about 10 degrees. Arthur & Hoare (2006) suggested an angle of 20 degrees to be the best fit, however, they did not build a model specific for G29.96 and they simply derive the value from trends found in their numerical study. Since the angle is so small and makes little difference to the results, for simplicity, we show the rest of the results without any rotation.

2.6.2   Velocity maps

In order to compare our simulations results with the observation of [Ne ɪɪ] 12.8 μm fine-structure line mapping (Zhu et al. 2008, Figure 2.2), we create velocity maps as follows. We take the velocity component along the z-axis to be the line of sight velocity, we then divide it in velocity bins. We add a normalized gaussian line profile to account for the thermal broadening of the line, considering the temperature of the simulation. Finally we add a point spread function typical for the observations. Figure 2.11, 2.12 and 2.13 show velocity maps for the bow shock, the modified champagne flow and the champagne flow with mass loading at age 20,000 yr.

The observations (Figure 2.2) show two features in the ionized gas: a clear arc-like structure at the rest frame velocity (98 km   s^{-1}), and a somewhat disturbed gas at blue- and red-shifted velocities. In the case of the bow shock, the H ɪɪ region never breaks open, seen in the velocity maps as a round feature, where the tail is also visible. Therefore, for the case of G29.96 we exclude the bow shock model.

For the other two models we find that, on one hand, the champagne flow model can best reproduce the rest frame arc-like structure, on the other hand, the model with mass loading is able to reproduce the disturbances in the ionized gas at blue- and red-shifted velocities. When mass loading is introduced, the cometary shape is less clear. The injection of gas from proplyds disturbs the dynamics of the region, generating a more turbulent picture. The bright arc-structure is still recognizable at zero velocity, but almost absent in the blue- and red-shifted channels. Both champagne flow models give a good representation of the dynamics of the ionized gas. Observations show that a less turbulent way to mass load the gas would be the best model to explain both arc-like feature and turbulences.

2.6.3   X-ray luminosity and spectral energy distribution

The diffuse soft X-ray emission observed towards G96.96 indicates the presence of a diffuse plasma at a temperature $< 10^6$ K. Both bow shock and modified champagne flow models predict an average temperature of the shocked stellar wind gas of $\sim 5 \times 10^7$ K.
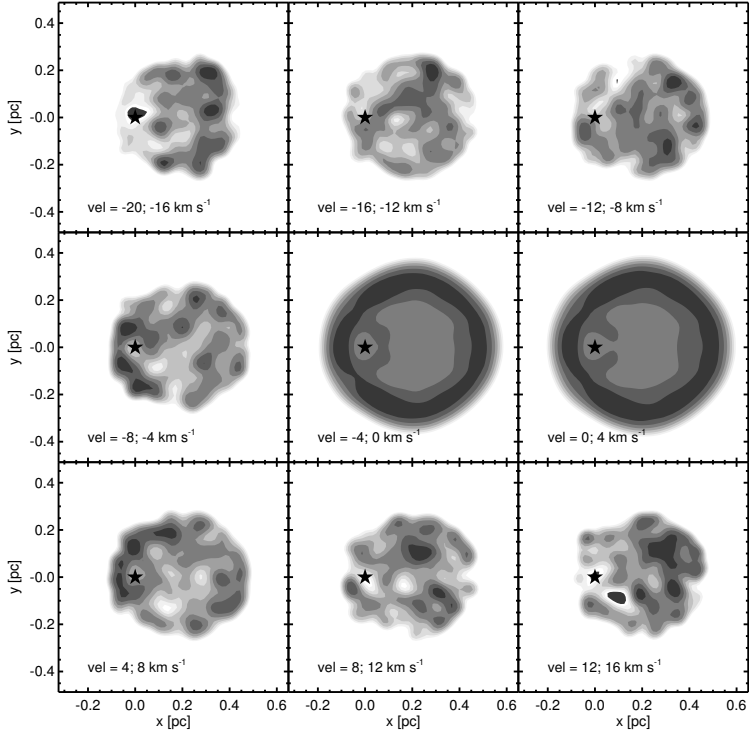
Figure 2.11 – Prediction of velocity bin maps of [Ne II] line observations (Zhu et al. 2008) for the bow shock model at 20,000 yr.

Only when mass loading is included the temperature of the shocked stellar wind gas cools to $\sim 4 \times 10^6$ K. Therefore, mass loading is an efficient way to cool the shocked gas and can explain the observed diffuse soft X-ray emission.

We also calculate the total expected X-ray luminosity by assuming Bremsstrahlung radiation only. We take the emissivity of the Bremsstrahlung, that depends on density and temperature of the gas in the simulation, and integrate over the volume and a frequency range (0.5-8.0 keV) (Sarazin 2009). Results are shown in Table 2.1. We find that, while we are able to explain the diffuse soft X-ray component, we are unable to justify the lack of diffuse hard X-ray emission. However, we did not include the extra cooling in the hot plasma due to the dust. Dust is not contained in the stellar wind, but it might be introduced in the bubble from proplyd evaporation. Therefore, in the model with mass loading and extra cooling can be assumed. Indeed, the presence of dust can enhance the cooling rate up to a factor of 100 for temperatures 10^7-10^8 K (van Buren et al. 1990, Dwek 1987,

33
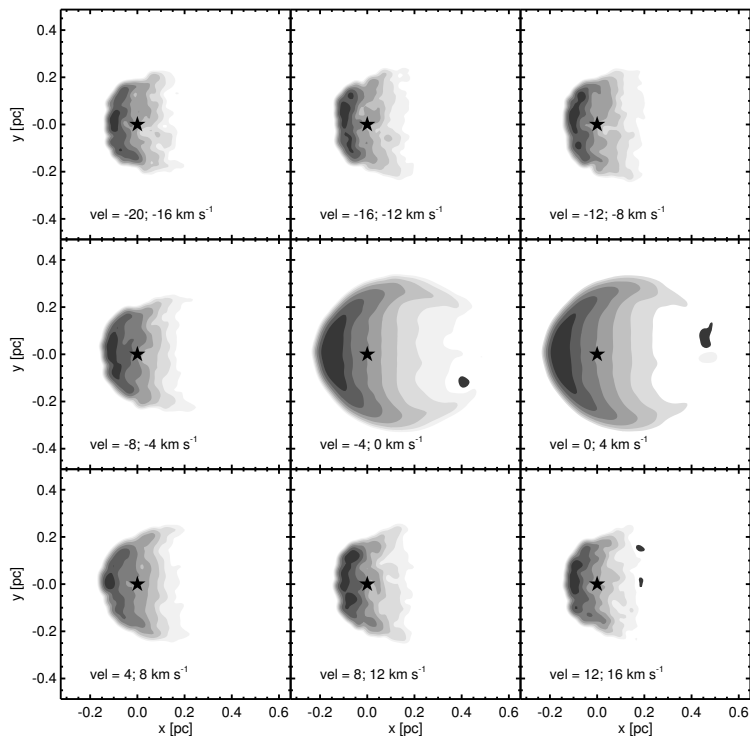
Figure 2.12 – Prediction of velocity bin maps of [Ne II] line observations (Zhu et al. 2008) for the modified champagne flow model at age 20,000 yr.

Everett & Churchwell 2010).

2.6.4 Summary

We carried out three-dimensional numerical simulations aimed at understanding the interaction of the stellar winds with its surroundings for the prototypical cometary UC H II region, G29.96. Radio maps of this source show the morphology of the ionized gas, while [Ne II] line emission maps display the dynamics of the gas. Furthermore, we have constrained the stellar type and the mass loss rate of the ionizing source, indicating a strong stellar wind. Finally, we have detected hard X-rays from the star – either from a colliding wind binary or from a coronal region – and only a small component for diffuse soft X-rays. The latter demonstrates that the plasma in the bubble is not very hot.

With all the parameters constrained by observations, we investigate three models for
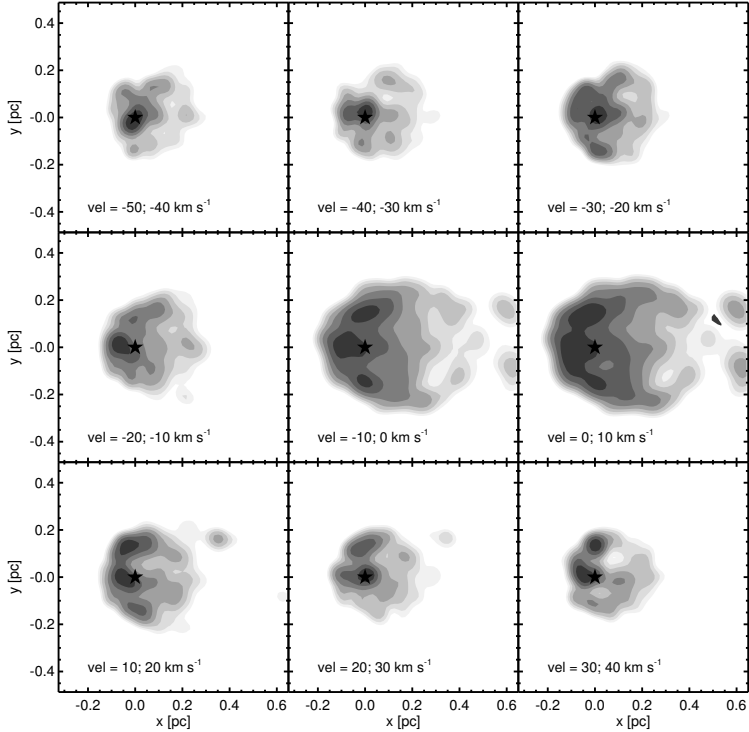
Figure 2.13 – Prediction of velocity bin maps of [Ne II] line observations (Zhu et al. 2008) for the modified champagne flow model with mass loading at age 20,000 yr.

the evolution of the source: bow shock, modified champagne flow and modified champagne flow with mass loading. We exclude the bow shock model because it fails in reproducing both the morphology of the region, as seen in the radio, and the dynamics of the ionized gas, as revealed by the [Ne II] line emission. The only two assumptions in the bow shock model are the velocity of star (10 km s^{-1}), and the density of the uniform medium (5×10^4cm^{-3}). Besides observations indicating that the density in the source surroundings is quite high (Martín-Hernández et al. 2002), we need such a high value for the ambient density to keep the source confined to a small radius. However, the high ambient density also causes the model to not succeed in reproducing the morphology. Indeed, under these conditions the swept-up shell cannot break open at the tail of the region resulting in a different morphology in the radio. Even more telling, the calculated dynamics does not reproduce the [Ne II] velocity maps.

In contrast, the modified champagne flow is able to reproduce both the cometary mor-

phology of G29.96 the radio emission and the velocity maps of [Ne II] line emission show-
ing the typical bright arc structure that fades towards the tail of the region. However, both
classical models – bow shock and modified champagne flow – predict intense diffuse soft
X-ray emission inconsistent with the observations. Indeed, the shocked stellar wind gas
of both models reach temperatures of $\sim 4 \times 10^7$ K, that should have been seen in the soft
X-ray band. It indicates that there must be a mechanism at work that cools the shocked
stellar wind gas by about one order of magnitude.

We introduced mass loading from proplyd evaporation in the modified champagne
flow model. Adopting a reasonable proplyd distribution, the injection of mass in the
shocked stellar wind region cools the gas by one order of magnitude and it can explain
the X-rays. However, the overall morphology of the region gets so disturbed that the good
morphology match we obtain by the modified champagne flow model vanishes.

We conclude that the surrounding core must have a density gradient that generates
the cometary shape. We emphasize that the stellar parameters – effective temperature
and mass loss rate – are well constrained by our observations. There is some leeway in
the adopted density distribution for the surrounding core. However, the density of 5×10^4
cm^{-3} is in good agreement with observation of the ionized gas density (Martín-Hernández
et al. 2002). The scale height of the density distribution (0.1 pc) leads to a morphology
which is in good quantitative agreement with the observations (cf., Figure 2.1 and 2.10).
In addition, this model reproduces the observed velocity field quantitatively (cf., Figure
2.2 and 2.12). However, the classical interaction of stellar winds with the surrounding
does not explain the X-ray observations. Mass loading mechanisms are able to lower the
temperature of the shocked gas, but proplyd evaporation makes the gas turbulent and pre-
vent the model to explain the morphology of the region. A more regulated mass loading
effect must take place, one example could be mass loading from the swept-up gas shell.

2.6.5 Discussion

The large variety of observed UC H II in morphology and kinematics has been explained
by various models. Detailed numerical work on the interaction of stellar winds with the
ambient medium in the presence of radiation has been carried out by Freyer et al. (2003,
2006) discussing the appearance of thin shell instabilities and their effects on the dynam-
ics. In a broader contest, Arthur & Hoare (2006) explored a combinations of bow shock
(van Buren et al. 1990) and champagne flow models (Tenorio-Tagle 1979, Bodenheimer
et al. 1979, Yorke et al. 1983) in order to identify the characteristic of each model and
their predictions to compare with observations.

We have studied in details the source G29.96 as a prototype of cometary UC H II. For
the particular case of G29.96 we excluded bow shock models. However, we emphasize
that it does not exclude the validity of this model for other sources. Numerical work has
been carried out mostly in the context of runaway stars (Raga et al. 1997, Comeron &
Kaper 1998) showing appearance of structures as a result of the interaction between the
fast stellar wind of a runaway star and the surroundings, complicated by the presence of
magnetic fields (Mackey et al. 2013).

We found that the classical models alone – bow shock, and modified champagne flow

– cannot explain the lack of diffuse soft X-rays observed towards G29.96. Mass loading of the hot plasma is a promising mechanism to cool the hot shocked gas. However, evaporation from proplyds will dominate the morphology and dynamics of the region. As a result, the adopted spatial distribution of the proplyds has to be highly tailored (Dyson et al. 1995) and that is not very realistic. The presence of dust in the hot plasma can enhance the cooling rate as much as a factor of 100 for temperatures $10^7 - 10^8$ K (van Buren et al. 1990, Dwek 1987, Everett & Churchwell 2010). Although stellar winds do not have dust, we can assume that some dust is mixed in the hot gas from proplyd evaporation. In such scenario, the gas can cool more efficiently and less mass loading from proplyds is necessary to lower the temperature by one order of magnitude. Therefore, less dynamical disruptions will happen in the bubble.

Besides the morphology, another problem with mass loading from proplyds is that after a short time all the proplyds in the vicinity of the ionizing star are fully photo evaporated and the shocked gas starts warming up again. In a recent paper, Gritschneder & Burkert (2013) studied the dynamics of proplyds. They consider proplyd formation to happen in the expanding shell of an H ɪɪ region, as the effect of triggered star formation. Those newborn stars have an initial velocity that tends to push them away from the ionizing star, leaving the H ɪɪ region free of proplyds. However, Gritschneder & Burkert (2013) show that in high density cases, such as Orion, stars have enough time to be gravitationally pulled back towards the ionizing star. G29.96 is similar to Orion in terms of densities, therefore there is the possibility that proplyds return might keep the hot gas mass loaded and at lower temperatures for longer timescales than considered by us.

Other explanations that could explain the absence of X-rays have been suggested in the past. One is the blowout scenario: the wind kinetic energy mostly stays in the form of kinetic energy rather than thermalizing in a strong shock. This would happen if the volume of turbulent molecular clouds is mostly low-density material, with only small pockets of high density material (Mac Low et al. 2007). However, while this is a reasonable general scenario for the interaction of stars with their surroundings, it is unlikely to be able to explain the observed morphology of this particular source. Another possibility is that mass loading happens at the contact discontinuity through conduction mechanisms: electrons from the hot shocked gas transfer energy to the ionized gas shell, the hot gas cools and mass is injected from the ionized gas into the hot gas. Arthur (2012) studied conduction in unidimensional simulations and found a significant thickening of the ionized gas shell and lower temperatures of the shocked gas. One final suggestion is magnetic turbulent layers: the introduction of magnetic fields into the molecular cloud prior to H ɪɪ region expansion can lead to thick turbulent mixing layers with lower temperatures at the wind/cloud boundary (Kahn & Breitschwerdt 1990 and Falceta Gonçalves, personal communication).

2.7   Conclusions

We present a broad study of UC H ɪɪ regions combining X-ray observations of the hot gas with spectroscopic study of the properties of the ionizing star, and a hydrodynamical study

of the evolution of these regions. We focusing our analysis on G26.96, a very well-studied typical UC H II region.

We collected observations of the *H*- and *L*-band spectra of the ionizing star of G29.96. Combined with the *K*-band from Martín-Hernández et al. (2003), we have five emission lines: Br 11, He II $\lambda16923$, He I $\lambda17007$, Br γ and Br α.

We used the genetic algorithm developed by Mokiem et al. (2005) to fit the observed lines with synthetic line profiles to constrain the mass loss rate. The best-fit parameters are $T_{\text{eff}} = 39.8^{+7.6}_{-1.9}$ kK, $\log g = 3.66^{+0.28}_{-0.16}$ and $\log \dot{M} = -5.15^{+0.1}_{-0.2}$ $M_{\odot}\text{yr}^{-1}$.

We observed G96.96 with Chandra X-ray Observatory using ACIS-I. The spectral hardness of the ionizing star of G29.96 shows that the source is not a typical single star, indicating the presence of a colliding-wind binary and/or has a substantial magnetic field. We find some evidence for a soft X-ray diffuse component, but no detection of a diffuse hard component.

We use 3-dimensional hydrodynamic code with radiative transfer to model the UC H II region. We create three models of the expansion and evolution of the H II region. The first one is the bow shock model characterized by an ionizing star with a stellar wind that moves through a uniform density medium. The second one is the modified champagne flow model, where the ionizing star with stellar winds is in a medium with a density gradient. The third model is the second models with the addition of mass loading due to proplyd evaporation.

For each model, we produce observables that we directly compare to observations. From the comparison with the radio maps, we exclude the bow shock model. With the very high densities of the medium required to keep the UC H II region small, the swept-up shell cannot break open, resulting in a shape of the ionized gas too spherical.

Thanks to the X-ray observations, we exclude the modified champagne flow model. Such model predicts the presence of a diffuse component of the soft X-ray, that is not observed. The model that can explain all the simulations at once is the modified champagne flow model with mass loading. Mass loading acts as a coolant of the hot gas of the shocked stellar wind.

2.8   Appendix: Code testing

The FLASH HC code was extensively tested as part of the radiative transfer code comparison project, the Rijkhorst et al. (2006) version used in Iliev et al. (2006) and the updated version we use in this work in Iliev et al. (2009). In this section, we extend those tests with new ones more suited to the high density regimes of interest in this work. We also reproduce the work of Arthur & Hoare (2006) to test our code against a known result for a more detailed stellar wind problem.

Expansion of an H II region in a uniform density medium

The tests performed in the RT code comparison project (Iliev et al. 2006, 2009) focused on physical conditions commonly found in the intergalactic medium, however the condition

in the interstellar medium are very different. Namely, the densities of interest in this work are several orders of magnitude higher than those used for the code comparison tests. In order to confirm that the code is appropriate for use in those density regimes, we perform two test problems with known analytic solutions previously used in the code comparison project.

The first test we perform is the variation on Test 1 from Iliev et al. (2006), which is the expansion of an H II region around a single ionizing radiation source embedded in a static, hydrogen-only uniform density medium. The only difference to the Iliev et al. (2006) test is that we increase the density of the medium, n_H, by six orders of magnitude, to $n_H = 10^3$ cm^{-3}.

There is a well-known analytic solution for the evolution of ionization front radius of the H II region expected in this case, assuming a constant temperature in the gas and infinite photoionization cross-section:

$$r_I(t) = \mathcal{R}_s(1 - e^{-t/t_{rec}})^{1/3},\tag{2.10}$$

where $t_{rec} = (\alpha_B(T)n_H)^{-1}$ is the recombination time scale and $\mathcal{R}_s$ is the final size of the H II region obtained by equating the number of recombination in the H II region with the number of photons emitted by the source $\mathbb{N}_{Lyc}$, the so called Strömgren radius,

$$\mathcal{R}_s = \left(\frac{3\mathbb{N}_{Lyc}}{4\pi\alpha_B(T)n_H^2}\right)^{1/3}.\tag{2.11}$$

The setup parameters are as follows. The simulation volume is cubical with side dimension $L_{box} = 6.6$ pc. The computational grid used to represent the volume is uniform, with 128 cell per box side. The medium is static, hydrogen-only gas with uniform number density $n_H = 10^3$ cm^{-3} and kept at constant temperature $T = 10^4$ K throughout. A source of monochromatic photons of energy $E_\gamma = 13.6$ eV is placed at the corner of the simulation volume, at coordinates $(0, 0, 0)$, and emits $\mathbb{N}_{Lyc} = 5 \times 10^{48}$ photons per second. For these parameters, the recombination time scale is $t_{rec} = 122.31$ years. We run the simulation for 500 years.

In Figure 2.14 we show the position of the ionization front radius as a function of time compared with the analytic solution from Eq. 2.10. The difference with the analytic solution is caused by the fact that the photoionization cross section in our simulation is not infinite, therefore the ionization front in the simulation has a finite thickness and photons can penetrate deeper into the neutral medium than assumed in the analytic solution. This fact was already discussed in Iliev et al. (2006) and our result agrees with the behavior of all codes shown there. We conclude that FLASH HC is able to reproduce the analytic solution for the evolution of an H II region in a static medium in the density regime of interest for our work.
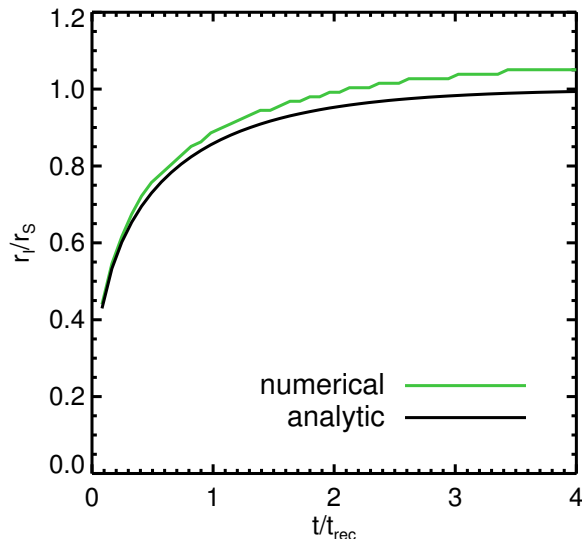
Figure 2.14 – Expansion of the ionization front in uniform medium at fixed temperature. The plot shows in full black line analytic expansion of the radius as a function of time as described in Eq. 2.10; and the numerical results in gray.

Pressure supported expansion of an H II region in a uniform density medium

The second test we perform is a variation on Test 5 from Iliev et al. (2009), which is the classical problem of the expansion of an ionization front due to a single ionizing radiation source embedded in a uniform density medium. As for the previous test, the only difference to the Iliev et al. (2009) test is that we increase the density of the medium, n_H, by six orders of magnitude, to $n_H = 10^3$ cm^{-3}.

We focus our analysis on the evolution of the ionization front after the Strömgren radius has been reached. This first phase happens on a recombination timescale, that is very short compares to the time evolution we want to reach in this work. Once the ionization front has reached the Strömgren radius, the pressure of the ionized gas within it is higher that the pressure of the ambient medium. Such overpressure drives the expansion of the ionization front beyond the Strömgren radius, as predicted by the classical Spitzer (1978) solution:

$$r_I = R_{st}\left(1 + \frac{7c_s t}{4R_{st}}\right)^{4/7} \tag{2.12}$$

where c_s is the sound speed in the ionized gas.

We perform the test with the very similar input parameters as before but with hydro-

dynamic effects included, meaning that the gas is not isothermal. The setup parameters are as follows. The simulation volume is cubical with side dimension $L_{box} = 6.6\,pc$. The computational grid is uniform, with 128 cell per box side. The medium has a uniform number density $n_H = 10^3\,cm^{-3}$ and at initial temperature $T = 10^2\,K$. A source of monochromatic photons of energy $E_\gamma = 13.6\,eV$ is placed at the corner of the simulation volume, at coordinates $(0, 0, 0)$, and emits $\mathbb{N}_{Lyc} = 5 \times 10^{48}\,s^{-1}$. For these parameters, the recombination time scale is $t_{rec} = 122.31\,yr$. We run the simulation for 1.5 Myr.
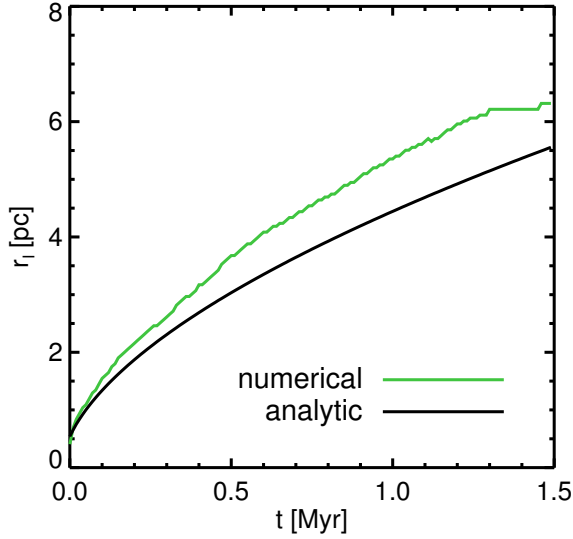
Figure 2.15 – Expansion of the ionization front in uniform medium with hydrodynamic response. The plot shows with black line the analytic expansion of the radius as a function of time as described in Eq. 2.12, and with gray line the numerical result of the simulation.

Figure 2.15 shows the results of the test. We include the Spitzer analytic solution as described in Eq. 2.12 and the numerical test. We find reasonable good agreement throughout the expansion between code and analytic solution. As found by Iliev et al. (2009), the global dynamics of the ionization front at this stage depend primarily on the temperature of the ionized gas that driver the overall expansion.

The H II region radial evolution is overestimated. Iliev et al. (2009) noticed that the analytic solution describes well the early and late evolution of the expansion, but not the intermediate. Furthermore, the radial evolution does not match the $r^{4/7}$ expansion predicted by the analytic solution, but it approaches it at late times as the radius of the front becomes larger, also seen in Iliev et al. (2009). We conclude that FLASH HC reproduces reasonably well the analytic solution for the evolution of an H II region in a non-static medium in the high density regimes.

Stellar wind

The interaction of stellar winds with a medium is a problem that has been studied in many different astrophysical contexts. More recently there has been an interest in studying the interaction of stellar winds with the radiation of the star. In particular, the work of Freyer et al. (2003, 2006) and Arthur & Hoare (2006) explored this in detail. The extensive work done allow us to use such a setting as a test case for our code. As far as we know, the FLASH HC code has never been used in a similar setting, and we want to check the reliability of our code. We set up a test as the Arthur & Hoare (2006) expansion of an H ɪɪ region in the presence of a stellar wind. The box size is 0.15×0.15 pc with constant density medium 6000 cm^{-3} and temperature 300 K. The ionizing star is located at the corner of the box in the origin of the axis and it is a blackbody of effective temperature 30000 K. We set the mass loss rate is 10^{-6} M$_\odot$ yr^{-1} and terminal wind velocity 2000 km s^{-1}. We performed the same test in both 2D and 3D and at different resolutions. For the sake of comparison with Arthur & Hoare (2006) we show first results of the 2D models. The number density together with the velocity field, the gas temperature, and the degree of hydrogen ionization after 200 and 500 yr from the beginning of the simulation are shown in Figure 2.16(a) and 2.16(b) respectively.

Figure 2.16(a) shows the stellar wind model at age 200 yr. The ionization front moves quickly approximately to the location of the Strömgren radius, $R_{st} \sim 0.07$ pc, in a recombination timescale ~ 1.7 yr. The pressure of the ionized gas is higher than the cold medium causing the ionization front to expand further. This expansion is smaller than the stellar wind but still visible in the small arrows of the velocity field in the outer shell. The stellar wind bubble expands into the ionized and preheated ambient medium. Cooling in the outer shell of swept-up gas is efficient and causes the shell to collapse to a thin layer. Due to thin-shell instability (Vishniac 1983) dense knots are produced along the shell, causing a higher optical depth along rays going thought them. This causes the rippling of the photoionization front, and the shadowing effect visible in the plot. The free-flowing wind is heated by the reverse shock at ~ 0.03 pc to very high temperatures of about 10^8 K.

Figure 2.16(b) shows the evolution at 500 yr. At this stage the thin shell of swept-up gas has reached a radius ~ 0.06 pc and the thin shell instability has evolved in more dense knots and a more perturbed shell. The degree of ionization went from almost 100% to 5% in the region between the initial ionization front and the thin shell due to trapping of the photons by the high dense swept up shell region. Spikes of ionized gas are characteristic of the instability and represent the propagation of the ionization fronts in collimated beams through gaps in the knotty shell.

We further studied the thin-shell instability modes at higher refinement to confirm that they have no influence on the outcome of our simulations. In Figure 2.17(a) and 2.17(b) we present the same stellar wind simulation as above for refinement level 9. Also Freyer et al. (2003) proved that the energy budget is not influenced by the refinement. Comparing Figure 2.16(a) and 2.16(b) with 2.17(a) and 2.17(b) it is possible to see that the location of the ionization front and of the swept-up shell does not change with refinement. As expected, the main change with increasing resolution is the level of details that are found.
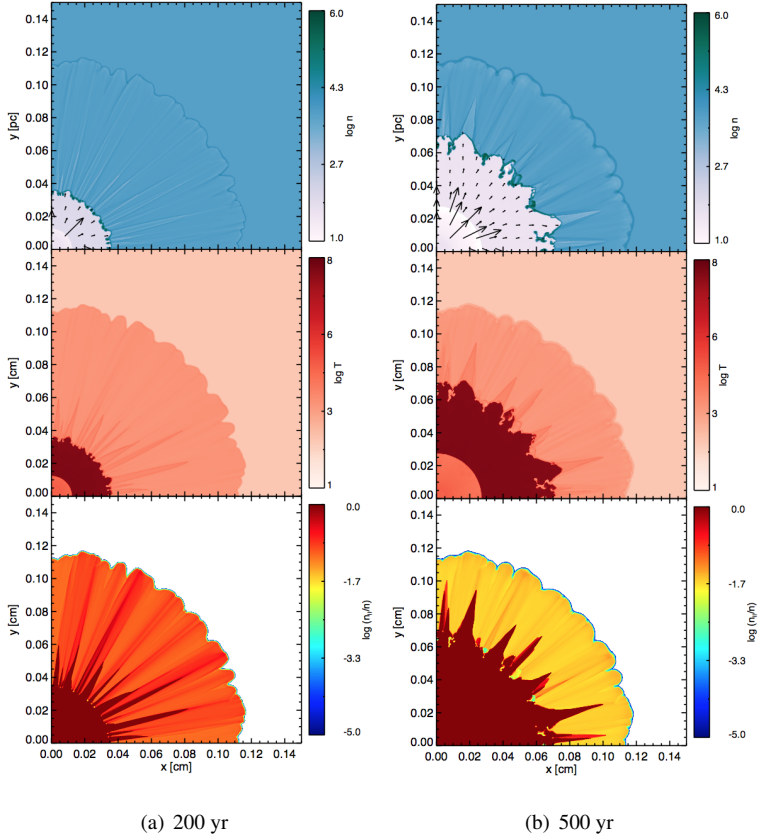
(a) 200 yr   (b) 500 yr

Figure 2.16 – Number density together with the velocity field (top), gas temperature (middle), and degree of hydrogen ionization (bottom) for the stellar wind model at age (a) 200 yr, and (b) 500 yr with level of refinement up to 8. The star is located at the center of the coordinate system.

The swept-up shell has the same instability modes at both levels of refinement. The structures visible at refinement level 9 can be matched to the one at refinement 8. The energetics involved in the problem do not change with resolution giving us confidence that choosing refinement level 8 is a good compromise between computational cost and level of details reached in the simulation.
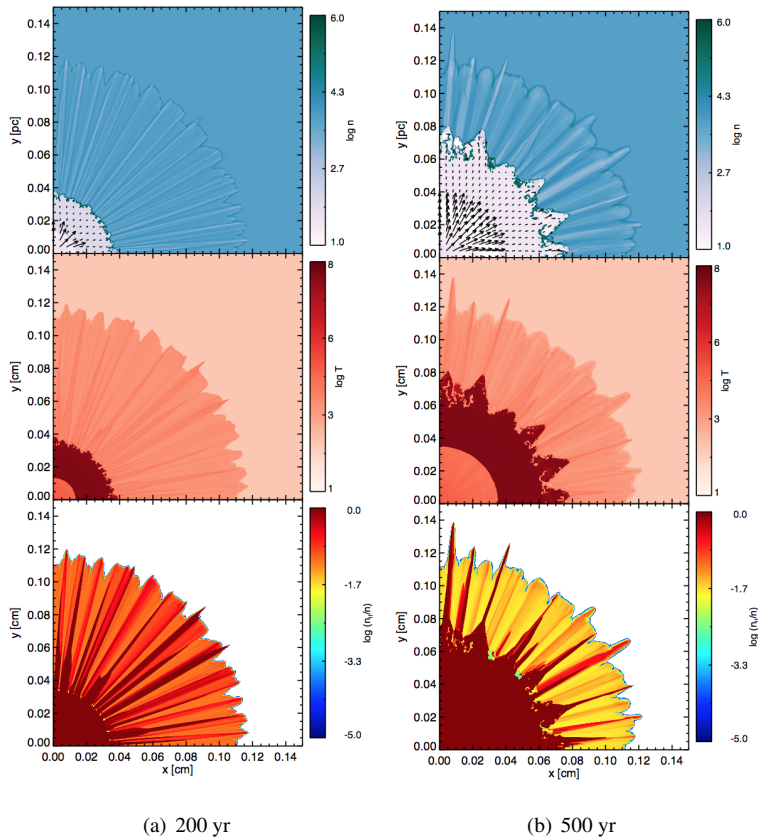
(a) 200 yr   (b) 500 yr

Figure 2.17 – Number density together with the velocity field (top), gas temperature (middle), and degree of hydrogen ionization (bottom) for the stellar wind model at age (a) 200 yr, and (b) 500 yr with level of refinement up to 9. The star is located at the center of the coordinate system.

III

A class of champagne flow H II regions with radiation pressure-driven dust waves

We investigate the evolution and the morphology a class of H II regions formed by champagne flow mechanisms in order to explain the cometary shape of the dust emission. We carry out hydrodynamical numerical simulations with radiation using the FLASH HC code. We set up a modified Bonnor-Ebert sphere density profile to represent the molecular cloud and change the location of the ionizing star offset from the center. We derive velocity and emission measure maps to compare to observations. The velocity of the gas inside the H II region reaches values up to 40 km s^{-1} at the star location, well above the minimum velocity required for a dust wave to form. We show that champagne flow models provide a natural mechanism to explain the presence of dust inside bubbles and its cometary shape. We are also able to reproduce the full range of observed morphological classes by setting the ionizing star offset from the center of the natal molecular cloud.

Silvia Verdolini, Bram B. Ochsendorf, Alexander G. G. M. Tielens
to be submitted

3.1   Introduction

The presence of dust inside H II regions as discovered by the Galactic Legacy Infrared Mid-Plane Survey Extraordinaire (GLIMPSE) survey in the mid-infrared has recently raised a new enigma regarding the evolution of interstellar bubbles. The formation and expansion mechanisms of H II regions are still under debate. When a high mass star ionizes its surrounding, the ionization front reaches the Strömgren radius on short timescales. The following stages of expansion have been examined by many authors, each taking into account different physical processes. Spitzer (1978) studied the expansion due to the effects of overpressure caused by the ionization and heating of the H II region; Castor et al. (1975) considered the mechanical energy of the stellar winds as a main driving mechanism; and Krumholz & Matzner (2009) took into account the pressure of the radiation on the gas. Draine (2011) studied the structure of dusty H II regions in static equilibrium with an external bounding pressure and found a family of solutions for the density profiles, ranging form uniform to hollow-spheres.

Ochsendorf et al. 2013a (submitted) revealed the first detection of a radiation-pressure driven *dust wave* around a massive star (σ Ori, stellar spectral type O9.5V). They suggested that the cometary shape of the dust emission is the result of the interaction between radiation pressure from the star with the dust contained in the flow of ionized gas photo evaporated from the natal molecular cloud. Similar arc-like structures in 24 μm emission of warm dust have been detected inside H II regions. Ochsendorf et al. 2013b (to be submitted) suggest that the dust distribution inside interstellar bubbles can be explained by similar dust waves. Radiation pressure from the ionizing star acts on the photo-evaporating flow from the swept up shell of the H II region. In the presence of a champagne flow, the ionized gas inside the H II region reaches velocities ~ 10 km s^{-1} at the star location setting up the conditions for a dust wave.

In this work, we extend the work of Ochsendorf et al. 2013b (to be submitted) to a broader range of parameters. We restrict our study to H II regions powered by stars that have weak stellar winds. Indeed, evidence is accumulating that winds from stars with stellar type later than O6.5V (ionizing luminosity $Q_0 \approx 48.8$ (Martins et al. 2005)) are weaker than predicted by theory (Vink et al. 2000, Puls et al. 2008, Najarro et al. 2011). We identify five H II regions following such criteria, and with different morphologies: from closed bubbles, to broken and fully open ones. In the first case, Draine (2011) theory predicts a ring-like structure in the emission measure of dust, while in the other cases we expect an arc-like structure pointing upstream of the gas flow. We investigate if H II bubbles can, without the inclusion of a stellar wind, reproduce the morphologies (as a function of density gradient and depth into the cloud) and create the conditions necessary to induce photo-evaporating flows in their interior.

The paper is organized as follows. We present a selection of five prototypical H II regions in Section 3.2 which cover well the range of morphology observed. We describe the numerical method in Section 3.4 and analyze the results in Section 3.5. In Section 3.6 we discuss how simulated H II regions compare with observed one, and what are the main implications of this work. We conclude in Section 3.7.

Table 3.1 – Bubble parameters. Electron densities are derived from the observed emission measure assuming spherical symmetry of the H II region with a uniform density distribution.

Name	l (deg)	b (deg)	d (kpc)	Diam. (pc)	$\mathbb{N}_{Lyc}$ (s^{-1})	Spec. type	τ_{MS} (Myr)	n_e (cm^{-3})
N49 (C)	28.83	-0.23	5.5[1]	4.0	48.35[1,3]	O7-8	~ 7	72
N90 (C)	43.77	0.06	6.1[1]	1.7	47.74[1,3]	O9.5	~ 11	68
RCW120(B)	348.26	0.48	1.35[2]	3.5	48.58[4]	O7-7.5	~ 6	86
N73 (B)	38.74	-0.14	9.2[1]	5.3	48.2	O8-8.5	~ 8	41
N69 (B/O)	36.29	0.72	4.9[1]	30	48.0	O9	~ 10	13

(1) Deharveng et al. (2010), (2) Zavagno et al. (2007), (3) Beaumont & Williams (2010), (4) Martins et al. (2010). Spectral types from Martins et al. (2005) assuming dwarf type stars. Main sequence lifetimes (τ_{MS}) from Ekström et al. (2012). *Notes*: (N49 and N90) Flux density S taken from Beaumont & Williams (2010) but corrected for distance from Deharveng et al. (2010). (N73): S taken from the HRDS (Bania et al. 2010). (N69): S taken from the NVSS (Condon et al. 1998).

3.2 H II region morphology

H II regions are often classified by their morphology. Churchwell et al. (2006) and the ongoing Milky Way project (Simpson et al. 2012) used the Spitzer/GLIMPSE survey to collect a large sample of Galactic bubbles and classified bubbles as complete or closed (C) or broken (B) according to their appearance in the IRAC 8 μm band. We follow this classification, however adding the 'open' morphology (O). A morphological classification does not necessarily relate to the age of the bubble; as we will investigate below, the evolution could be dominated by the region in which the H II region expands. Furthermore, while some bubbles can appear broken in IRAC 8 μm band, dense condensations exposed at longer wavelengths by Herschel can exist in the parts of the apparent broken shell. For example, in N49 (Figure 3.1(a)) the broken parts of the IRAC shell correspond to the highest columns seen in SPIRE 250 μm.

We will compare the outcome of our simulations with several prototypical examples outlined below. Limitations in the selection criteria of the prototypes include:

1) *Apparent size*. To simultaneously study the distribution of both gas and dust we need sufficient spatial resolution.

2) *Radio surveys*. High resolution radio continuum observations are needed to study the distribution of the ionized gas. Hα is rarely observed towards faint H II in the Galactic plane. Therefore, we rely on radio observations. The recent MAGPIS radio survey offers radio images at 20 cm with a resolution 6″. However, this covers only a small part of the Galactic plane (48.5 < l < 5, |b| < 0.8). In addition, the MAGPIS is one of the most sensitive surveys up to date. For bubbles of large angular size (RCW 120), lower resolution data from the NVSS (Condon et al. 1998) is sufficient for our needs.

(a) N49

(b) N90

(c) RCW 120

(d) N73

(e) N69
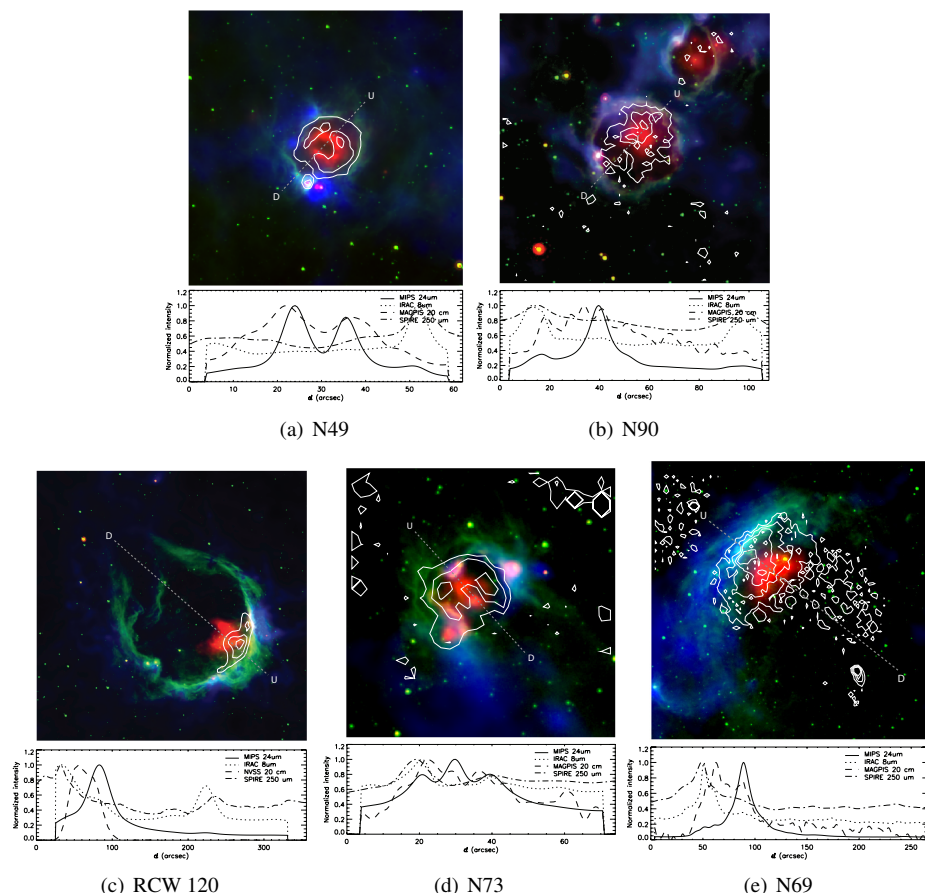
Figure 3.1 – Bubble prototypes. Red is MIPS 24 μm, green is IRAC 8 μm, and blue is SPIRE 250 μm. Overlaid are smoothed contours of radio emission of MAGPIS 20 cm (for RCW 120; NVSS). Contour levels are max-75%-50%, except for N69 where a 25% contour level is added to show the faint emission that traces the gas streaming out of the bubble. Lower panels show line profiles of cross-cuts through the maximum of the 24 μm emission, which corresponds to the apex of the arc (or ring; see N49 and N73) shaped 24 μm emission. The profiles are smoothed using a Gaussian function of width 7.5″ in order to reduce noise in the MAGPIS images. The cuts run from 'U', which stands for 'upstream', to 'D', which stands for 'downstream'.

3) *Distance*: Large scale surveys like the Green Bank Telescope H II region Discovery Survey (HRDS) (Bania et al. 2010) are trying to solve the near and far kinematic distance ambiguity by measuring radio recombination lines (RRL) (e.g., Anderson et al. 2012). However, the distance towards a lot of bubbles remain uncertain. In our sample selection we only use sources of which the distance ambiguity is resolved.

With the distance known, we estimate the amount of Lyman continuum photons, $\mathbb{N}_{Lyc}$, from the integrated radio fluxes necessary to maintain the ionization in the H II region, assuming optically thin free-free emission, using the following relation (Condon 1992):

$$\mathbb{N}_{Lyc} = 7.54 \times 10^{46} \left(\frac{F_\nu}{\text{Jy}}\right)\left(\frac{\nu}{\text{GHz}}\right)^{0.1} \left(\frac{d}{\text{kpc}}\right)^2 \left(\frac{T_e}{10^4\,\text{K}}\right)^{-0.45} \text{s}^{-1}, \qquad (3.1)$$

where F_ν is the flux at frequency ν, d is the distance of the source and T_e is the electron density.

Table 3.1 lists the properties of the selected bubble sample. For each bubble, we compare emission maps at a multitude of wavelengths:

1) *Spitzer*/IRAC 8 μm from the Glimpse survey (Benjamin et al. 2003), which traces PAH emission coming from the PDR located at the inner boundary of the swept up shell.

2) *Spitzer*/MIPS 24 μm from the MIPSGAL survey (Carey et al. 2009), which traces warm dust (50-150 K) emission mainly coming from both the swept up shell and the interior of the bubbles.

3) *Herschel*/SPIRE 250 μm from the Hi-Gal survey (Molinari et al. 2010), tracing cool (10-40 K) dust emission from dense condensation containing larger columns of material.

4) *VLA* 20 cm images from the MAGPIS survey (Helfand et al. 2006), tracing free-free continuum emission from ionized gas.

3.2.1 'Closed' bubbles

As predicted by the Draine (2011) static solution, radiation pressure acting on dust grains inside the bubble pushes the dust towards the walls of the H II region, seen as a ring structure in emission measure. Several apparent closed bubbles, such as N49 (Fig 3.1(a), (Draine 2011)) and W3A (Salgado et al. 2012), show such ring features. The line profiles at 24 μm and 20 cm show that gas and dust inside the bubble are spatially coupled. We note that Draine (2011) concludes that the gradient inside N49 can not be due to radiation pressure on dust alone and that a stellar wind likely contributes to the inner cavity. Indeed, the N49 ionizing star is at the limit that defines stars with weak winds, making it difficult to exclude the effects of stellar winds without a more detailed investigation.

3.2.2 'Broken/open' bubbles

From Figure 3.1(c) to 3.1(e), broken (B) and/or open (O) bubbles are shown in increasing stages of opening or shell-disruption. We find a clear separation of the ionized gas and dust inside H II regions, as traced by the cross cuts in Figure 3.1(c). The sequence could be interpreted as an age progression: the bubbles expand to large radii, which leads to an increasingly large 'opening' of the region (N73 and N69). Eventually, a bubble can

Table 3.2 – Initial Density

	$\log \max(n)$	$\log \bar{n}$	R_{cl} [pc]	M_{cl}[$M_\odot$]	P_{env} [K cm^{-3}]
A	4.4	2.4	4.7	5.6×10^4	6×10^5
B	5.8	3.5	4.6	6.9×10^5	6×10^5
C	5.8	3.8	4.7	1.4×10^6	6×10^6
D	5.8	4.2	7.1	3.3×10^6	6×10^6

appear as a flat ionization front being evaporated by the ionizing source ('σ Ori-like': see Ochsendorf et al. 2013a, submitted).

3.3 Dust waves

Photo-evaporation flows inside H II bubbles can be caused by either a density gradient or the disruption of the swept-up shell, ultimately characterized by the ejection of the ionized gas in the surrounding medium. A flow of ionized gas will drag along dust in its way by coupling through the drag force. The coupling efficiency between dust and gas depends on the flow parameters (in particular, the velocity v_f and density n_H of the flow) and the intrinsic momentum of the grains. This allows us to derive properties of the dust as soon as the flow parameters are specified. Depending on the coupling efficiency, we can distinguish between a *dust wave*, where dust is stopped by radiation pressure from the ionizing source and decouples from the gas, and a *bow wave*, where dust is stopped and gas stays coupled. Thus, the former is characterized by an arc structure in the dust, while the latter has an arc structure in dust and gas emission. Regardless of the coupling between gas and dust, photo-evaporation flows provide a natural explanation for the presence and arc-like morphologies of dust within H II regions (Ochsendorf et al., 2013a submitted), typically observed at 24 μm (see Figure 3.1) and indicative of dust grains of temperature $\sim$ 50-100 K residing within the harsh conditions of the H II regions.

3.4 Numerical method

We carry out hydrodynamical simulations using the code FLASH HC, a modified version of the FLASH code (Fryxell et al. 2000) that includes a Hybrid Characteristics radiative transfer scheme developed by Rijkhorst et al. (2006). The FLASH code is a publicly available, block-structured, adaptive mesh refinement (AMR) hydrodynamics code with modular design and scalable to tens of thousands of processors. The Hybrid Characteristics (hereafter HC) is a ray-tracing radiative transfer scheme designed specifically with FLASH block structure in mind. Since its introduction by Rijkhorst et al. (2006), we made several improvements to the HC scheme that are described in Raicevic (2010) and Chapter 2. The updated version of the scheme was employed in the radiative transfer code comparison project by Iliev et al. (2009).
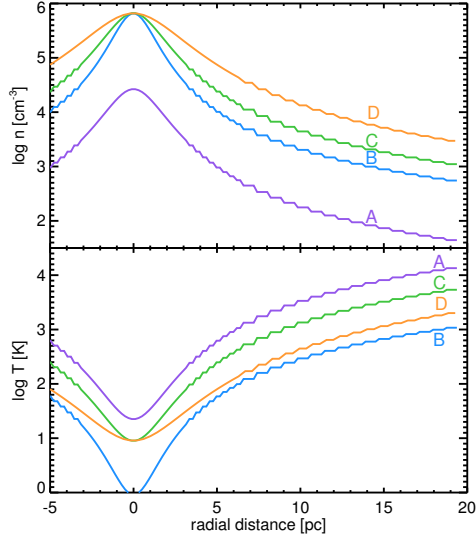
Figure 3.2 – Density and temperature profiles of the initial condition along the x-axis. We generate four clumps with a density profile similar to a Bonnor-Ebert sphere, but in pressure equilibrium.

3.4.1 Setup

The computational domain consists of a Bonnor-Ebert sphere density profile, modified to be in pressure equilibrium. A Bonnor-Ebert sphere is an isothermal gas sphere embedded in a pressurized medium in hydrostatic equilibrium. A number of isolated globules and cores have been studied in near infrared showing a good fit to the Bonnor-Ebert sphere profiles (Alves et al. 2001, Teixeira et al. 2005, Kandori et al. 2005). Since we do not want to study the formation from molecular cloud to birth of a star, but only the physics after the star is formed and starts ionizing the surrounding medium, we omit the force of gravity in the simulations. In order to have an equilibrium solution, we put the sphere in pressure equilibrium by changing the temperature appropriately. In this way we create a density profile that resembles the Bonnor-Ebert density structure without including gravity.

3.4.2 Initial conditions

We carried out a parameter study to investigate what determines the shape and size of H ɪɪ regions during their dynamical evolution. We also want to establish whether the ionized gas moves inside the H ɪɪ region and is able to set the right conditions for a dust wave.

We keep the type of star fixed with $\mathbb{N}_{Lyc} = 10^{48}$ s^{-1}, without stellar winds, and the box size 26 pc by 19.5 pc. We modify the density profile: we generate four clumps with the modified Bonnor-Ebert sphere with properties listed in Table 3.2. The average density and the mass in the clump spans two orders of magnitude. The ambient pressure has a low

and high value. In Figure 3.2 we illustrate the one-dimensional density and temperature profile of the four clumps.

Additionally to the density, we also change the location of the source with respect to the center of the clump. We consider three cases: the star at the center of the clump, the star offset along the x-axis of 1.3 pc and 4.9 pc. We run a total of twelve two-dimensional simulations by combining the four clumps and the three locations of the ionizing star. We assume that the star is not moving in respect to the ambient medium.

3.5 Results of the simulations

3.5.1 Morphology

We carried out a parameter study to determine the effects of the density of the ambient medium and the location of the star on the resulting H II region size, morphology and characteristics. We plot in Figure 3.3 and 3.4 the results of our twelve simulations at age 1 Myr and 2 Myr respectively. We note that H II regions in the lower density medium reach a larger radii in a shorter time. This is expected: the recombination timescale goes as $1/(\alpha_B n)$, where α_B is the recombination rate, and the expansion depends on the amount of gas that gets ionized and stays as such. In a lower density medium a larger volume of gas is ionized.

The position of the star with respect to the clump determines the shape of the H II region. When the star is at the center of the clump the H II region is perfectly spherical. The Strömgren radius is reached in a recombination timescale, before the gas has time to react. Later, the increase in pressure due to the increase in temperature ($\sim 10^4$ K) drives the shock to larger radii. However, the pressure of the ambient medium stops such a shock and material builds up into a thick shell that radiation cannot penetrate anymore. The result is an inner region of gas highly ionized and of low density at temperature $\sim 10^4$ K surrounded by a almost neutral, denser shell propagating into the medium.

The same physics happens when the star is offset with respect to the clump center, with the difference that there is no more symmetry in the H II region. The result is an elongated H II region towards the low density side, that can eventually evolve into an open H II region. The increasing distance of the star to the center of the clump increases the asymmetry of the morphology of the H II region.

In the offset cases, simulations show Rayleigh-Taylor instabilities in a zone between the ionization front and the dense shell towards the low density medium. When the ionized gas at higher pressure is accelerated towards the medium at lower pressure, the instability sets in and the typical gas mushroom-like features characteristic of the Rayleigh-Taylor instability becomes visible.

Finally we note that the location of the star with respect to the slope of the density of the medium creates differences in the evolution of the H II region. Looking at clump C and D, where the main difference is the slope of the radial decay in density, we see that the asymmetries evolve faster in the less steep case (clump D) creating a more elongated H II region.

Figure 3.3 – Logarithm of the number density (in cm^{-3}) after 1 Myr from the start of the simulations. The location of the ionizing star is marked by the star symbol, while the clump center is marked by a dot. We also mark the ionization front (black line), defined as the location where the ionization fraction has dropped to a value of 0.5. From top to bottom we show clump A, B, C, D respectively. On the columns we plot the three stars offset: centered, offset by 1.3 pc, and offset by 4.9 pc.

3.5.2   Velocity of the ionized gas

Figure 3.5 illustrates the total velocity of the gas for the twelve runs at age 2 Myr. For the low density case (clump A) the swept up shell expands at about 5 $km\,s^{-1}$ into the medium, while the ionized gas inside the H II region has a velocity strongly dependent on the morphology of the region. For the offset cases at low density, most similar to the broken and fully open observed cases, the velocity of the ionized gas reaches value of 20-35 $km\,s^{-1}$. For the higher density clumps, the velocities reached inside the bubbles is
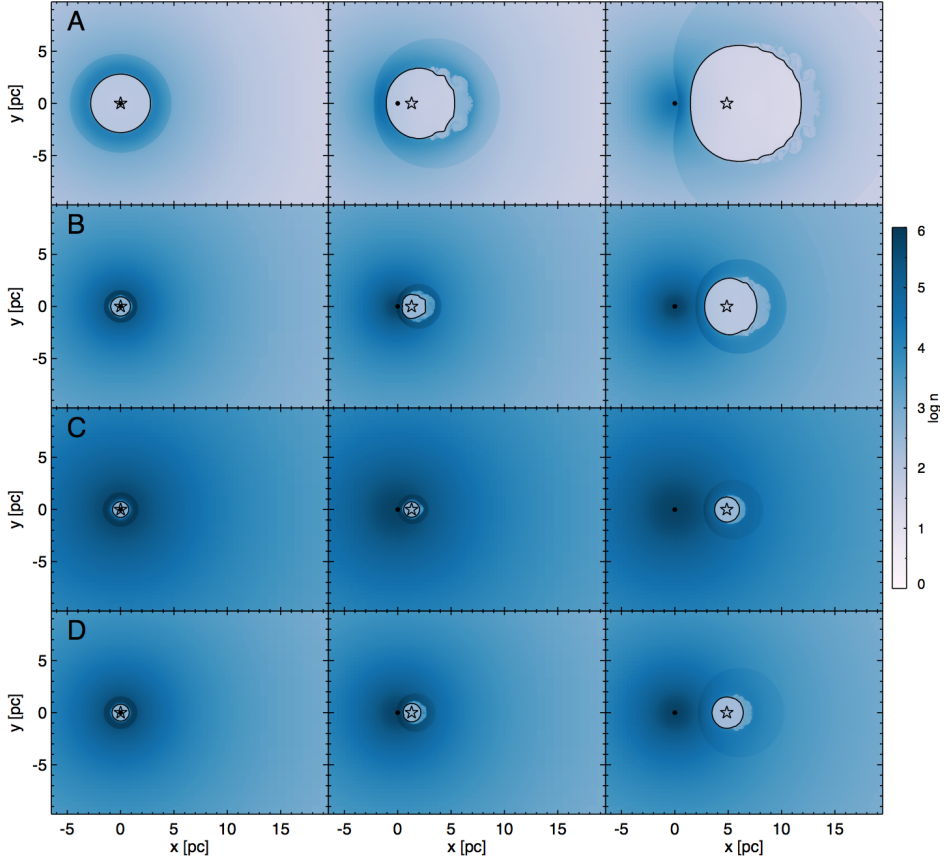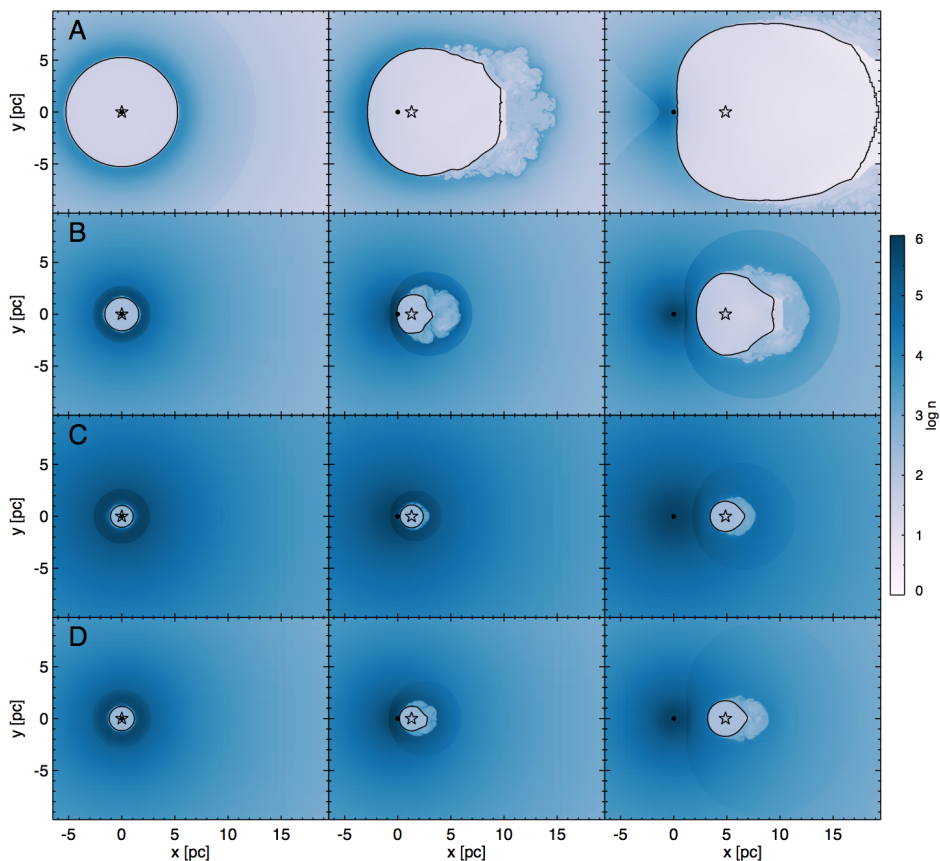
Figure 3.4 – Logarithm of the number density (in cm^{-3}) after 2 Myr from the start of the simulations. The location of the ionizing star is marked by the star symbol, while the clump center is marked by a dot. We also mark the ionization front (black line), defined as the location where the ionization fraction has dropped to a value of 0.5. From top to bottom we show clump A, B, C, D respectively. On the columns we plot the three stars offset: centered, offset by 1.3 pc, and offset by 4.9 pc.

from 5 to 20 km s^{-1}. We note that the ionized gas moves down the density gradient even before the H II region opens up, an in some cases, the H II region is close to spherical, but has already the gas moving towards what will be the opening.

Figure 3.6 shows the ranges of velocities reached along the x-axis passing through the star at different ages. The spherical case shows a very symmetric profile characteristic of a sphere expanding outwards. The neutral shell expands at maximum 5 km s^{-1} in radial direction. When the star is offset from the cloud center, the gas is accelerated up to 20 to 25 km s^{-1} (according to the offset) at the location of the star, creating the perfect
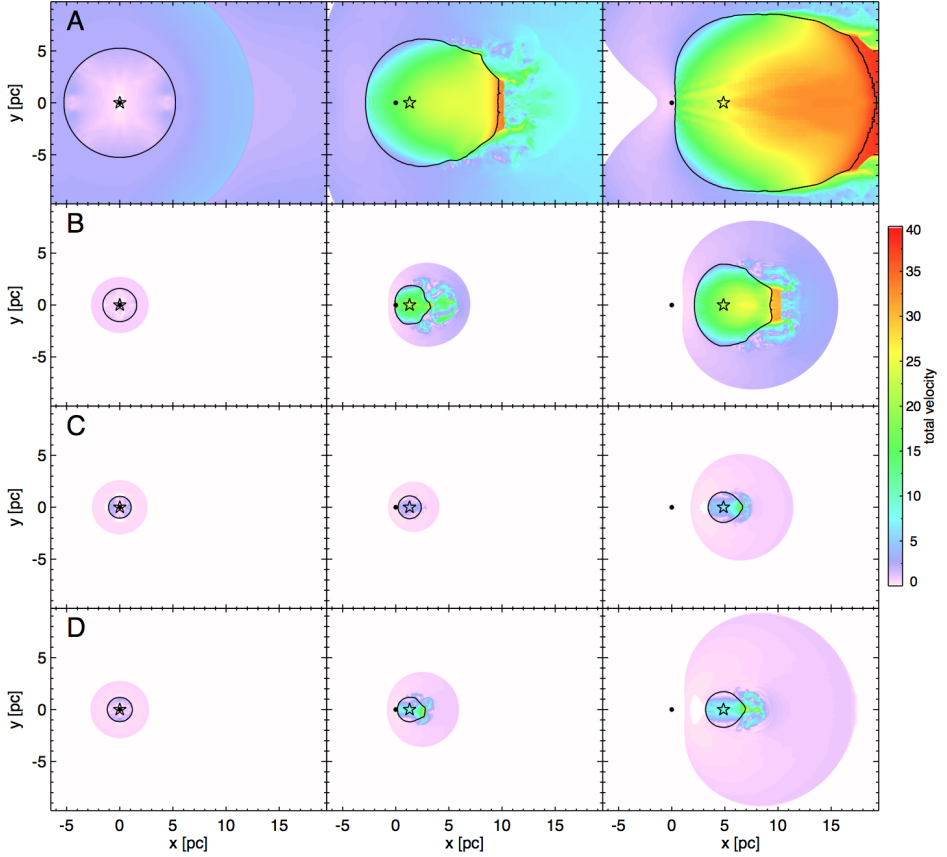
Figure 3.5 – Total velocity (in km s^{-1}) after 2 Myr from the start of the simulations. The location of the ionizing star is marked by the star symbol, while the clump center is marked by a dot. We also mark the ionization front, defined as the location where the ionization fraction has dropped to a value of 0.5. From top to bottom we show clump A, B, C, D respectively. On the columns we plot the three stars offset: centered, offset by 1.3 pc, and offset by 4.9 pc.

conditions for the dust wall to set up.

3.6   Discussion

3.6.1   Comparison with observations

We selected two simulations that are representative of the two classes of bubbles that are observed: closed and broken/open bubbles. We choose clump B with star offset of 1.3 pc
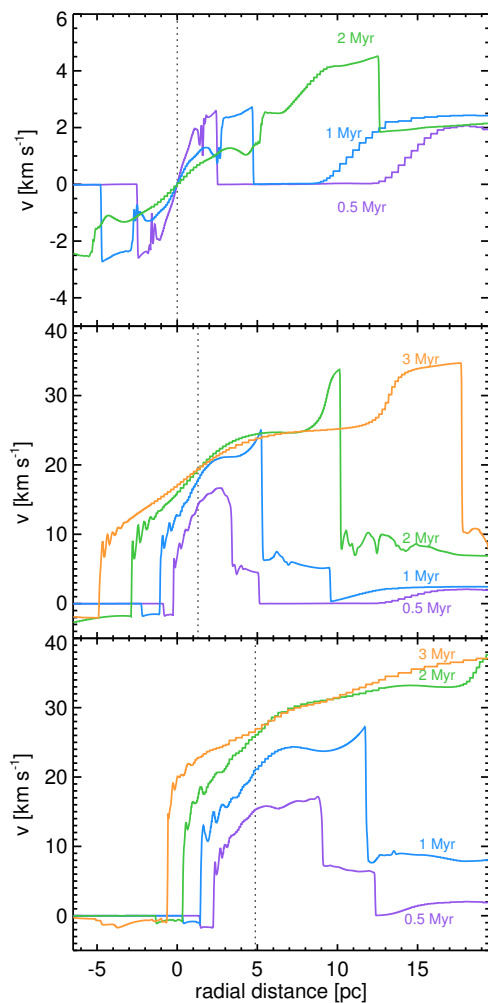
Figure 3.6 – Time evolution of the total velocity of the gas along the x-axis passing through the star for clump A. The ionizing star location is indicated by the dotted line, the clump is at zero coordinate. From top to bottom we show clump three stars offset: centered, offset by 1.3 pc, and offset by 4.9 pc. The velocity of the gas along the cut is shown for times 0.5, 1, 2 and 3 Myr after the start of the simulation. Note the different y-axis range for the top panel.

to represent the closed bubbles and clump A with stellar offset 4.9 pc as an example of the broken bubbles. We run those two cases in three dimensions and produce maps similar to the observables. We create emission maps of the ionized gas to estimate the radio emission. We select gas with a column density from the central star up to 10^{21} cm^{-2} that

(a) Closed bubble: Clump B, offset 1.3 pc,   (b) Broken bubble: Clump A, offset 2.4 pc,
1 Myr   1 Myr
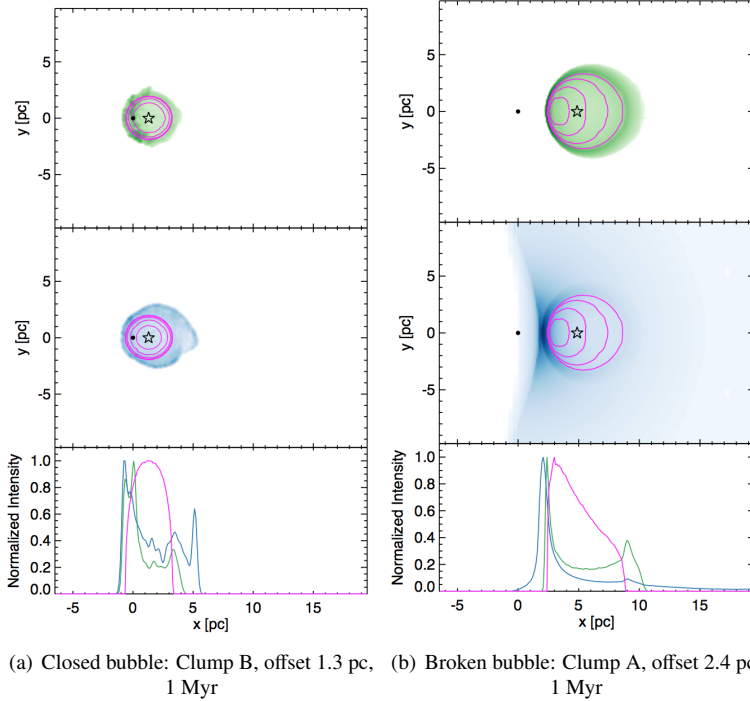
Figure 3.7 – Synthetic emission of the PAH feature (top panel), the cold dust component (middle panel) and ionized gas (contours) for a typical (a) closed bubble and (b) broken bubble. We also show cross-cut through the center of the star of the three components (bottom).

represents the PAH emission, and gas with a column density up to 10^{22} cm^{-2} to represent the PACS observation of the dust. Then, we integrate along a line of site and generate column density maps of the selected region as would be observed. We plot the results in Figure 3.7.

For the closed bubble (Figure 3.7(a)), the radio emission measure is symmetric and peaks at the center of the bubble. Our hydrodynamic simulations with radiative transfer exclude the effects of radiation pressure on the gas or on the dust. Therefore the ionized gas inside the bubble is uniform and the emission measure peaks at the center due to projection effects. The profile follows Draine (2011) dustless case. If we assume the presence of dust and radiation pressure acting on the gas and dust, we would expect the gas and dust to clear out the central part of the H II region and pile up towards the ionization front, as seen in N49 (Figure 3.1(a)) and N90 (Figure 3.1(b)). The PAH feature has its maximum just outside the ionized gas region and marks the location of the ionization front. Further out in radius, there is the location of the cold dust emission, tracing the dense material of the swept up shell.

In the case of broken/open bubbles, the ionized gas piles up towards the highest den-

sity of the ISM, as seen in observed bubbles (Figures 3.1). Cold dust, PAH feature, and ionized gas emission have distinctive peaks of emission, respectively from the high density part to the low density part. In the case of RCW120 (Figure 3.1(c)), the emission of each component behave as expected from theory. The sequence from partially broken bubbles to open is a result of the combined effects of density and time. If the density gradient is quite steep or the average density is not very high, the H II region expands to larger radii and breaks up quite fast. However, at early stages the H II region has a spherical shape.

3.6.2   Location of the dust wave

Ochsendorf et al., 2013a (submitted) developed a model to study the interaction of a dusty evaporative flow with the radiation pressure of the star. In this work, the equation of motion of the dust and the gas are calculated by solving a coupled set of differential equations, which includes the radiation pressure force and momentum transfer through the drag force.

When dust and gas decouple, dust piles up in front of the star, and a dust wave forms. The conditions necessary for such dust wave to generate can be quantified by the dimensionless coupling strength parameter, $C = 1 - v_g/v_{g,0}$, where $v_{g,0}$ is the initial velocity of the gas (i.e., the velocity of the photo-evaporation flow) and v_g is the velocity of the gas at the location where the dust is stopped. C is a measure of the efficiency of momentum transfer between gas and dust through the drag force and is regulated by the flow velocity and the density of the gas. For $C = 1$, gas and dust are tightly coupled in a photo-evaporation flow and a bow wave forms (Ochsendorf et al. 2013b, submitted).

We plot in Figure 3.8(a) the coupling strength C for a grid of models that have the same ionizing source (10^{48} s^{-1}) and varying density and velocity of the flow. We show also the time dependent results for the simulated H II regions. As Figure 3.8(a) displays, the coupling between gas and dust is least effective in high velocity photo-evaporation flow. Therefore, dust waves are expected to form in particular in Model A and B, which reaches high velocities near the star soon after ionization of the cloud material: indeed, these models also reproduce the observations best.

Similarly, Figure 3.8(b) shows the coupling strength C for a grid of models that have the same ionizing source (10^{48} s^{-1}), but for varying density and H II region radii. We can compare Model A and B – that have the right conditions for a dust wave to form – directly with observations. We note that there is overlap between observed H II regions and models. This indicates that broken/open bubbles have photo-evaporative flows above 15-20 km s^{-1}. The source N69 is the completely open source for which it is difficult to define both radius and density; uncertainties on the observations may cause the offset found in Figure 3.8(b). All models have a similar dependence between ionized gas density and radius of the H II region, with the exception of Model A2. The general trend is expected, as the H II region radius increases with time, the gas inside the bubble is diluted in a progressively larger volume, causing the density to decrease. Instead, Model A2 expansion is stopped by the presence of the clump, while the gas is flowing out of the region at considerable speed.
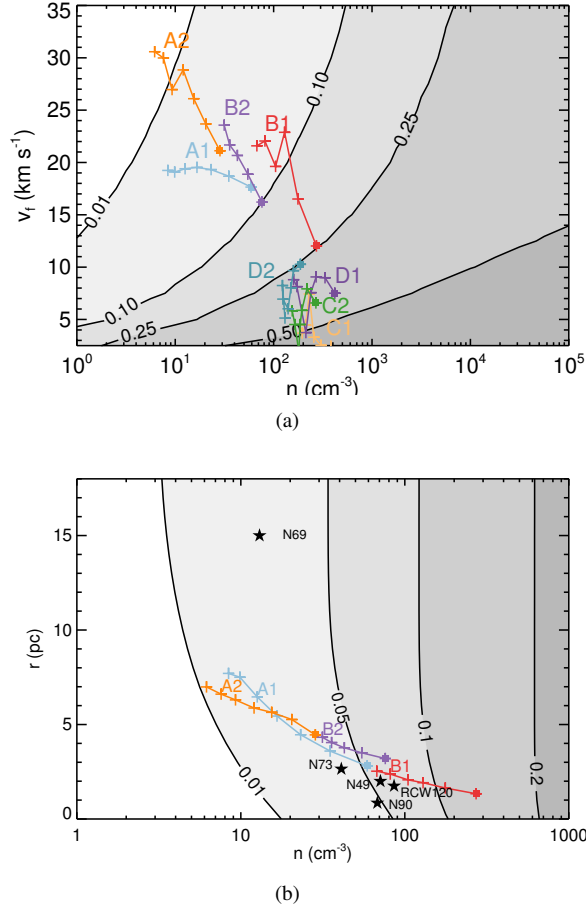
Figure 3.8 – Gray scale with marked contours of the coupling strength, C, for a grid of models with fixed ionizing source luminosities $\mathbb{N}_{Lyc} = 10^{48}$ s^{-1} and varying (a) velocity of the flow, v_f, and ambient densities, n; (b) radius of the H II region, r, and ambient densities, n. Time dependent tracks from the H II region simulations are over plotted. Cross symbols mark time intervals of 0.5 Myr starting from the filled square symbols. The letter correspond to the clump, as in Table 3.2, and the numbers refer to the offset of the source in respect to the clump center, with '1' being 1.3 pc offset, and '2' 4.9 pc offset. The five selected typical H II regions are shown in (b) with star symbols. Low coupling strength will lead to dust wave, while high coupling strength results in bow wave.

In conclusion, models seem to indicate that champagne flow H II regions that can produce gas flows at the source location above 15-20 km s^{-1} are likely to show a dust wall. The morphology of such H II regions can vary from almost spherical shapes to broken and open bubbles.

3.6.3   Champagne flow H II regions

Our assumption of small influence of the stellar winds on the H II region evolution is based on recent observation that revealed weak-wind strength for stars with $\log(L/ \, L_\odot) \leq 5.2$ (Martins et al. 2005, Marcolino et al. 2009). Beaumont & Williams (2010) studied an unbiased sample of H II regions and most of their ionizing stars have luminosity $\log(L/ \, L_\odot) \leq 5.2$, even after correction of the distance (Anderson & Bania 2009), indicating that a large population of H II regions might simply be explained without the effects of stellar winds. We argue that the arc-structures seen in infrared emission inside H II regions can be explained as dust waves induced by photo-evaporating flows inside H II bubbles. We revisit the champagne flow model, as first suggested by Mac Low et al. (1991), and calculate the flow velocity of the ionized gas. Dust waves require a gas velocity $> 10 \; \mathrm{km\,s^{-1}}$ near the star. By placing the ionizing star offset from the center of a Bonnor-Ebert sphere, the ionized gas flows in a champagne flow kind of fashion towards the low density part, or tail of the region. We show that the gas velocities are enough to explain the creation of dust waves. This mechanism provides a natural explanation for the presence and morphology of dust emission seen in the interior of H II bubbles (Deharveng et al. 2010, Anderson et al. 2012) and the morphology of the H II region itself.

3.6.4   Kinetic energy

In some models, the swept-up shell of the H II region breaks open and the ionized gas is injected directly into the surrounding ISM. The flow can reach velocity up to $40 \; \mathrm{km \; s^{-1}}$, with a total of kinetic energy released into the ISM up to 10^{49} erg. A typical supernova explosion has an energy of about 10^{51} erg, 10% of which gets transformed into kinetic energy of interstellar gas (Veilleux et al. 2005). Therefore the energy released by single H II regions is one order of magnitude smaller, considering that the lifetime of late type O stars is about 6-7 Myr. Nevertheless, their contribution to the kinetic energy in the ISM might be relevant particularly when considering scale sizes of $\sim$ 1-3 pc in regions of massive star formation.

3.6.5   Triggered star formation

The theory of triggered star formation was first introduced by Elmegreen & Lada (1977). The ionization shock front of a massive star or group of stars provides the external pressure to compress a nearby molecular cloud and start its collapse. However, recent observations of single H II regions showed that triggered star formation can happen also at smaller scales. The swept-up shell produced by an ionizing star can be gravitationally unstable and fragment into small clumps that will generate low-mass stars. The ionizing radiation can induce condensation of preexisting overdensities due to turbulence and produce fingers and pillars and eventually a star. Examples of triggered star formation by the H II region bubble have been shown by Deharveng et al. (2009), Deharveng et al. (2010) and Zavagno et al. (2007)

The simulations we carried out in this work show that all the conditions for triggered star formation are met. During the evolution of H II regions, the swept-up gas becomes quite dense and contains up to 10^4 M$_\odot$ in gas. The simulations with the ionizing star offset from the molecular cloud show a denser swept-up shell towards the highest density of the medium. Studied of RCW 120 showed that most of the condensation of material and possible formation of new stars is on the densest shell, opposite to the opening. Under the conditions of the swept-up shell, the Jeans length is about 0.5 pc that is smaller than the shell thickness, making this mechanism possible within the shell. The Jeans mass is ~ 15 M$_\odot$. We have showed that fragmentation might be possible, however detailed studies are needed to determine how efficient such mechanisms would be in generating new star.

3.7   Conclusions

We analyze a class of H II regions that show dust emission at 24 μm in their interior. We identify five typical H II regions with luminosity log(L/ L$_\odot$) < 5.2 to ensure that their stellar winds are weak. Each H II region represents a morphological class: closed, broken and open shells. We use *Spitzer*/IRAC 8 μm from the Glimpse survey to traces PAH emission coming from the PDR located at the inner boundary of the swept up shell; *Spitzer*/MIPS 24 μm from the MIPSGAL survey, which traces warm dust (50-150 K) emission mainly coming from both the swept-up shell and the interior of the bubble; *Herschel*/SPIRE 250 μm from the Hi-Gal survey to trace cool (10-40 K) dust emission from dense condensation; and *VLA* 20 cm images from the MAGPIS survey to trace free-free continuum emission from ionized gas.

We carried out hydrodynamical simulations using FLASH HC code of a class of champagne flow H II regions to explore the role of the environment and age on the morphology of the bubble. We set up an ionizing star at the center and offset from the center of four typical clumps. Each clump has a Bonnor-Ebert density profile modified to be in pressure equilibrium.

We find that all the morphological classes of observed H II regions can be explained with a champagne flow model. Closed bubbles are either young or evolving in a symmetric environment. The ionizing star of broken and open bubbles is in a non-uniform, and asymmetric medium.

The velocity of the gas inside the bubble reaches values up to 30 km s^{-1} at the star location that allows a dust wave to form. We find that a classical champagne flow model can explain both the presence of the dust inside the bubble. As suggested by (Ochsendorf et al., 2013a submitted), the cometary shape of the dust emission is the result of the interaction between radiation pressure from the star with the dust contained in the flow of ionized gas.

We limited this study to the case when stellar winds are negligible. Clearly, more massive stars have strong stellar winds and those change the structure and evolution of H II regions. However, dust emission has been found inside bubbles that have strong stellar winds. We leave to a future work the analysis of this class of H II regions.

IV

A study of H II regions in NGC 6822 and the distribution of star-forming galaxies in emission line diagnostic diagrams

Derivation of physical parameters of H II regions, such as age, radius and density of the ambient medium, is important in understanding the interaction of massive stars with their surroundings, the mechanisms driving the expansion of the ionized gas, and the link between star forming galaxies and single H II regions. We seek to obtain well constrained physical parameters of H II regions in the nearby universe and use such information to understand the star forming sequence of Sloan Digital Sky Survey (SDSS) galaxies in optical line diagnostic diagrams and their relation with single H II regions. We select two well-studied H II regions in the nearby galaxy NGC 6822: Hubble V and Hubble X. We collect archive data: optical emission line images, optical photometry, and infrared (IR) data. We make use of unidimensional analytical models to constrain the density of the medium around each H II region. We carry out photoionization models of H II regions powered by stellar winds and radiation pressure. We find that the ambient densities derived from analytical expansion models are generally higher than observations suggest. We are able to confirm the young age of the cluster and the ionization state of the region. We compare with a selection of SDSS galaxies and find that their emission characteristics are consistent with most of their light coming from the few brightest H II regions rather than the most dim ones.The location of Hubble V and Hubble X on the BPT diagram confirms the evolutionary tracks derived from the photoionization models. The two H II regions represent the low end of the distribution of star forming galaxies. Analysis of our models shows that the most massive stellar cluster in blue star forming galaxies tend to be younger than our H II regions.

Silvia Verdolini, Lynn R. Carlson, Sherry C. C. Yeh, Maud Galametz, Vianney Lebouteiller,
Jarle Brinchmann, Frédéric Galliano, Alexander G. G. M. Tielens
to be submitted

4.1 Introduction

Detailed studies of H II regions in the local universe are important in understanding star formation processes, the evolution of high mass stars, and properties of the interstellar medium (ISM) in which they expand. When a high mass star emits radiation, the gas around it becomes ionized. The ionized gas is heated by photoelectrons and and cooled through line emission processes, primarily, optical forbidden lines and IR fine structure lines from trace species. For a constant density nebula, the resultant H II region's size (the Strömgren radius) can be derived from the global ionization balance which equates the total photon luminosity from the star with the total recombination rate integrated over the nebula.

The Baldwin et al. (1981) diagram (hereafter the BPT diagram) is a commonly used tool to study extragalactic H II regions and their host galaxies. The most used combination is [O III] $\lambda5007$/Hβ versus [N II] $\lambda6584$/Hα that, in the galactic context, allows a clear distinction between star-forming and AGN dominated galaxies. In this plot, single H II regions cover a narrow sequence that overlaps with the star-forming sequence of the Sloan Digital Sky Survey (SDSS) galaxies (Brinchmann et al. 2004). The location on this sequence is controlled by physical properties of the H II region, such as metallicity, density of the ISM, ionization parameter, and age. Understanding how the star forming sequence is connected to single H II regions on the BPT diagram can be helpful to assess physical properties of unresolved H II regions in extragalactic galaxies. Models of the BPT diagram, or in general any line emission, are produced using photoionization model codes such as Cloudy (Ferland et al. 2013) or MAPPINGS III (Sutherland & Dopita 1993, Dopita et al. 2000). It is possible to create a set of predicted H II regions' line emission that can be compared to the observed BPT diagram for a set luminosity of the central star or star cluster, density of the ambient medium, and age. Such modeling is important in understanding H II regions' structures and in constraining their physical properties. By matching observations and a grid of models on the BPT diagram, it is possible to derive an approximate cluster age and ionization state of the region, even if the region is unresolved.

Observationally, H II regions have complex structures, and it is sometimes difficult to disentangle physical parameters making it problematic to compare with theoretical models. Recently, variations of the principal emission line ratios and derived physical values within H II regions have been found by studying giant H II regions and large star-forming regions in nearby galaxies using integral field spectroscopy. Such studies include H II regions in the outer disk of NGC 6946 at a distance of 5.9 Mpc (García-Benito et al. 2010), and N588 (Monreal-Ibero et al. 2011), N595 (Relaño et al. 2010), and IC132 and the central region (López-Hernández et al. 2013) of M33 at a distance of 840 kpc. Many studies of closer H II regions, such as 30 Doradus in the Large Magellanic Cloud (50 kpc) (Lopez et al. 2011, Pellegrini et al. 2011), have shown the level of complexity that can be reached in one single star forming region including multiple star formation events at different ages and locations, triggered star formation, and colliding stellar winds.

The aim of this study is to investigate the properties of H II region and compare observations with theory. We select two well-studied H II regions that have available multi-wavelength observations of gas and dust. They are two bright, single, resolved extragalac-

tic H II regions Hubble V and Hubble X in the Local Group dwarf irregular NGC 6822. In term of size, stellar cluster, and density, we expect that those two H II regions are much better analogues of H II regions dominating the emission of SDSS galaxies than either galactic compact H II regions such as Orion or M17 or the intense starburst associated with 30 Dor in the Large Magellanic Cloud. Indeed, the distance of NGC 6822 (490 kpc; Mateo 1998), provides good spatial resolution compared to other extragalactic sources. It is the closest active star forming galaxy after the Magellanic System (Cannon et al. 2012) and the closest with no massive neighbor. It is gas-rich and has a metallicity of Z∼ 0.4 $Z_\odot$. A large neutral gas disk has been reported by de Blok & Walter (2000), and it shows a complicated structure of shells and holes indicating a past interaction event (Cannon et al. 2012). Hubble V and Hubble X are two of its most prominent star forming regions and have similar ionizing clusters and ages but different morphologies. Hubble V is more compact, while Hubble X displays an almost spherical shell, typical of idealized H II regions. O'Dell et al. (1999) studied the ionization properties of the two regions from optical emission-line images. Bianchi et al. (2001) used Hubble Space Telescope (HST) imaging to derive resolved stellar photometry and study the high mass stars contained in the two clusters, showing that both H II regions contain very young stellar populations and several massive stars.

The structure of the paper is as follows. In Section 2, we describe the data used for the analysis. In Section 3, we compare theoretical models of the expansion of H II regions with the observations. In Section 4 we present our photoionization models. We discuss our findings in Section 5, and we finish with conclusions in Section 6.

4.2 Data set

4.2.1 Optical emission line images

Optical emission line images come from the Wide Field Planetary Camera 2 (WFC2) from the HST and are taken from the Hubble Legacy Archive (HLA). Bands used are F487N (Hβ), F502N [O III], F656N (Hα), and F658N [N II]. These Level 2 combined images were fully reduced by the HLA team using the IRAF[1] package MultiDrizzle and are provided by HLA in units of electrons/second. We convert to W m^{-2} by multiplying by the PHOTFLAM keyword provided in the fits image header and by the central wavelength. Original images were taken as part of Program GTO 6159 and presented by O'Dell et al. (1999).

We use high resolution optical imaging to examine the morphology and determine the radius of the H II regions. Hubble V consists of two separate structures: a very bright core in all emission lines powered by a compact stellar cluster consisting of a few OB stars as identified via photometry (see Section 4.2.2) and an extended structure towards the South-East powered by less massive B stars. We focus our study only on the bright core which we refer to as Hubble V for the rest of the paper. We adopt a radius for Hubble V of

---

[1] IRAF is distributed by the National Optical Observatories, which are operated by AURA Inc., under cooperative agreement with the National Science Foundation.
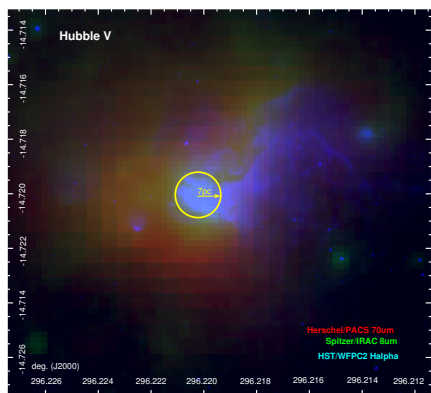
Figure 4.1 – Composite image of Hubble V: HST F656N (Hα) tracing hot ionized gas (blue); *Spitzer*/IRAC 8 μm showing PAH emission and tracing the photodissociation region (green) and *Herschel*/PACS 70 μm tracing denser gas of the molecular cloud (red). The circle indicates the selected area for the analysis done in the rest of this paper. Intensities are shown on a logarithmic scale.
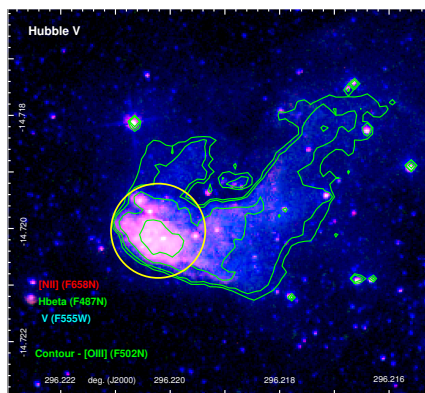
Figure 4.2 – Zoomed-in composite image of Hubble V: HST F555W-V band (blue) showing the stars of the cluster. HST F487N Hβ (green); HST F658N [N II] (red); and contours for HST F502N [O III]. The circle indicates the selected area for the analysis done in the rest of this paper. Intensities are shown on a logarithmic scale.
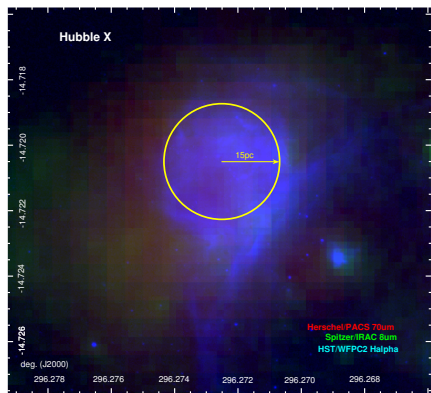
Figure 4.3 – Composite image of Hubble X: HST F656N (Hα) tracing hot ionized gas (blue); *Spitzer*/IRAC 8 μm showing PAH emission and tracing the photodissociation region (green) and *Herschel*/PACS 70 μm tracing denser gas of the molecular cloud (red). The circle indicates the selected area for the analysis done in the rest of this paper. Intensities are shown on a logarithmic scale.
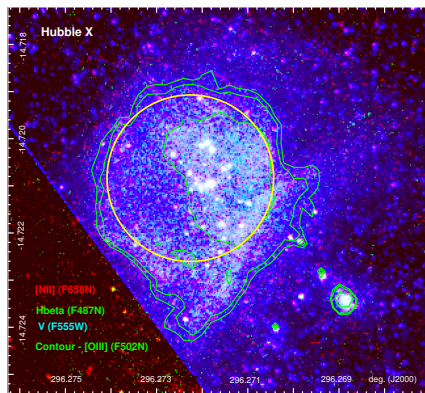
Figure 4.4 – Zoomed-in composite image of Hubble X: HST F555W-V band (blue) showing the stars of the cluster. HST F487N Hβ (green); HST F658N [N II] (red); and contours for HST F502N [O III]. The circle indicates the selected area for the analysis done in the rest of this paper. Intensities are shown on a logarithmic scale.

7 pc. Figure 4.1 shows Hα emission together with *Spitzer* and *Herschel* (Section 4.2.3). Hα traces the wall inside the H II region, surrounded by a photodissociation region and the parent molecular cloud, traced by *Spitzer* and *Herschel* respectively. In Figure 4.2 we illustrate the other strong line emission, together with the V band. All the brightest emission is located within the 7 pc radius.

Figure 4.3 and 4.4 show that Hubble X has a more spherical shape, close to the ideal H II region, and it is more extended. It has a radius of $\sim$ 15 pc centered on the stellar cluster visible in the V band. The Hα image shows that at the South-East of the main bubble there is an arch-like diffuse emission. We believe that this structure is the remains of an old H II region, confirmed by the considerably older age of the stellar content of this region. Towards the South-East of the image there is another isolated clump, bright in all line emission, a separate small H II region with its own population of massive stars. We will refer to Hubble X as only the region within the marked radius.

4.2.2 Optical photometry

Bianchi et al. (2001) constructed the H-R diagram for star-forming regions in NGC 6822, including Hubble V and X, using HST UBV photometry. They superimpose isochrones from the model atmospheres of Bertelli et al. (1994) and derive ages of the stellar population < 4 Myr for both star forming regions. Although there are a few evolved stars in their H-R diagrams, they are simply looking over a larger field of view; those sources lie outside of the physical structures we examine here.

We use photometry provided in Massey et al. (2007) to characterize the stellar population. Observations were conducted with the Cerro Tololo Inter-American Observatory (CTIO) Blanco 4 m telescope to obtain images in *UBVRI* with a pixel scale of 0.''27 and point spread functions between 1'' and 1.''5. They used images from the CTIO 0.9 m and the Lowell 1.1 m for additional (color) calibration. Internal photometric errors are estimated to be $\lesssim$ 5% for massive stars (M$\gtrsim$ 20 M$_\odot$). Massey et al. (2007) found that their photometry matches that of Bianchi et al. (2001) from HST. The Massey et al. (2007) photometry, however, includes more photometric bands, and provides better detections at the brightest end than either Bianchi et al. (2001) (where HST saturates) or de Blok & Walter (2006).

To obtain absolute magnitudes, we subtract a distance modulus of 23.45 and apply a reddening correction as derived from Efremova et al. (2011). They found a total E(B-V) = 0.41 ± 0.15 for Hubble V and E(B-V) = 0.36 ± 0.16 for Hubble X. This includes a Milky Way foreground component of E(B-V) = 0.22 with R$_V$ = 3.1 plus an internal redding component with an extinction curve similar to that of 30 Doradus in the Large Magellanic Cloud with R$_V$ $\sim$ 2.68 (Misselt et al. 1999), resulting in A$_V$ $\sim$ 1.19 and A$_V$ $\sim$ 1.05 for Hubble V and X, respectively.

For the most luminous stars, we interpolate from main sequence isochrones of $\sim$ 6 Myr (Girardi et al. 2002) with metallicity $\sim$ 0.4 Z$_\odot$ to obtain bolometric magnitudes. These stars are brighter than M$_V$ $\sim$ −4.3, representing the OB population that will dominate ionization and any stellar wind input in the region (Cox 2000). For main sequence stars and the measured magnitude M$_V$, M$_{bol}$ is interpolated from the isochrones and used

to calculate the bolometric luminosity:

$$L_{bol} = 10^{(4.75 - M_{bol})/2.5} \, L_\odot \,. \tag{4.1}$$

From bolometric luminosities, we can then approximate how many ionizing photons are coming from the stars.

$$\mathbb{N}_{Lyc} \simeq 7.2 \times 10^{43} L_{bol} - 4.4 \times 10^{48} \; s^{-1} \tag{4.2}$$

for O to early B-type stars, where $\mathbb{N}_{Lyc}$ is the number of ionizing photons, and L_{bol} is expressed in units of $L_\odot$ (Vacca et al. 1996).

Some of the bright sources, both in the Massey et al. (2007) and Bianchi et al. (2001) photometry lists, have inconsistent colors in different bands. These are in the crowded center of the clusters within the H II regions, and we attribute the unlikely photometry to crowding, high-background, source-blending, and differential reddening. The Massey et al. (2007) list includes twelve bright sources in the core of Hubble V, of which seven have normal main-sequence colors, three are redder than expected, and two are very blue even before dereddening. Likewise, of eight bright sources in the core of Hubble X, four are unphysically blue. For the seven OB sources with main-sequence colors Hubble V, the total $\mathbb{N}_{Lyc} \sim 1.7 \times 10^{50}$ s^{-1}; for the four in Hubble X $\mathbb{N}_{Lyc} \sim 10^{50}$ s^{-1}.

We can also derive the number of ionizing photons from Hβ. We derive $\sim 30 \times 10^{49}$ s^{-1} for Hubble V and $\sim 25 \times 10^{49}$ s^{-1} for Hubble X, corresponding to 6 and 5 O4 stars, respectively. When compares to the number of ionizing photons derived from photometry, it indicates that the objects with inconsistent colors account for approximately half of the total ionizing radiation.

4.2.3 Mapping dust and gas

We use broad band IR data from the Spitzer Space Telescope (*Spitzer*) (Werner et al. 2004) Infrared Array Camera (IRAC; Fazio et al. 2004) and Multiwavelength Imaging Photometer for *Spitzer* (MIPS; Rieke et al. 2004) and from the Photodetector Array Camera and Spectrometer (PACS) and the Spectral and Photometric Imaging Receiver (SPIRE) aboard the *Herschel* Space Observatory (*Herschel*; Pilbratt et al. 2010). IRAC (3.6-24 μm) and MIPS (24-70 μm) images were taken as part of "The Spitzer Infrared Nearby Galaxies Survey" (SINGS; Kennicutt et al. 2003) and obtained through the NASA/IPAC Infrared Science Archive (IRSA[2]). Reduction of MIPS images is described by Bendo et al. (2012). Herschel FIR and submm maps were obtained and reduced as part of the Dwarf Galaxies Survey (Madden et al. 2013) with data reduction described by Rémy-Ruyer et al. (2013). These broad band maps are combined to produce a map of the dust content of the galaxy.

A background subtraction is applied to *Spitzer*/IRAC, *Spitzer*/MIPS and *Herschel*/PACS maps. To do so, a median value is estimated from the distribution of background pixels fitted by a Gaussian and subtracted from the maps. Given the low Galactic latitude

---

[2] http://irsa.ipac.caltech.edu

of NGC 6822, our SPIRE maps are strongly affected by non homogeneous emission coming from Galactic cirrus (Galametz et al. 2010). After masking the emission associated with the galaxy (pixels above 1σ detection in the three SPIRE bands), the cirrus emission is modeled in each map using a Levenberg-Marquardt least-squares 2-D fit with a 3rd order polynomial (we use the function *mpfit2dfun.pro* of the IDL software) and removed from the maps. *Spitzer* and *Herschel* maps (from 3.6 μm to 350 μm) are then convolved to the resolution of SPIRE 500 μm (namely 36″, ∼ 85.8 pc) using the convolution kernels of Aniano et al. (2011). The phenomenological SED fitting procedure of Galliano et al. (2011) is finally applied to the 3.6 to 500 μm dataset on a local basis in order to derive a dust mass map of NGC 6822. In this model, the distribution of starlight intensities per unit dust mass is approximated by a simple power law (Dale et al. 2001). The dust size distribution and composition is considered to be uniform across the galaxy. The old stellar population and the dust grains (composed of Polycyclic Aromatic Hydrocarbons, carbon grains, and silicates) are the sources of the IR-to-submm emission. Amorphous carbon grains are chosen to model the carbon dust. Using standard graphitic grains instead would yield higher dust masses, as shown in Galliano et al. (2011). The stellar contribution to the mid-IR is also modeled using a spectral library synthesized using the stellar evolution code PEGASE (Fioc & Rocca-Volmerange 1997). This SED modeling procedure, from background subtraction and convolution steps to the resolved fitting technique, is further detailed in Galametz et al. (2013) where they model the star-forming region N 159 in the LMC.

To assess the neutral gas content, the gas into which each H II region is expanding, we use an H I moment map of NGC 6822 provided by de Blok & Walter (2000). The beam sizes 42″ × 12″, oriented with the long axis approximately north-south. The native map is in units of Janskys per beam. We first convert to a map of integrated intensity (W_{HI}) in units of K km s^{-1}, multiplying pixel values by 1190.5 K (Cannon et al. 2006) and 1.6 km s^{-1} to account for channel separation (zero-spacing correction; de Blok & Walter 2006). We then covert to number column density using the relation N_H(H cm^{-2}) = 1.82 × 10^{18} W_{HI} K km s^{-1} (Bernard et al. 2008) and to mass column density multiplying by the atomic mass of hydrogen. We find the total mass of H I in circular apertures around each our two regions and convert to density by dividing by the volume of a sphere. The low resolution of the map and likely clumpiness of the gas means that the resulting estimate, approximately the same for both regions, $n_{HI} > 20$ cm^{-3}, must be taken as a lower limit. For a detailed discussion of the ambient medium density see Section 4.5.2.

4.2.4 Ionized gas density

We use [S III] maps in 18 and 33 μm to determine the density of the ionized gas. These two ionized gas cooling lines are dipole forbidden and have approximately the same excitation energy, such that the ratio of the lines is relatively insensitive to temperature for $T_e \sim 10^4$ K. The critical densities, at which collisional de-excitation with electrons becomes important, are different. This line ratio is sensitive in the range $n_e \sim 10^2$-10^4 cm^{-3}, appropriate for the center of H II regions.

We use observations of these two lines from *Spitzer*'s Infrared Spectrograph (IRS
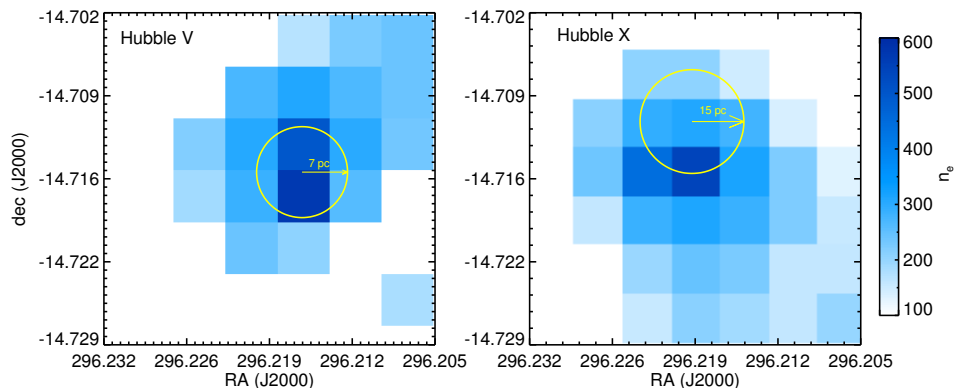
Figure 4.5 – Electron densities for Hubble V (left) and Hubble X (right) derived from [S III] maps in 18 and 33 μm. The circles indicate the same area as in Figure 4.1 and 4.3.

Houck et al. 2004). Observations were performed on September 25th, 2010 (AORkey 9478400), mapping a section of NGC 6822 with the *long-low* module (14-38 μm, spectral resolution $\lambda/\Delta\lambda \approx 57$-126). The bad pixels in the exposures were first cleaned using the IRSCLEAN[3] algorithm. The images were then imported into the spectral mapping software CUBISM (Smith et al. 2007) and further bad pixel cleaning was performed by using the backtracking tool. Finally, we extracted the map of the spectral lines [S III] 18.7, 33.5 μm using CUBISM. Since these lines are isolated and the spectral continuum is fairly simple, we considered a flat continuum for CUBISM to compute the continuum-subtracted line intensity at each position in the map. The spatial resolution of these maps is difficult to know precisely because of the projection of the dispersion axis in the slit, but it should be close to $\sim$ 4$''$ and $\sim$ 7$''$ at 18.7 μm and 33.5 μm respectively. We convolve both images to matching resolutions of $\sim$ 7$\farcs$5 and regrid to matching pixels of 6$''$ $\times$ 6$''$ from unaligned native 5$''$ $\times$ 5$''$ pixels. We take the ratio of 18/33 μm in each pixel and convert to number density, appropriate for an H II region, using a conversion as derived in Dudik et al. (2007). Derived density maps are shown in Fig. 4.5. The average ionized gas density in both regions in the center of the region is $n_e \sim 450$ cm^{-3} for Hubble V and 300 cm^{-3} for Hubble X.

4.3   H II region expansion

The expansion of an H II region has been studied by many authors: Spitzer (1978) studied the expansion due to the effects of overpressure caused by the ionization and heating of the H II region; Castor et al. (1975) considered the mechanical energy of the stellar winds as a main driving mechanism; and Krumholz & Matzner (2009) took into account the

---

[3] http://irsa.ipac.caltech.edu/data/SPITZER/docs/dataanalysistools/tools/irsclean

4.3 HII region expansion

Table 4.1 – Properties of Hubble V and Hubble X

	Hubble V	Hubble V
L_{bol} [10^5 L$_\odot$]	48	31
$\mathbb{N}_{Lyc}$ [10^{49} s^{-1}]	30	25
Age [Myr]	< 4	< 4
Radius [pc]	7	15
n_e [cm^{-3}]	450	300
n [cm^{-3}]	61	52
q_{obs} [cm s^{-1}]	1.1×10^8	3.1×10^7
q_{mod} [cm s^{-1}]	1-4 $\times 10^7$	1-4 $\times 10^7$
M_{HII} [M$_\odot$]	2.1×10^3	2.7×10^3
M_{dust} [M$_\odot$]	9×10^2	1.1×10^3
M_{tot} [M$_\odot$]	6.2×10^5	7.7×10^5
$12 + log$(O/H)	8.37 ± 0.09	8.19 ± 0.16

pressure of the radiation on the gas. Independent of the driving mechanisms, analytical models can be used to constrain physical properties of H II region. At a given density of the surrounding medium, each model predicts the radius of the H II region, i.e. the distance of the ionization front from the star, as a function of time. Given two of the three parameters (density, radius, and age), theory allows us to derive the third unknown. We describe hereafter three analytical models and their application to the case of Hubble V and X.

4.3.1 Analytical models

In the simplest scenario of evolution of the ionization front in a uniform gas, the equilibrium solution (where recombination and ionization of hydrogen balance) is known as the Strömgren sphere. The inside of such an H II region has an inner temperature and pressure higher than the surrounding gas, due to ionization, causing a shock to propagate through the medium that sweeps up material into a dense, neutral shell. As the H II region expands, the density inside the H II region slowly drops, requiring fewer photons to keep the gas ionized. The extra photons lead to an increase in the ionized gas mass, following the Spitzer (1978) analytic solution.

However, there are some complications to this picture. High mass stars have stellar winds, and their importance for the expansion of an H II region has been studied by Castor et al. (1975) and Weaver et al. (1977). The wind expands driving a strong shock into the ambient ISM, sweeping it up into a dense neutral shell. The shocked gas is slowed down by the presence of an ambient medium and the "new" stellar wind material now has a
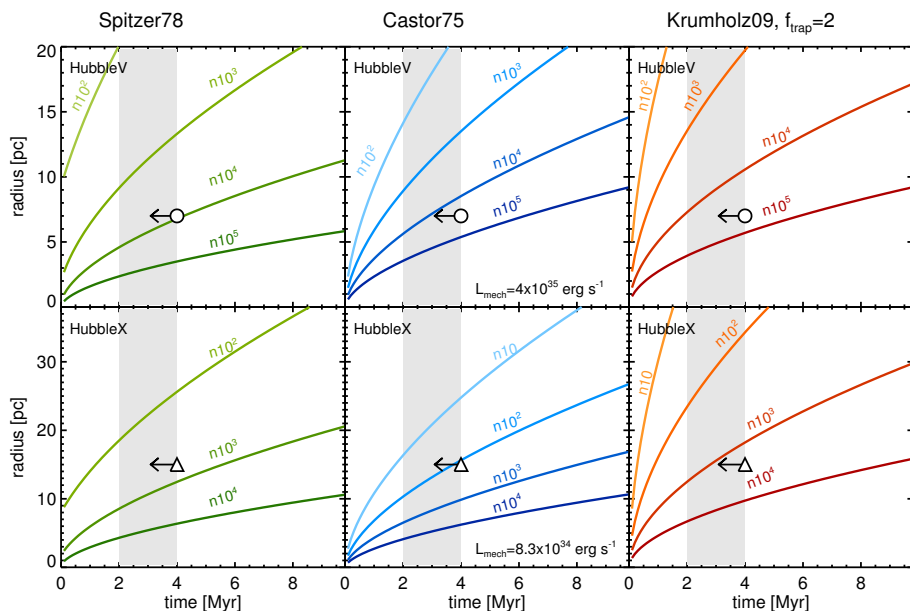
Figure 4.6 – Analytic expansion of H II region radius vs. time for parameters suitable for Hubble V (top row, open circle) and Hubble X (bottom row, open triangle). We compare predictions of three theories: pressure-driven H II regions (Spitzer 1978, left column), wind-driven bubbles (Castor et al. 1975, center column), and radiation pressure-driven shells (Krumholz & Matzner 2009, right column). For each case we show lines calculated with number density of the ambient medium n = 10, 100, 1000, 10^4, 10^5 cm^{-3}. The ages of the stellar cluster are indicated by gray shading.

velocity higher that the already shocked one creating a reverse shock. Such a structure is often referred to as energy-driven, adiabatic wind bubble.

More recently, the importance of radiation pressure in the first phases of H II region expansion, especially those powered by many OB stars, has been stressed both theoretically (Krumholz & Matzner 2009) and observationally (Murray & Rahman 2010). This model has received further impetus by recent studies that show that stellar winds from high mass stars are not as strong as previously thought and that (at least for a population of H II regions) the main driver cannot be the stellar wind (Najarro et al. 2011, Matzner 2002) .

4.3.2   Comparison to observations

Each of these theories for the expansion of H II regions predicts the size as a function of time. The results of these dynamical models can be compared to the observations. We do so for Hubble V and Hubble X in Figure 4.6. The radius of each H II region comes

from the Hα maps (circles in Figure 4.1 and 4.3) and the age is the upper limit from the stellar population analysis of Bianchi et al. (2001). These are summarized in Table 4.1. For the Castor et al. (1975) solution we need an estimate of the mechanical luminosity of stellar wind. We derive this using the Vink et al. (2000) mass loss recipe at metallicity 0.4 $Z_\odot$ for each identified massive star, as mentioned in Section 4.2.2. We estimate the total L_{mech} as the sum of the contribution of each star. We derive $L_{mech} = 4 \times 10^{35}$ ergs^{-1} for Hubble V and 8.3×10^{34} ergs^{-1} for Hubble X. For the Krumholz & Matzner (2009) solution f_{trap} is the free parameter representing how many times a photon can be used, or how much momentum each photon can deposit into the gas each time it scatters. We use $f_{trap} = 2$, the preferred value in radiation-hydrodynamic simulations of Krumholz & Thompson (2012, 2013). The parameter f_{trap} is important for very luminous clusters, but in the case of our two H II regions, it does not have much influence on the result.

Figure 4.6 shows the predictions of the theoretical models applied to our regions. For adopted ages of 2-4 Myr (see Section 4.2.2 and 4.4.2) and depending on the model, we infer ambient medium densities between 10^4 and 10^5 cm^{-3} for Hubble V, and between 100 and few 10^3 cm^{-3} for Hubble X. We note that for Hubble V, a density of $\sim 10^3$ cm^{-3} is only allowed if the age is substantially less than 1 Myr (Figure 4.6).

4.4   Diagnostic diagrams

The BPT diagram is a useful tool to diagnose emission line origins observed in external galaxies and to distinguish star-forming galaxies dominated by H II regions from active galactic nuclei (AGNs). A BPT diagram consists of emission line pairs of forbidden lines over recombination lines, which are indications of ionization per unit volume. The line ratios [O III]/Hβ versus [N II]/Hα are particularly useful because the wavelengths in each line ratio pair are similar thus insensitive to foreground extinction, and these emission lines are bright (Veilleux & Osterbrock 1987). Individually resolved H II regions form a narrow and well defined sequence of [O III]/Hβ and [N II]/Hα ratios in such plot, while regions ionized by a power-law ionizing spectrum, such as AGNs, are offset (Groves et al. 2004). An H II region's properties, such as density and metallicity, will change the region's location within this narrow sequence on the BPT diagram.

Brinchmann et al. (2004) found from the SDSS that unresolved star-forming galaxies in the local universe fall along the same narrow sequence as individually resolved H II regions. Detailed studies of nearby H II regions provide local analogs to star formation sites in distant galaxies. Therefore, it is important to understand physical processes involved in determining H II region locations along the sequence in BPT diagrams and their relation with the whole star forming galaxies. Chapter 5 and 6 studied how an increase of the environment pressure and the H II regions models affect the location of a galaxy on the diagnostic diagram, while Kewley et al. (2013a) and Kewley et al. (2013b) analyzed the evolution of galaxies on the BPT plot with redshift taking into account both star-forming and AGN galaxies.
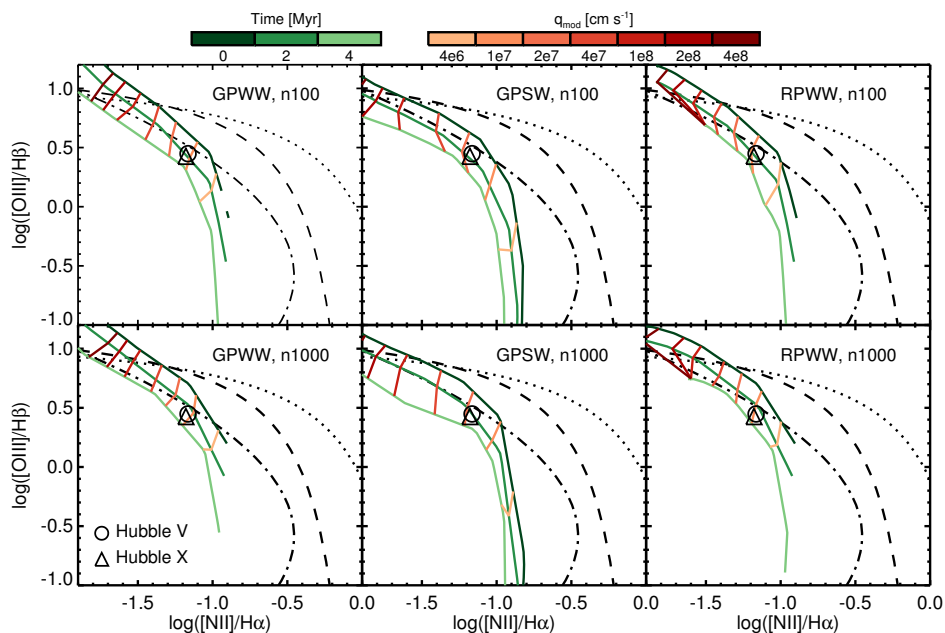
Figure 4.7 – BPT diagram for the photoionization models with initial densities 100 (top row) and 1000 cm^{-3} (bottom row): gas pressure with weak winds (GPWW) on the left, gas pressure with strong winds (GPSW) in the center, and radiation pressure and weak winds (RPWW) on the right. We evolve the models from 0 to 4 Myr (green colors) and we show them with lines of constant q_{mod} parameter (orange). Hubble V and Hubble X integrated measurements are shown as filled circle and square respectively. The dashed line is the Kauffmann et al. (2003) line, an empirical separation of star forming galaxies and AGN based on SDSS galaxies. The dotted line is the Kewley et al. (2001) theoretical limit for star forming galaxies. The dot-dashed line is a fit to the star forming galaxies from the SDSS galaxies Brinchmann et al. (2008).

4.4.1   Spectral synthesis and photoionization models

To investigate the physical properties of Hubble V and X, we construct photoionization models in the same fashion described in Yeh et al. (2013). We briefly describe our model parameters in this paper, for more details we refer readers to Yeh et al. (2013).

We generate a population of static, single H II regions with a wide range of luminosities and sizes. First we use the stellar population synthesis code Starburst99 (Leitherer et al. 1999) to generate coeval star clusters' spectra of age 0 to 6 Myr, employing the Geneva standard evolutionary tracks (Charbonnel et al. 1996, Schaerer et al. 1993b,a, Schaller et al. 1992) with 0.4 Z$_\odot$, and Lejeune-Schmutz (Lejeune et al. 1997, 1998, Schmutz 1998) stellar atmospheres. We then feed the Starburst99 spectra into Cloudy 13.00, last described by Ferland et al. (2013), as the ionizing source in the center of each pseudo H II region, which is spherical and in force balance. We adopt Cloudy pre-stored

ISM dust grain size distribution and fix the abundances at $0.4\,Z_\odot$[4], with the same gas phase abundances as Dopita et al. (2000). Number density of the hydrogen nuclei at the inner radii of H II regions is fixed at 100 and 1000 cm^{-3}, with the total luminosity of continuum spectra 10^{34} to 10^{46} erg s^{-1} in 0.2 dex steps. Outputs of the integrated luminosity of Hα, Hβ, [O III], and [N II] are recorded for the gas pressure weak wind (GPWW) model, gas pressure strong wind (GPSW) model, and radiation pressure weak wind (RPWW) model (Chapter 5).

The GPWW model are filled Strömgren spheres with uniform gas pressure, comparable to the Spitzer (1978) analytic model. The GPSW model produces regions with a large "voids" in the center filled with hot and diffuse stellar wind gas; ionized gas is confined to a thin shell between the stellar wind bubble and the ionization front, aimed at reproducing the Castor et al. (1975) solution. Finally, the RPWW model represents H II regions of radiation pressure-driven ionized shells, in which radiation pressure is the dominant mechanism for shell expansion and stellar winds are negligible, as described by the Krumholz & Matzner (2009) analytic solution. For detailed discussion and implications of each model, see Chapter 5 and 6.

Figure 4.7 shows results of the GPWW, GPSW, and RPWW model in the BPT diagram for initial densities of 100 and 1000 cm^{-3}. The plot shows the outcome of the models depending on age of the stellar population and on the ionization parameter, q_{mod}. The ionization parameter q is the ratio of the ionizing photon flux to the gas density. It gives an indication of the degree of ionization of an H II region and is defined as

$$q = \frac{\mathbb{N}_{Lyc}}{4\pi R^2 n_e} \, , \tag{4.3}$$

where R is the radius of the H II region and n_e is the electron density. We evaluate the ionization parameter expected from the models, q_{mod}, at the ionization front radius of each simulated H II region. For the electron density, we use the density of the inner shell for models GPWW and GPSW because the density structure for the set of parameters used does not change significantly. For RPWW models we use the density of the shell at the ionization front as predicted by the models, which is usually higher than the initial one due to radiation pressure piling material up towards the ionization front (Draine 2011, Yeh & Matzner 2012).

4.4.2 Results

The GPWW, GPSW and RPWW photoionization models have some common features (Dopita et al. 2000, Kewley et al. 2001, Levesque et al. 2010). The age of the stellar population causes the [O III]/Hβ ratio to shift down with increasing age. Ages larger than 4 Myr make the models drop dramatically because the most massive stars move out of the main sequence. The ionization parameter increases from right to left on the plot. The metallicity has the effect of shifting the models towards lower [N II]/Hα values (see also

---

[4] We scale the abundances linearly for all elements with the exception of helium, nitrogen and carbon, for which we adopt the scaling relations in Dopita et al. (2006a).
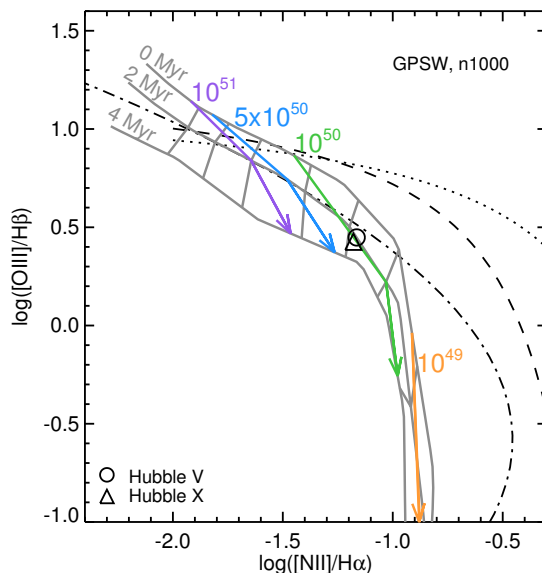
Figure 4.8 – Predicted evolution in time of H II regions on the BPT diagram. Gas pressure with strong winds (GPSW) grid models are in grey. Arrows indicate increasing time evolution for H II regions with number of ionizing photons from 10^{49} to 10^{51} s^{-1}. Other lines and symbols are as Figure 4.7.

Figure 6.3 and 6.4). The increase of the density in which the H II region expands has only small effects on the location of the models in the plot. GPWW and RPWW have very similar results in terms of shape of the overall models with one main difference in the ionization parameter: at a give location, the q_{mod} of the GPWW is systematically higher than q_{mod} of the RPWW by about a factor 2. As expected, GPWW H II regions are systematically smaller, therefore have higher q_{mod}, than the RPWW ones. As also visible in Figure 4.6, radiation pressure acts as extra force added to the gas pressure driven expansion of the H II region.

Figure 4.7 also shows the location of our two H II regions. Despite the different surrounding densities, both H II regions fall in a very similar location of the BPT diagram. All three models can reproduce the location of the observed regions with fairly similar ionization parameters in the case of gas pressure models and with slightly smaller q values for RPWW model. We discuss this further in Section 4.5.3. We derive q value for those H II regions of 1-4×10^7 cm s^{-1} for gas pressure models and 4×10^6-10^7 cm s^{-1} for radiation pressure models. The age is restrictd to 2-4 Myr in all models.

As an H II region ages and expands, the ionization parameter changes. While it is straight forward to see the trend with age on a grid of models, predicting how the ionization parameter changes is not obvious, because it depends on the radius of the expansion

and on the density structure created by the H II region. We show an example of our prediction for the evolution of an H II region in Figure 4.8. At a fixed number of ionizing photons, we calculate the radius according to the analytic solutions described Section 4.3. We use the appropriate density at the ionization front as found in the photoionization models (important for the RPWW models) to calculate the ionization parameter that gives the BPT diagram location. The evolutionary tracks predict that H II regions move on the BPT diagram from high [O III]/Hβ and low [N II]/Hα values towards lower [O III]/Hβ and a fixed value of [N II]/Hα that will depend on the metallicity. In order to populate the top part of the diagram, H II regions must be formed by massive stars, to have enough ionizing photons to excite the [O III], and they must be young. When comparing to Hubble V and X, we find again that all the derived parameters (Table 4.1) are consistent with the expected values from Figure 4.8.

4.5 Discussion

In Sections 4.3 and 4.4, we have illustrated unidimensional analytical models and photoionization models for the specific case of Hubble V and X. We expect that those two H II regions are good analogues of H II regions dominating the emission of SDSS galaxies. We connect the information derived from two single cases to the more general trend of the star forming galaxies. Before doing so, we discuss here the physical parameters that we have constrained using the combined efforts of observations and theory.

In order to assess the evolution of the H II region and its physical conditions, it is important to disentangle the degeneracy between age and density of the medium. Consider a star or stellar cluster of known ionizing photons with an observed radius r. Such a radius is the result of the expansion of the H II region in time into its surrounding medium of density n. If we can derive one of the two parameters, we know the other. We discuss here how we derive a tighter constraint on the age of the H II region using the photoionization models, and we prove that the ambient densities derived from observations are lower limits.

4.5.1 Age

Bianchi et al. (2001) used photometric studies of the two clusters to construct H-R diagrams. They derive an upper limit on the age of the stellar cluster of 4 Myr by comparing the data with stellar evolution isochrones. Supporting evidence for a young age comes from the lack of supernovae signature. Shocked gas and H II regions are clearly separated in the BPT diagram, with shocked gas being on the top right part of the plot (Groves et al. 2004). We do not find any indication of shocked gas in the two fields. Considering a single burst of star formation, SN explosions happen after about 3.5 Myr. The lack of SN support that our two clusters have an age less than 3.5 Myr.

We show in Figure 4.7 a set of photoionization models. We can assume that both Hubble V and X come from one single burst of formation, then independently of the

model used to describe the driving mechanism of the H ɪɪ region, both star-forming regions are less than 4 Myr old.

We derived a relatively strong constraint on the age of the stellar population using two different methods. We note that while the isochrone methods are unable to distinguish an age less than 4 Myr, photoionization models together with the BPT diagram give a more precise estimate. Optical lines are very sensitive to the hard radiation coming from high mass stars which evolve very fast to Red supergiant and/or Wolf Rayet star. As a result the BPT plot becomes a more sensitive tool to determine stellar age than isochrones on the H-R diagram.

4.5.2   Density of the ISM

The gas-to-dust ratio is calculated by finding the total H ɪ mass and total dust mass over the main body of the galaxy. We perform aperture photometry over a 440″ radius (centered at ra = 296.208, dec = −14.778 in degrees J2000) on the H ɪ column density map and dust mass map discussed in Section 4.2.3. The total H ɪ mass over this area is $M_{\mathrm{H I}} \sim 6 \times 10^7$ M$_\odot$, assuming a distance of 490 kpc and adding the contribution of Helium. The total dust mass, using the amorphous carbon model, is $M_{dust} \sim 8.6 \times 10^4$ M$_\odot$. This results in a gas-to-dust ratio of approximately 700 by mass, neglecting contributions from H_2 and trace species. The inherent assumption is that the gas-to-dust ratio is equal to the one measured for the galaxy as a whole. Although dust properties are affected in H ɪɪ regions (Salgado et al. 2012) causing the value of the gas-to-dust ratio to decrease, the mean field is dominated by the swept up shell, not the ionized gas mass.

We select an circular region around the sources of radius 42 pc, that is the smallest region we can select: the beam size of the 500 μm maps is 12″ corresponding to ~ 28.5 pc at the source distance. From the dust maps, we calculate the total mass in dust, $M_{dust} \sim 9 \times 10^2$ M$_\odot$ and 1.1×10^3 M$_\odot$, respectively for Hubble V and Hubble X. By multiplying by the gas-to-dust ratio, we derive the total mass in the region for Hubble V M_{tot} is $\sim 6.2 \times 10^5$ M$_\odot$ and for Hubble X $\sim 7.7 \times 10^5$ M$_\odot$. We calculate the total mass of the ionized gas from the number of ionizing photons and the density of the ionized gas (Section 4.2.4 and Figure 4.5) obtaining for the two H ɪɪ regions, respectively, $M_{\mathrm{H II}} \sim 2.1 \times 10^3$ and 2.7×10^3 M$_\odot$. The ionized gas densities of $\sim 300\text{-}450$ cm^{-3} measures the dense shell of swept up ionized material; it is not a direct measure of the density of the ambient medium. In terms of mass, the ionized gas has a minor contribution to the total budget. Finally, we derive the density of the ISM by dividing the total mass by the volume of the sphere with radius 42 pc. We get a Hydrogen density $n_{\mathrm{H}} \sim 61$ cm^{-3} for Hubble V and $n_{\mathrm{H}} \sim 52$ cm^{-3} for Hubble X. Note that these are higher than the values estimated directly from H ɪ in Section 4.2.3.

The densities derived from observations are lower limits, and Figure 4.6 indicates that they are lower than necessary to confine the expanding H ɪɪ regions to the observed radii. In the previous section, we show via two independent methods that the regions cannot be older than 4 Myr, most probably ~ 2 Myr. With this estimate in mind we can go back to Figure 4.6 and derive the density of the medium surrounding the H ɪɪ regions. Almost independently of the expansion model one considers, Figure 4.6 indicates that the density

in both regions must be higher than the values derived with the dust maps.

In the case of Hubble V, the discrepancy between the predicted and estimated values of the ISM density is of a factor of 150 to 1000 (depending on the models), while in the case of Hubble X is smaller. For Hubble X the expected density of the ISM is between 100 and 800 cm^{-3}, for Spitzer (1978) and Castor et al. (1975) models, and up to few thousands for Krumholz & Matzner (2009). Therefore, the values of the density of the medium derived from observations are a factor of 2 to 16 lower than predicted by the first two analytical models. Such a difference between the two H II regions might be due to the morphology. The analytical models are unidimensional, suitable for spherical and confined H II regions. It might explain the better fit for Hubble X, that has an almost spherical appearance. While looking at the optical image of Hubble V and the location of the dust clump, it seems indicating that the H II region is open on one side and that gas is leaking out in a champagne flow.

Despite the discrepancies between models and observations, we can deduce some important points. First, Hubble V must be in the vicinity of a high density clump on scales smaller than those measured that stops the expansion on one side and that generates the strong emission lines. Second, the density derived from observations is a lower limit indicating that we are possibly missing dust in the detection, indication that the IR data is dominated by the emission from warm dust in the PDR and that much of the dust in the swept up shell is very cold and escapes detection with Herschel.

4.5.3 Ionization parameter

We derive two independent estimates of the ionization parameter q, one from observations q_{obs} that can be compared with the values derived from models, q_{mod} in Section 4.4.1. We fix the number of ionizing photon flux to the observed value in both observational and theoretical estimates. We use the values of $\mathbb{N}_{Lyc}$ as listed in Table 4.1.

To derive q_{obs}, we use the radius of the region as seen from Hα. We derive the electron density from [S III] maps in 18 and 33 μm as described in Section 4.2.4 and shown in Figure 4.5. For Hubble V the average electron density within the bubble is ~ 450 cm^{-3}, while in Hubble X is $n_e \sim 300$ cm^{-3}, giving q_{obs} values of 1.1×10^8 and 3.1×10^7 cm s^{-1} respectively. Figure 4.7 shows the grid of models on the BPT diagram, from which it is possible to see that the ionization parameter is approximately between 1 and 4×10^7 cm s^{-1} for all models. Considering the uncertainties and the assumptions made, we can say that for both H II regions the estimates of the ionization parameter derived from observation and theory are consistent. Both regions have similar ionization state, which is what it is typically found for H II regions in the local universe. However, Hubble V has an observed ionization parameter higher than expected from the models (Section 4.4.2). It could be due to geometrical effects caused by a deviation from spherical of the H II region's shape.

4.5.4 Comparison with SDSS galaxies

Star-forming galaxies and H II regions in the local universe follow the same sequence in the BPT diagram, suggesting that star-forming galaxies can be simplified as a collection
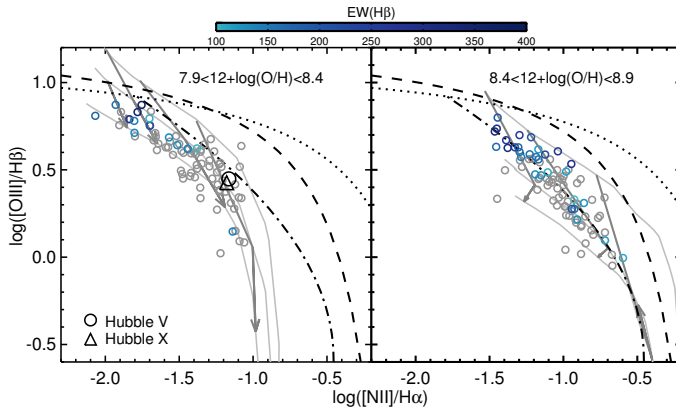
Figure 4.9 – Sub samples of SDSS data on the BPT plot. We selected star forming galaxies from the SDSS catalogue that have a spectrum of a region less than 200 pc in diameter and divided them in two metallicity bins: 12+log(O/H) between 7.9 and 8.4, and between 8.4 and 8.9, corresponding respectively to 0.4 and 1 $Z_\odot$. We further divide the sample into galaxies with EW(Hβ) below 100 Å in gray circles, and above 100 Å, color coded according to their EW(Hβ). Models GPWW with 0.4 and 1 $Z_\odot$ for ages 0, 2 and 4 Myr are shown together with the self-consistent predictions of evolution of H II regions in time (grey lines). Hubble V and Hubble X integrated measurements are shown as open circle and square respectively.
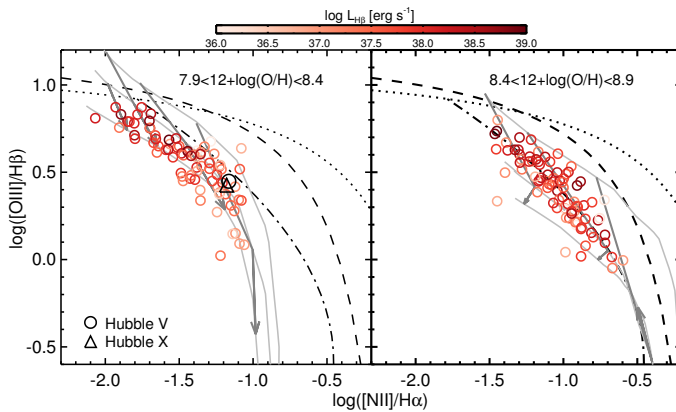
Figure 4.10 – Sub samples of SDSS data on the BPT plot. We selected star forming galaxies from the SDSS catalogue that have a spectrum of a region less than 200 pc in diameter and divided them in two metallicity bins: 12+log(O/H) between 7.9 and 8.4, and between 8.4 and 8.9, corresponding respectively to 0.4 and 1 $Z_\odot$. Each data point is color coded according to the logarithm of the luminosity in Hβ. Models GPWW with 0.4 and 1 $Z_\odot$ for ages 0, 2 and 4 Myr are shown together with the self-consistent predictions of evolution of H II regions in time (greylines). Hubble V and Hubble X integrated measurements are shown as open circle and square respectively.

of H II regions. Contamination from warm ionized gas has an influence only on galaxies with low specific star formation rate (Mathis 2000, Brinchmann et al. 2004) that is not relevant for this discussion. In this Section, we compare star-forming galaxies dominated by H II regions with single H II regions based on their location on the BPT diagram.

In Chapter 6 we created synthetic galaxies as collections of H II regions using a population synthesis code aimed at understanding the star forming sequence of galaxies. We generated H II regions according to an initial mass function and a constant star formation rate. We evolved each H II regions according to an analytic expansion models (Spitzer 1978, Krumholz & Matzner 2009) and we predicted their line emission with photoionization models. We found that the main difference between models with low (0.1 $M_\odot$ yr^{-1}) and high (10 $M_\odot$ yr^{-1}) star formation rate is due to the number of massive H II regions formed at each time, and it decides the spread of synthetic galaxies on the BPT diagram. The low star formation case generates galaxies with a large spread on the BPT diagram, while galaxies generated with high star formation rate are more concentrated. It is due to the stochastic nature of star formation: for low star formation rates most of the H II regions formed are powered by relatively late spectral types (eg. $\sim$ O9) that have weak emission lines and a low [O III]/Hβ ratio. Whenever a bright H II region is formed, its light dominates over the entire galaxy and brings the [O III]/Hβ ratio up, causing the spread in values. When the SFR is high, there is always a massive H II region to keep the ratio up, therefore showing no spread on the BPT diagram. In other words, with a constant star formation rate, the most massive and youngest H II region dominates the light of the entire galaxy, with only a weak influence of the underlying old stellar population.

Hubble V and Hubble X are two examples of young and bright H II regions, they are good analogues of the H II regions dominating the emission in star forming galaxies. We compare our single H II regions to a selection of star forming galaxies from the SDSS data. We can also use the information we have on the two H II regions to further validate the way we extrapolate physical information from the diagram. We selected galaxies in the SDSS sample that have spectra of regions less than 200 pc in diameter. In this way, we try to minimize the effect of contamination due to emission from the warm ionized medium. For those galaxies, we take the equivalent width of Hβ (EW(Hβ)) as an indicator of young stellar population. When the EW(Hβ) is > 100 Å then the star formation and light are dominated by a very young population without contamination from an underlying old stellar population. We divide the sample into young sources with EW(Hβ) > 100 Å, and old sources < 100 Å. We further split the sample according to metallicity: 12 + log(O/H) between 7.9 and 8.4, and between 8.4 and 8.9 (corresponding to 0.4 and 1 $Z_\odot$); and plot the data on the BPT diagram (Figure 4.9). We find that young sources are systematically shifted towards the top part of the BPT diagram, suggesting that their light must be dominated by massive H II regions. Hubble V and X are located towards the low end of the distribution of young galaxies, indicating the time evolution of such galaxies.

In Figure 4.10 we consider the same sample of star forming galaxies divided into metallicity bins, and show their Hβ luminosity. Even though the trend is not as clear as in the previous plot, there is an indication that galaxies dominated by young H II regions are also the most luminous in Hβ. The luminosity of the emission line Hβ is an indication of the star formation activity in the galaxy because its emission comes primarily from

high mass stars present in the galaxy. Therefore, Figure 4.10 confirms that the location of galaxies on the star forming sequence of the BPT diagram is partially due to the presence and age of high mass stars.

From the comparison between single H ɪɪ regions and star forming galaxies, we can draw the following conclusions. First, galaxies dominated by young H ɪɪ regions show higher [O ɪɪɪ]/Hβ than the older ones and are found systematically on the top left part of the plot, independently of the metallicity and they are generally more luminous galaxies. Second, [N ɪɪ]/Hα value is mostly dependent on the metallicity that translates the data points on the plot almost rigidly. Third, when compared to the photoionization models, it is clear that the location of the galaxies dominated by young H ɪɪ regions is due to the combined effect of young age and high ionization parameter. Finally, Hubble V and Hubble X are located at the lower end of the young part of the star forming sequence, indicating that the most massive stellar cluster in blue star forming galaxies tend to be younger than our H ɪɪ regions.

4.6   Conclusions

We select two very well studied H ɪɪ region in the nearby galaxy NGC 6822: Hubble V and Hubble X. We use Hβ, [O ɪɪɪ], Hα, and [N ɪɪ] optical emission line images taken with the WFC2 camera from the HST to produce the BPT diagram and to look at the morphology of the two regions. We use photometry from Massey et al. (2007) to characterize the stellar population and the age of the region. Finally, we use broad band IR data to map the dust content that together with the estimates of the neutral gas from H ɪ maps from de Blok & Walter (2000) gives us the gas-to-dust ratio in the galaxy.

We make use of unidimensional analytical models to get a better constrain the density of the medium around each H ɪɪ region. We consider three theoretical descriptions of the expansion of H ɪɪ regions: Spitzer (1978) takes into account the overpressure caused by the ionization and heating of the H ɪɪ region; Castor et al. (1975) the mechanical energy of stellar winds; and Krumholz & Matzner (2009) the radiation pressure on the gas. Given the density of the ISM, each model describes the expansion radius of the ionization front as a function of time. The estimates of the density we derive from the models are few orders of magnitude higher than the observed ones indicating that we might be missing the detection of the very cold dust, probably because overpowered by the warm dust emission.

We test photoionization models for three possible H ɪɪ region driving mechanisms. We find no major difference between the models. Together with the BPT diagnostic diagram such models are able to confirm the young age of the clusters ($\sim$ 2 Myr) and the ionization state of the regions ($q \sim 10^7$ cm s^{-1}). We created evolutionary tracks on the BPT plot useful to understand general trends in the star forming sequence.

We find many similarities in the two H ɪɪ regions: they are both young, powered by similar stellar clusters, and have a similar ionization states. However their morphology is strikingly different. The brightest part of Hubble V is expanding in a very dense molecular cloud, $> 10^4$ cm^{-3}. Gas seems to escape towards the South-East part of the object, where

the density likely drops and a "champagne flow" begins. Hubble X has a more regular spherical shape and is expanding in a less dense ($\sim 10^3$ cm^{-3}) and more uniform medium.

We compare a selection of SDSS galaxies to models and to Hubble V and X in the BPT diagram. We use the equivalent width of Hβ as an indicator of recent start formation, and the luminosity of Hβ. We find that star-forming galaxies' locations in the BPT diagram is dominated by the few, very bright H II regions, rather than by the numerous dim stars. The location of Hubble V and X suggests that the evolutionary tracks derived from photoionization models are consistent with observations and can be extended to the more general case of star forming galaxies. We suggest that detailed studies of global properties of H II regions will help disentangle the debate on their driving mechanisms.

V

Line emission from radiation-pressurized H II regions. I. Internal structure and line ratios

The emission line ratios [O III] $\lambda5007$/Hβ and [N II] $\lambda6584$/Hα have been adopted as an empirical way to distinguish between the fundamentally different mechanisms of ionization in emission-line galaxies. However, detailed interpretation of these diagnostics requires calculations of the internal structure of the emitting H II regions, and these calculations depend on the assumptions one makes about the relative importance of radiation pressure and stellar winds. In this paper we construct a grid of quasi-static H II region models to explore how choices about these parameters alter H II regions' emission line ratios. We find that, when radiation pressure is included in our models, H II regions reach a saturation point beyond which further increases in the luminosity of the driving stars does not produce any further increase in effective ionization parameter, and thus does not yield any further alteration in an H II region's line ratio. We also show that, if stellar winds are assumed to be strong, the maximum possible ionization parameter is quite low. As a result of this effect, it is inconsistent to simultaneously assume that H II regions are wind-blown bubbles and that they have high ionization parameters; some popular H II region models suffer from this inconsistency. Our work in this paper provides a foundation for a companion paper in which we embed the model grids we compute here within a population synthesis code that enables us to compute the integrated line emission from galactic populations of H II regions.

Sherry C. C. Yeh, Silvia Verdolini, Mark R. Krumholz, Christopher D. Matzner, Alexander G. G. M. Tielens

5.1   Introduction

The line ratios [O III] $\lambda5007$/Hβ and [N II] $\lambda6584$/Hα, first proposed for use in galaxy classification by Baldwin et al. (1981) (hereafter BPT), are commonly used to diagnose the origins of emission lines from galaxies, and in particular to discriminate between galaxies whose emission is powered by star formation-driven H II regions and from those powered by active galactic nuclei (AGNs). These emission line pairs are particularly useful because (1) they are bright and thus relatively easy to measure, (2) blending between the lines can be corrected with reasonable accuracy, so long as the spectra are taken with sufficient resolution, and (3) the wavelengths in each line pair are quite similar, so the line ratio is relatively insensitive to dust-reddening (Veilleux & Osterbrock 1987).

The power of these line ratios as diagnostics comes from their sensitivity to the spectral shape of the radiation field driving the ionization, which can be understood from a simple physical picture. To first order, the intensities of the Hα and Hβ lines simply measure the total photoionization rate, and thus normalize out the ionizing luminosity. On the other hand, the [O III] and [N II] intensities are sensitive not only to the total ionizing luminosity, but also to the shape of the ionizing spectrum and to the ionization parameter $\mathcal{U}$, which measures the ratio of photons to baryons in the ionized gas. When the ionizing flux arises from hot stars, the ionizing spectrum is dominated by low-energy photons that have short mean-free paths through neutral gas. Thus the H II region consists of a fully ionized zone with a sharp boundary. Within this region, as $\mathcal{U}$ increases, more of the ionized gas volume becomes filled with high ionization potential species such as O^{++}, and less with low ionization potential species such as N^+. As a result, H II regions ionized by hot stars tend to fall along a sequence that runs from high [O III]/Hβ, low [N II]/Hα to low [O III]/Hβ, high [N II]/Hα. On the other hand, if the ionizing spectrum follows a power-law, as expected for AGN, then a significant amount of the ionization is produced by X-ray photons capable of ionizing higher ionization potential species like O^{++}. Moreover, these photons have large mean-free paths, giving rise to a large zone of partial ionization rather than a smaller region of full ionization as in the stellar case. In this configuration, [O III]/Hβ and [N II]/Hα both increase with $\mathcal{U}$, and either one or the other tends to be larger than in the stellar case, leading to a sequence that runs from intermediate to high [O III]/Hβ and [N II]/Hα and is well-separated from the locus occupied by H II regions dominated by stellar sources.

This simple picture is roughly consistent with local observations: star-forming galaxies in the Sloan Digital Sky Survey (SDSS; median redshift $z = 0.1$) obey a tight correlation between the [O III]/Hβ and [N II]/Hα ratios in the BPT diagram (Brinchmann et al. 2004, Tremonti et al. 2004). However, higher redshift star-forming galaxies are offset from this sequence to higher values of [O III]/Hβ, without joining the locus of points occupied by AGN in the SDSS sample (Shapley et al. 2005, Erb et al. 2006b, 2010, Brinchmann et al. 2008, Liu et al. 2008). As our work is motivated by a desire to better understand the physical information encoded in the BPT diagram, we pause to consider how this shift in the BPT locus might arise.

The difference in line luminosity ratios could be intrinsic to the galaxies' H II regions. As we have said, the ionization parameter is a major controlling factor which positions

regions *along* the star-forming locus. Line emission from these regions will be also affected by the metallicity and dust content of the interstellar gas; by the density of that gas (through the critical densities of the lines); by the ionizing spectra of the stars (which reflect stellar masses, metallicities and rotation rates). In addition, stellar winds can alter the boundary conditions for ionized zones, a point discussed by Yeh & Matzner (2012, hereafter YM12) and to which we return below.

Alternatively, the shift in the BPT diagram could arise from outside the H ii regions if their light is mixed with line emission from shocks or an unresolved AGN (e.g., Liu et al. 2008). Indeed, Wright et al. (2010) use integral field spectroscopy to demonstrate that a weak AGN is responsible for the shift in a single galaxy at $z = 1.6$, and Trump et al. (2011) stack HST grism data of many galaxies to show that this phenomenon is reasonably common. Taken together, these studies raise the possibility that H ii regions at $z \approx 2$ lie along the same BPT locus as those nearby, and the shift is an optical illusion caused by active nuclei.

However, the distribution of high-redshift galaxies in the BPT diagram is *also* shifted in the direction of high $\mathcal{U}$. Because radiation pressure rises, relative to gas pressure, in proportion to $\mathcal{U}$, this implies that the radiation force typically is more important in high-redshift galaxies. This radiation-force-dominated condition is also more prevalent among starburst galaxies in the local Universe, as YM12 argue on the basis of mid-infrared line emission. This possibility has also received significant support from recent resolved observations of H ii regions, which provide direct evidence that radiation pressure is significant for the most luminous examples (Lopez et al. 2011, but also see Pellegrini et al. 2011 and Silich & Tenorio-Tagle 2013).

The detailed role of radiation pressure in altering the line ratios of starlight-ionized H ii regions has received relatively little attention, although the phenomenon has been explored in the context of AGN narrow-line regions (Binette et al. 1997, Dopita et al. 2002). Early models ignored radiation pressure entirely (e.g. Dopita et al. 2000, hereafter D00). Although more recent models include radiation pressure (e.g. Dopita et al. 2005, 2006a,b, Groves et al. 2008, Levesque et al. 2010), it is either explicitly or implicitly assumed that the geometries and internal structures of H ii regions are dominated by stellar wind bubbles rather than radiation pressure. As we discuss below, the assumption that stellar wind pressure exceeds radiation pressure is often physically inconsistent with the range of ionization parameters being probed. Moreover, resolved observations of the brightest nearby H ii regions indicate the hot gas produced by shocked stellar winds for the most part does not remain confined within H ii regions, and instead leaks out into the low-density ISM (Townsley et al. 2003, Harper-Clark & Murray 2009). As a result, the pressure of shocked stellar wind gas is often smaller rather than larger than radiation pressure (Lopez et al. 2011; YM12)[1].

In this paper we explore how radiation pressure influences the line emission of H ii

---

[1] Note that Pellegrini et al. (2011) assume a smaller filling factor for the X-ray emitting gas, and so assign it a much higher pressure than Lopez et al. (2011). For the same luminosity, small, higher-pressure bubbles have a greater dynamical effect on their immediate surroundings. But these bubbles are less important for the entire region than large, lower-pressure ones. This is a consequence of the virial theorem, which ties dynamics to the net energy budget.

regions. To do so, we compute a sequence of hydrostatic H II region models under a variety of physical assumptions about the relative importance of radiation pressure and stellar wind pressure (Section 5.2), and we explore how varying the physical assumptions alters the loci occupied by the model H II regions in the BPT diagram (Section 5.3). We then compare our models to those published by other authors (Section 5.4) and draw conclusions (Section 5.5). In a companion paper (Chapter 6, hereafter Paper II), we use the grid of H II region models presented in this paper to construct a population synthesis model capable of predicting the line ratios of star-forming galaxies containing many different H II regions. We use these models to compare to observations of star-forming galaxies. Although this study cannot replace a full investigation of the factors affecting the H II region locus within the BPT diagram, it is the first to explore the roles of radiation and wind pressure.

5.2 Photoionization models

5.2.1 Input parameters and calculations

To study the influence of radiation pressure on H II regions, we construct a grid of static, single H II regions, with a wide range of sizes, ionizing luminosities, and wind strengths. Our procedure is as follows. We first use the stellar population synthesis code Starburst99 (Leitherer et al. 1999) to generate spectra from coeval star clusters. We assume that all of the clusters are massive enough to fully sample the stellar initial mass function, which we take to have exponents –1.3 and –2.3 between stellar mass boundaries 0.1, 0.5, and 120 $M_\odot$. We employed the Geneva standard evolutionary tracks (Charbonnel et al. 1996, Schaerer et al. 1993a,b, Schaller et al. 1992) with solar metallicity, and Lejeune-Schmutz stellar atmospheres (Lejeune et al. 1997, 1998, Schmutz 1998), which incorporate plane-parallel atmospheres and stars with strong winds. We record the Starburst99 output spectra for cluster ages of 0 to 11 Myr at 0.5 Myr intervals.

We then use the photoionization code Cloudy 08.00, last described by Ferland et al. (1998), to compute the structure of static, spherical H II regions driven by point sources whose spectra are taken from the Starburst99 calculations. In addition to the spectrum of the driving source, Cloudy requires a number of other input parameters. The first of these is the total luminosity of the ionizing source, for which we run a series of models with $L = 10^{33}$-10^{46} erg s^{-1} in 1 dex steps. The second is the number density of hydrogen nuclei at the innermost zone of the H II region, which we set to values from $n_{H,in} = 10^{-1}$-10^5 in steps of 1 dex. The third is the distance of the innermost zone from the point source, which we vary from $R_{in} = 10^{-2}\,\tilde{r}_{ch}$-$10^2\,\tilde{r}_{ch}$ in steps of 0.2 dex. Here the characteristic radius

$$\tilde{r}_{ch} = \frac{\alpha L^2}{12\pi(2.2k_B Tc)^2 S} \tag{5.1}$$

is the radius of a uniform-density, dust-free Strömgren sphere for which the gas pressure is equal to the unattenuated radiation pressure at its edge (Krumholz & Matzner 2009; YM12); in this equation, α is the recombination rate coefficient, T is the gas temperature,

Table 5.1 – Comparison of model parameters

	Dopita et al. 2000 Model	Our Model	Levesque et al. 2010 Model
Ionizing spectra	Starburst99	Starburst99	Starburst99
Initial mass function	Salpeter, M_{up} = 120 $M_\odot$	Default Starburst99 IMF[a] M_{up} = 120 $M_\odot$,	Salpeter, M_{up} = 100 $M_\odot$
Stellar tracks	Geneva standard	Geneva standard	Geneva high mass-loss
Stellar atmospheres	Lejeune-Schmutz	Lejeune-Schmutz	Pauldrach/Hillier
Photoionization code	MAPPINGS III	Cloudy v08.00	MAPPINGS III
Radiation pressure	Not included	Optional	Included
Geometry	Plane-parallel	Spherical	Plane-parallel
H II region state	Uniform gas pressure	Hydrostatic	Isobaric[b]
Metallicity	Solar	Solar	Solar
Gas Phase Abundances (logarithmic, relative to H)			
H	0	0	0
He	–1.01	–1.01	–1.01
C	–3.74	–3.74	–3.70
N	–4.17	–4.17	–4.22
O	–3.29	–3.29	–3.29
Ne	–3.91	–3.91	–3.91
Mg	–5.12	–5.12	–5.12
Si	–5.45	–5.45	–5.45
S	–4.79	–4.79	–5.19
Ar	–5.44	–5.44	–5.44
Ca	–8.16	–8.16	–8.16
Fe	–6.33	–6.33	–6.33

[a] IMF exponents: 1.3 and 2.3 at mass boundaries 0.1, 0.5, and 120 $M_\odot$.

[b] L10 included radiation pressure in their isobaric calculations, thus the hydrostatic condition reduces to a state of uniform total pressure in plane symmetry (YM12).

and L and S are the bolometric luminosity and the output of ionizing photons per unit time, respectively, from the point source. In all the calculations presented here we adopt the same fiducial parameters as YM12: $T = 8000$ K, $\alpha = 3.0 \times 10^{-13}$ cm^3 s^{-1}. Finally, we adopt Cloudy's default ISM dust grain abundance and size distributions at solar metallicity, but in order to allow more meaningful comparison between our results and those of D00, we adjust the gas-phase element abundances in our calculation to match theirs. These choices mean that the dust discriminant parameter (Draine 2011) takes the same value, $\gamma = 7.4$, as in YM12: so, dust opacity is significant within radiation pressure-dominated ionized zones. We summarize all the parameters we use in our calculations in Table 5.1. The Table also describes the parameter choices used in D00 and Levesque et al. (2010, hereafter L10).

For each set of input parameters, we use Cloudy to calculate the structure of the resulting H II region, halting at the point where the gas temperature drops to 100 K in order to ensure that the ionization front is fully enclosed. We perform each calculation twice, once with radiation pressure turned off, and once with radiation pressure turned on and allowed to exceed gas pressure (in contrast to Cloudy's default setting, which does not allow radiation pressure to be greater than gas pressure.)

5.2.2   Model outputs and physical parameters

The output of our calculations is two four-dimensional grids of models defined by the parameters $(t, n_{\mathrm{H,in}}, L, R_{\mathrm{in}})$, where t is the age of the stellar population used to generate the ionizing spectrum. One grid contains models with radiation pressure turned on, which we refer to as the RP models, and the other contains models with radiation pressure disabled, which we refer to as gas pressure, or GP, models. For each run in both model grids, we compute several optical emission line luminosities integrated over the ionized gas, including the lines used to construct the BPT diagram: Hα, Hβ, [O III], and [N II].

In order to understand the physical meaning of the results, it is helpful to characterize each model by two dimensionless numbers that can be computed from the Cloudy output. Following YM12, we define the radiation pressure parameter

$$\Psi \equiv \frac{R_{\mathrm{IF}}}{\tilde{r}_{\mathrm{ch}}}, \tag{5.2}$$

where R_{IF} is the radius of the ionization front (IF). A value of $\Psi < 1$ indicates that the entire IF falls within $\tilde{r}_{\mathrm{ch}}$, and thus that radiation pressure is more important than gas pressure in determining its structure. Again following YM12, we define a separate stellar wind parameter

$$\Omega \equiv \frac{P_{\mathrm{in}} V_{\mathrm{in}}}{P_{\mathrm{IF}} V_{\mathrm{IF}} - P_{\mathrm{in}} V_{\mathrm{in}}}, \tag{5.3}$$

where P_{IF} and P_{in} are the gas pressures at the edge of the ionization front and the innermost zone, respectively, and $V_{\mathrm{IF}} = (4/3)\pi R_{\mathrm{IF}}^3$ and $V_{\mathrm{in}} = (4/3)\pi R_{\mathrm{in}}^3$ are the volumes contained within the IF and the inner edge of the H II region, respectively. The inner edge of the photoionized region is the outer edge of the bubble of hot gas inflated by the stars'
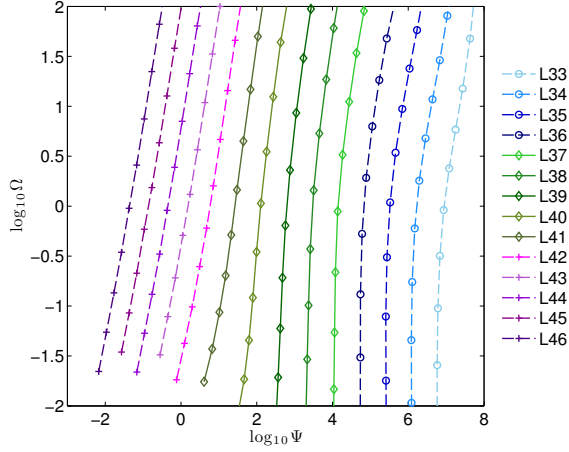
Figure 5.1 – An example of how our models fill the parameter space of Ψ and Ω. In the Figure, each plot symbol shows the values of Ψ and Ω computed for a particular calculation in our model grid at $t = 0$, $n_{\text{H,in}} = 10$ cm^{-3}, with radiation pressure on. Colors indicate lines of constant L, running from 10^{33}-10^{46} erg s^{-1} as indicated in the legend. The sequence of points along a given model corresponds to varying R_{in} from $10^{-2}\,\tilde{r}_{\text{ch}}$-$10^2\,\tilde{r}_{\text{ch}}$, with Ω increasing with R_{in}. Note that Ψ is a function of density as well as ionizing source luminosity. Radiation pressure can be significant in a high density region with relatively lower ionizing luminosity. Note that our full H II region model grids are incorporated into the dynamical models in Paper II.

winds. Thus Ω reflects the contribution of a pressurized wind bubble to the total energy budget of the H II region. In a region strongly pressurized by stellar winds $\Omega \gg 1$, while in a region with negligible wind pressure $\Omega \ll 1$.

For each Cloudy model, we compute the quantities Ψ and Ω, and thus we may think of our models as describing a parameter space $(t, n_{\text{H,in}}, \Psi, \Omega)$, as illustrated by Figure 5.1. This parameter space describes H II regions for which both radiation and wind pressure run from strong to negligible. To study the effects of winds, we reduce this four-dimensional parameter space to a three-dimensional one by selecting two representative values of Ω: we designate models with $\log \Omega = 2$ as *strong wind* (SW) models, and those with $\log \Omega = -1.5$ as *weak wind* (WW) models. Since our models never produce $\log \Omega = -1.5$ or 2 exactly, we construct these models by interpolation. At each age t, density $n_{\text{H,in}}$, and luminosity L, we find the two models whose values of Ω bracket our target one, and we compute line luminosities at the target value of Ω by interpolating between the two bracketing models.

Through this procedure, we obtain a set of four reduced model grids, which we refer to as RPWW (radiation pressure turned on, $\log \Omega = -1.5$), RPSW (radiation pressure turned on, $\log \Omega = 2$), GPWW (radiation pressure turned off, $\log \Omega = -1.5$), and GPSW (radiation pressure turned off, $\log \Omega = 2$).

It is important to bear in mind that our RP models are physically self-consistent, whereas the GP models are deliberately not. Thus, RPWW models make a transition from

classical spherical Strömgren spheres to radiation-confined shells, along the sequence described by Draine (2011), as Ψ decreases through unity. RPSW models are always thin shells: both radiation and wind pressure play a role in confining them, but, as we explain below, wind pressure always dominates. GPSW models are also thin shells, but due to the neglect of radiation pressure they sample a range of ionization parameters inaccessible to real regions. Finally, GPWW models are always filled Strömgren spheres, even when the radiation force should confine them. They can also sample unphysically high values of $\mathcal{U}$. Our GP models have strictly uniform gas pressure, as they include no other forces.

Table 5.2 – Model properties

Model	Acronym	Radiation pressure?	$\log \Omega$
Radiation pressure, weak wind	RPWW	yes	-1.5
Radiation pressure, strong wind	RPSW	yes	2
Gas pressure, weak wind	GPWW	no	-1.5
Gas pressure, strong wind	GPSW	no	2

Each of these model grids gives the line luminosities of H II regions as a function of the three remaining parameters, $(t, n_{\mathrm{H,in}}, \Psi)$, or equivalently (t, n_{H}, L). We summarize the properties of the models in Table 5.2. We will make use of the four full model grids in Paper II, but for the remainder of this paper we concentrate on the particular case $t = 0$, $n_{\mathrm{H,in}} = 10 \ \mathrm{cm}^{-3}$, in order to understand how the choice of input physics alters the structure of H II regions. We choose these parameters in particular because they match the ones used by a number of previous authors, thus facilitating easy comparison.

5.3 Results

5.3.1 One-zone models

For a given spectral shape, each ionized parcel with uniform density and temperature can be characterized by only two parameters: the density n_{H} and the ionization parameter $\mathcal{U} = n_{\gamma,i}/n_{\mathrm{H}}$, where $n_{\gamma,i}$ is the number density of ionizing photons. Therefore there is a unique mapping between $\mathcal{U}$ and initial densities on the BPT diagram. The one-zone models also represent simple analogs of H II regions, for one can decompose an H II region into zones in which $\mathcal{U}$, n_{H}, and ionizing spectrum are nearly constant. Thus the one-zone models represent thin, uniformly ionized regions which are very much like the ionized layer of a wind bubble. As such, they resemble best the SW models to be discussed in Section 3.2.2.

We run an additional set of Cloudy "one-zone" calculations in which we only compute the properties of line emission from the first, innermost zone. In this zone we can specify the value of $\mathcal{U}$ by choosing the the density n_{H} and the bolometric luminosity L (and thus the ionizing photon luminosity S). We run models with $n_{\mathrm{H}} = 10^{-1}\text{-}10^{6} \ \mathrm{cm}^{-3}$ in 1 dex
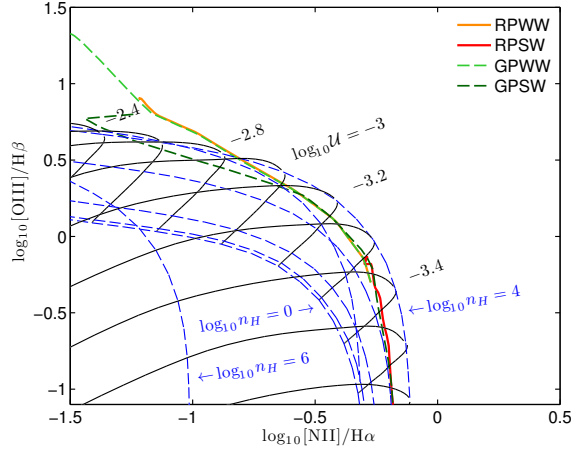
Figure 5.2 – Models in the BPT diagram. Full lines show one-zone models with constant $\mathcal{U}$, while dashed lines show one-zone models of constant n_{H}; both are calculated for an ionizing spectrum corresponding to a zero-age stellar population and Solar metallicity. We also show models RPWW, RPSW, GPWW, and GPSW (as indicated by the legend) with $n_{\mathrm{H,in}} = 10$ cm^{-3}, calculated with the same ionizing spectrum and metallicity.

steps, and $\mathcal{U} = 10^{-4}$-$10^{0.6}$ in 0.2 dex steps, all using an input spectrum corresponding to our $t = 0$ Starburst99 model, and using the same abundances and other parameters as the rest of our models.

In Figure 5.2, we show the constant $\mathcal{U}$ and constant n_{H} contours marked with black solids lines and blue dashed lines, respectively, on the BPT diagram computed with the one-zone models. The ionization parameter $\mathcal{U}$ and ionizing luminosity S increase from lower right to upper left, and increasing the density shifts models up and to the right, until the density exceeds $\sim 10^4$-10^5 cm^{-3}. Beyond this point, the models shift down and to the left, because the density exceeded the critical densities of the [N II] and [O III] emission lines, which are 6.6×10^4 cm^{-3} and 6.8×10^5 cm^{-3}, respectively (Osterbrock & Ferland 2006). In Paper II, we will return to the discussion of line ratios, $\mathcal{U}$, and critical densities on the BPT diagram, and further discuss most extreme H II regions exceeding the upper limit of line ratios set by Kewley et al. (2001), which is based on the mapping between line ratios and $\mathcal{U}$ but ignored the effect of densities.

We note that the BPT locations of macroscopic H II regions will differ from those of individual gas parcels, because of spatial variations in the physical quantities. In all cases $\mathcal{U}$ drops and the ionizing spectrum changes as one approaches the ionization front, because of selective absorption by neutral H atoms, and in some cases by dust grains. When radiation pressure is strong (and is included) and winds are weak, the gas density increases significantly across the layer. We therefore anticipate that full H II region models should differ from the one-zone calculation, even though the innermost zones are accounted by it. Moreover the macroscopic physical parameters, the assumed geometry,
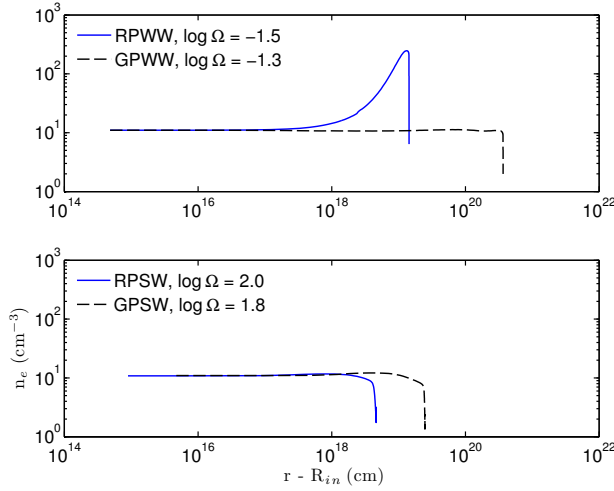
Figure 5.3 – Electron density versus radius for sample H II regions. Top panel: RPWW (solid line) and GPWW (dashed line) regions. Bottom panel: RPSW (solid line) and GPSW (dashed line) regions. The age of the ionizing star cluster in these regions is 0 Myr and the density at the inner boundary is 10 cm^{-3}. The luminosity in all models is 10^{43} erg s^{-1}. We select the value of $R_{\rm in}$ from our grid that gives $\log \Omega$ closest to -1.5 and 2; exact values of Ω for the four cases shown are as indicated in the legend. See Section 5.2.2 for details. Again we note that high luminosity is required here to reach radiation pressure-dominated state because the density is low.

and the inclusion or neglect of radiation pressure should affect the BPT loci. We explore these dependencies in the subsequent sections.

5.3.2 Full models

We now turn to our four full (radially resolved) H II region models, RPWW, GPWW, RPSW, and GPSW. In Figure 5.2, we overlay these models with $t = 0$ and $n_{\rm H,in} = 10$ cm^{-3} on the one-zone calculations. Other choices of density give qualitatively similar results, as long as the density is well below the critical densities of the [O III] and [N II] lines. As with the one-zone models, the full models form a sequence of values defined by Ψ or $\mathcal{U}$, which we control by varying L: high-Ψ, low-$\mathcal{U}$, low-L models are found at the bottom right and low-Ψ, high-$\mathcal{U}$, high-L ones at the top left of each sequence.

5.3.2.1 Weak wind models

When stellar wind pressure is negligible ($\log \Omega = -1.5$), H II regions at the low L end of the sequence are very similar to each other. This is because L determines the balance between radiation pressure and gas pressure; a high luminosity produces a large $\tilde{r}_{\rm ch}$ (Equation 5.1) and thus a small value of Ψ (Equation 5.2). Thus when L is low radiation pressure forces are negligible, and the results do not change much depending on

whether we include them or not. The density within both H II regions is roughly constant at $n_H = n_{H,in} = 10 \ \text{cm}^{-3}$.

At the high L, on the other hand, RPWW and GPWW differ substantially. In model GPWW, as L increases, we find that [O III]/Hβ increases and [N II]/Hα decreases without limit. In contrast, in model RPWW these line ratios saturate at a finite value. If one were to infer ionization parameters from these line ratios based on one-zone models, one would say that $\mathcal{U}$ saturates at a finite value in model RPWW, while in model GPWW it can increase without limit as L does. We can understand the difference in behavior by examining the density structures of RPWW and GPWW regions, of which we show an example in Figure 5.3. At high L, RPWW model H II regions are strongly dominated by radiation pressure. Under force balance, radiation pressure confines ionized gas into a much thinner layer and leads to a steep increase in density towards the IF. Much of the line emission comes from this dense layer, within which $\mathcal{U}$ is much lower than it is closer to the central source. YM12 discuss this effect in detail.

This effect does not operate in the GPWW models, where we have artificially disabled radiation pressure. As a result, these H II regions remain at nearly constant density regardless of the source luminosity. This allows $\mathcal{U}$ to increase without limit, and in turn allows the [O III]/Hβ and [N II]/Hα line ratios to continue changing even at large L.

Finally, it is interesting to note that, despite the uniform pressure in the GPWW models, the actual values of the line ratios are still significantly offset from the corresponding one-zone models of the same density, $n_H = 10 \ \text{cm}^{-3}$. At small L the shape of the sequence is similar but the models are displaced to slightly higher [N II]/Hα and [O III]/Hβ, while at large L the deviation is larger and the shape of the sequence is different as well. This difference occurs because, even though the pressure is uniform in the GPWW models, other quantities are not. In particular, the spectrum of the ionizing radiation field varies with radius, due to selective absorption of lower-energy photons by neutral H atoms and of higher-energy photons by dust within the ionized layer.

5.3.2.2 Strong wind models

In the RPSW and GPSW models ($\log \Omega = 2$), strong stellar wind pressure produces large "voids" of diffuse, high temperature stellar wind gas at the centers of the model H II regions. As a result, the ionized gas is confined to a thin shell between the wind bubble and the IF.

The location of the RPSW model in the BPT diagram is strikingly far from the locations of other models. Like the RPWW models, the RPSW models saturate at finite values of [N II]/Hα and [O III]/Hβ, regardless of how high the luminosity becomes. However, unlike in case RPWW, the saturation values are extraordinarily far down the sequence of one-zone models: [N II]/Hα > $10^{-0.5}$ and [O III]/Hβ < 10^0, corresponding to a one-zone value of $\mathcal{U}$ < $10^{-3.3}$. We can understand this effect by considering the relative importance of radiation and wind pressure in controlling the internal structures of H II regions. A value of $\log \Omega = 2$ requires that $P_{IF}V_{IF}/P_{in}V_{in} = 1.01$. Physically, this amounts to saying that the energy of the wind bubble constitutes 99% of the internal energy of the entire H II region. We note that V_{IF} is strictly greater than V_{in}. Similarly, P_{IF} is strictly greater than
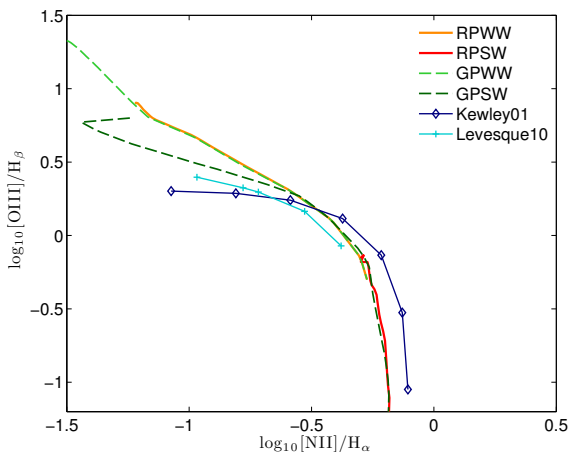
Figure 5.4 – A comparison of model results on the BPT diagram. All results shown are for $n_{\mathrm{H,in}} = 10 \text{ cm}^{-3}$ and a spectrum corresponding to a zero-age stellar population. The D00 model is marked as Kewley01 in the legend.

P_{in}, since the radiation force necessarily falls to zero at the IF, and thus pressure balance requires that gas pressure at the IF exceed that at the edge of the wind bubble. Thus models with $\log \Omega = 2$ necessarily have both $V_{\mathrm{IF}} \approx V_{\mathrm{in}}$ and $P_{\mathrm{IF}} \approx P_{\mathrm{in}}$. This corresponds to the H II region being a thin shell of nearly constant gas pressure. Figure 5.3 shows an example of this uniform density.

The RPSW configuration clearly cannot have radiation pressure as a significant force. If the radiation pressure force were significant, then we could not have $P_{\mathrm{IF}} \approx P_{\mathrm{in}}$, since the pressure at the IF would be pure gas pressure, and this would have to balance the gas plus radiation pressure at the inner edge. The conclusion of this analysis is that it is not possible to construct a physically consistent model in which wind pressure and radiation pressure are both strong in the dimensionless sense. Indeed, our model grids reflect this fact in that there are no models with radiation pressure turned on that are simultaneously dominated by wind ($\Omega \gg 1$) and dominated by radiation pressure ($\Psi \ll 1$). This physical effect manifests in the BPT diagram as a saturation in the range of line ratios that the RPSW models are able to reach. As discussed above, the location of an H II region driven by a stellar source in the BPT diagram is effectively controlled by $\mathcal{U}$, the photon to baryon ratio. However, $\mathcal{U}$ may also be thought of as a measure of the importance of radiation pressure, since increasing the photon number density relative to the baryon density also increases the radiation pressure relative to gas pressure. The fact that RPSW models cannot reach small values of Ψ also means that they cannot reach large values of $\mathcal{U}$, and thus cannot reach the line ratios associated with large $\mathcal{U}$. YM12 used this point to derive upper limits on the wind energy budget within individual H II regions and entire galaxies.

In contrast, radiation pressure is completely neglected in GPSW models. As there are no other forces to balance gas pressure gradients, these models have $P_{\mathrm{IF}} = P_{\mathrm{in}}$ indepen-

dent of the luminosity, and thus a value of $\log \Omega = 2$ simply implies that the shell is very thin: $R_{\mathrm{IF}} = 1.003\, R_{\mathrm{in}}$. In these models one can achieve arbitrarily high $\mathcal{U}$ by raising the luminosity and increasing R_{in} to keep up with R_{IF}. Figure 5.3 shows an example of such a model. Thus the GPSW models are not restricted in the range of $\mathcal{U}$ they can represent. However, the comparison with the RPSW models shows that GPSW models at high $\mathcal{U}$ are unphysical, because radiation force would have compressed the gas and limited $\mathcal{U}$ in a real region.

The comparison between RPSW, GPSW, and one-zone models shown in Figure 5.2 also reflects these effects. Both RPSW and GPSW models are wind-dominated and therefore have nearly uniform densities, and thus can be reasonably-well represented by one-zone models, leaving aside the issues of radiation field hardening and non-uniform temperature discussed in Section 5.3.2.1. Thus both RPSW and GPSW models follow the one-zone sequence reasonably closely. They differ only in the range of $\mathcal{U}$ values within that sequence that they are able to sample.

5.4   Comparison to previous work

It is interesting to revisit earlier published models for H II region line ratios in the context of our exploration of how these line ratios respond to changes in the included physics. We have chosen our model parameters in Starburst99 and Cloudy to be as close as possible to those used by D00 in order to facilitate this comparison. In Figure 5.4, we compare our four model results with the results computed by D00 and L10, at the same age of ionizing star cluster (0 Myr) and same density $n_{\mathrm{H,in}} = 10\ \mathrm{cm}^{-3}$.

The D00 model, which did not include radiation pressure and adopted plane-parallel ionized gas slabs at a fixed density, is essentially a wind-dominated model. This is because a plane-parallel slab can be thought of as a thin shell of material at roughly fixed distance from the ionizing source, and the only way to create a thin shell of constant gas pressure is to confine it with hot gas. Therefore our closest model to the D00 model is GPSW, and indeed we find that our GPSW results agree with the D00 model fairly well. Differences in line ratios between D00 and GPSW are around 0.1 to 0.2 dex. Our model sequence extends somewhat further, but this is simply a result of our having used a slightly larger range of input luminosities. The agreement between the models confirms that our Cloudy calculations, with input parameters set very close to the D00 settings, can reasonably well reproduce the earlier results. However, we note the comparison shows that the D00 models are not physically realistic at high luminosity, because one cannot neglect radiation pressure in very bright H II regions. Radiation pressure limits the physical range of $\mathcal{U}$, particularly for wind-confined slabs, and models without radiation pressure such as those of D00 do not properly capture this effect.

The models from L10 are similar to those of D00 in that they are based on plane-parallel ionized gas slabs, but the L10 models include radiation pressure. Therefore when $\mathcal{U}$ is low, the regions must be confined by wind pressure (like our RPSW). On the other hand, when $\mathcal{U}$ is high, the L10 models should be confined by radiation pressure (like our RPWW). However, Figure 5.4 shows that overall L10's models closely track our

GPSW curve (maximum separation < 0.1 dex). In light of our results, we can see that the L10 models, while not physically inconsistent, do represent a rather odd cut through parameter space. There are *two* structural parameters describing H II regions, and the L10 models sample a one-dimensional path through this two-dimensional space. Along this path the ratio of wind pressure to radiation pressure varies systematically from large values ($\Omega \gg 1$, $\Psi \gg 1$) at low ionization parameter to small values ($\Omega \ll 1$, $\Psi \ll 1$) at high ionization parameter. There is no obvious physical reason such a systematic variation in wind to radiation pressure strength should occur, particularly since the ratio of stellar wind momentum flux to luminosity is roughly the same for all O stars (Repolust et al. 2004).

5.5   Conclusions

We have computed a grid of quasi-static H II region models using Starburst 99 and Cloudy that covers a large range of density, luminosity, and stellar population age. In order to understand how radiation pressure and stellar winds alter H II regions' internal structures and observable line emission, we run two sets of models, one with radiation pressure enabled and one with it disabled, and we vary the radius at which the inner, wind-dominated bubble ends and the photoionized region begins. In the manner, we construct four sets of model H II regions: (1) ones with radiation pressure and weak stellar winds (RPWW), (2) wind bubbles that also include radiation pressure (RPSW), (3) Strömgren spheres where radiation pressure is ignored and winds are weak (GPWW), and (4) wind-dominated bubbles where radiation pressure is disabled (GPSW). We then explore how each set of H II regions populates the BPT diagram.

Our models reveal a number of interesting effects. All models form a sequence that runs from the lower right corner of the BPT diagram (high [N II]/Hα, low [O III]/Hβ) to the upper left corner (low [N II]/Hα, high [O III]/Hβ), with the position of an H II region along the sequence dictated by its luminosity, or equivalently its effective ionization parameter $\mathcal{U}$. However, the range of $\mathcal{U}$ explored by the models is limited when radiation pressure is included. Because strong radiation pressure, which would produce high $\mathcal{U}$, also causes gas to pile into a dense shell, the characteristic value of $\mathcal{U}$ within the shell is limited at a finite value. (See YM12 for more detail.) As a consequence, models which neglect radiation pressure can reflect an arbitrarily high value of $\mathcal{U}$, which real regions cannot.

The interaction of winds with radiation pressure further enhances this effect. We show that a stellar wind-dominated region cannot also have strong radiation pressure while remaining in hydrostatic balance, and as a result the range of $\mathcal{U}$ is severely limited. This means that wind-dominated H II regions can never occupy the upper-left portion of the BPT diagram, and, conversely, those H II regions that are observed to lie in this region must either have negligible wind pressure, be far from pressure balance, or be kept in pressure balance by forces other than gas and radiation pressure (e.g. strong magnetic pressure; YM12). The most realistic option, and the one favored by direct observations of nearby H II regions (Harper-Clark & Murray 2009, Lopez et al. 2011) as well as mid-infrared line ratios (YM12) is the first one: wind pressure is not dynamically significant,

at least for bright H II regions. Further, the fact that the high-redshift galaxy population has characteristically high ionization parameters implies that radiation pressure is significant within these galaxies' ionized zones, in an ionization-weighted sense.

We have compared our results to the earlier models of Dopita et al. (2000, D00) and Levesque et al. (2010, L10). In these models the H II region is assumed to be a wind-dominated thin ionized shell, which corresponds to our GPSW model. We find that this model agrees well with the results of D00 and L10. However, we show that these models are inconsistent at the high luminosity end. The D00 models neglect radiation pressure for H II regions where it is non-negligible. The L10 models include radiation pressure, but we show that the assumed plane-parallel slab geometry is physically realistic only if the strength of the ratio of stellar wind pressure to radiation pressure varies systematically with H II region properties in a physically unexpected manner.

While these calculations provide insight into how the physics driving H II regions' structures translates into observable properties such as line ratios, a full model for where galaxies fall in the BPT diagram requires attention to H II regions' dynamical expansion as well as their internal structure. This problem is the subject of Paper II.

VI

Line emission from radiation-pressurized H II regions. II. Dynamics and population synthesis

Optical and infrared emission lines from H II regions are an important diagnostic used to study galaxies, but interpretation of these lines requires significant modeling of both the internal structure and dynamical evolution of the emitting regions. Most of the models in common use today assume that H II region dynamics are dominated by the expansion of stellar wind bubbles, and have neglected the contribution of radiation pressure to the dynamics, and in some cases also to the internal structure. However, recent observations of nearby galaxies suggest that neither assumption is justified, motivating us to revisit the question of how H II region line emission depends on the physics of winds and radiation pressure. In a companion paper we construct models of single H II regions including and excluding radiation pressure and winds, and in this paper we describe a population synthesis code that uses these models to simulate galactic collections of H II regions with varying physical parameters. We show that the choice of physical parameters has significant effects on galactic emission line ratios, and that in some cases the line ratios can exceed previously claimed theoretical limits. Our results suggest that the recently-reported offset in line ratio values between high-redshift star-forming galaxies and those in the local universe may be partially explained by the presence of large numbers of radiation pressured-dominated H II regions within them.

Silvia Verdolini, Sherry C. C. Yeh, Mark R. Krumholz, Christopher D. Matzner, Alexander G. G. M. Tielens

6.1 Introduction

Ratios of optical and infrared lines from H II regions are popular diagnostics that have been used to infer a large number of properties of galaxies. Perhaps the most famous example of this is the Baldwin et al. (1981) diagram (hereafter the BPT diagram), which plots [O III] $\lambda5007$/Hβ versus [N II] $\lambda6584$/Hα. H II regions in the local universe form a narrow sequence in this diagram, and their position along this sequence provides information about properties of the H II region such as its density and metallicity. Recently, thanks to the Sloan Digital Sky Survey (SDSS) (Brinchmann et al. 2004, Tremonti et al. 2004) the sequence has been extended to unresolved galaxies in the local universe. The SDSS showed that galaxies whose line emission is dominated by an active galactic nucleus (AGN) or by fast shocks are distinguishable in the BPT diagram from those whose emission is powered predominantly by star formation. Star-forming galaxies and H II regions in the local universe follow the same sequence, suggesting that star forming galaxies can be simplified as a collection of H II regions. In contrast, AGN-dominated galaxies lie off this sequence.

However, star-forming galaxies at high redshift appear to be offset (upward and to the right) in the BPT diagram from those in the local universe (Shapley et al. 2005, Liu et al. 2008, Erb et al. 2006a, 2010), but do not occupy the same locus as local AGN-dominated galaxies either. Several possible causes for the offset have been suggested. One possibility is that H II regions at $z \approx 2$ follow the same star-forming sequence as in the local universe, but the presence of an unresolved AGN or shocked gas contaminates their line emission causing the shift in the BPT diagram (e.g., Liu et al. 2008). Observational support for this idea comes from Wright et al. (2010), who demonstrate using integral field spectroscopy that a weak AGN is responsible for the shift of a $z = 1.6$ galaxy. Trump et al. (2011) stack HST grism data from many galaxies to show that this phenomenon is reasonably common. However, another possible explanation for the offset is that there are systematic differences exists between H II regions in the local universe and at high redshift. This suggests that the time is ripe for a reinvestigation of the physics driving H II region line emission, and thus the location of galaxies in diagnostic line ratio diagrams such as the BPT plot.

The problem of computing the integrated line emission produced by a galaxy containing many H II regions can be roughly decomposed into two separate steps. The first is determining the internal structure of an H II region given its large-scale properties, for example the radius of the ionization front and the luminosity of the star cluster that powers it. The second is determining the dynamics of the H II region population in a galaxy, which sets the distribution of H II region properties. The first of these problems is generally solved with by a radiative transfer and chemical equilibrium code such as Cloudy (Ferland et al. 1998) or MAPPINGS (Sutherland & Dopita 1993, Dopita et al. 2000, Kewley et al. 2001), while the second is solved by a population synthesis code that generates a population of H II regions and follows their expansion in the interstellar medium (e.g. Dopita et al. 2006a). For this second step, the results depend on what drives H II region expansion, i.e. whether H II regions are classical Strömgren spheres whose expansion is driven by warm gas pressure (Spitzer 1978), wind bubbles whose expansion is controlled

by the pressure of shocked stellar wind gas (Castor et al. 1975, Weaver et al. 1977), radiation pressure-driven shells (Krumholz & Matzner 2009, Murray et al. 2010), or something else.

The most commonly-used population synthesis models, those of Dopita et al. (2000, 2005, 2006b,a) and Groves et al. (2008), assume that the expansion of H ɪɪ regions is primarily wind-driven. However, recent resolved observations of H ɪɪ regions in nearby galaxies have shown that this assumption is likely to be incorrect. Harper-Clark & Murray (2009) and Lopez et al. (2011) use X-ray observations of Carina and 30 Doradus, respectively, to directly estimate the pressure of the shocked hot gas inside expanding H ɪɪ regions.[1] By comparing these pressures to the other sources of pressure driving the expansion, and to the values expected for a wind bubble solution, they conclude that the giant H ɪɪ regions cannot be expanding primarily due to shocked wind gas pressure, and that radiation pressure may well be dominant. Moreover, Yeh & Matzner (2012) found no evidence for wind-dominated bubbles either in individual regions or on galactic scales, using observed ionization parameters. Physically, the surprisingly weak role of winds is likely a result of H ɪɪ regions being "leaky", so that the hot gas either physically escapes, or it mixes with cooler gas, and this mixing cools it enough for radiative losses to become efficient (Townsley et al. 2003). Regardless of the underlying cause, though, the observations clearly show that the wind bubble model should be reconsidered.

In this work, we investigate the implications of these observations, and more broadly of varying the physics governing H ɪɪ regions expansion, for line emission and line ratio diagnostics. To do so we create a population synthesis model in the spirit of Dopita's work, and within this model we systematically add and remove the effects of radiation pressure, and we vary the stellar wind strength. In a companion paper (Chapter 5, hereafter Paper I) we generate a series of hydrostatic equilibrium models of H ɪɪ regions using Starburst99 (Leitherer et al. 1999) and Cloudy (Ferland et al. 1998), both including and excluding radiation pressure and stellar winds. In this paper we use these models to predict the integrated line emission of galaxies containing many H ɪɪ regions.

The structure of the remainder of this paper is as follows. In Section 6.2 we describe the method we implement to generate synthetic galaxies. In Section 6.3 we analyze the main results, with particular attention to how various physical mechanisms affect observed line ratios, and in Section 6.4 we compare to observations. We finish with discussion and conclusions in Section 6.5.

6.2   Method

We are interested in the computing the total line emission of multiple H ɪɪ regions in an unresolved galaxy, such those at high redshift, in order to create a synthetic set of data

---

[1] Note that Pellegrini et al. (2011) analyze the same region (30 Doradus) as Lopez et al. (2011) and report a much higher pressure in the X-ray emitting gas, such that this pressure exceeds radiation pressure. They reach this result by adopting a small filling factor for the X-ray emitting gas, compared to Lopez et al.'s assumption of a filling factor close to unity. However, with such a small filling factor, the hot gas is not dynamically important for the H ɪɪ region as a whole, and thus the general conclusion that hot gas is dynamically unimportant remains true even if Pellegrini et al.'s preferred filling factor is correct.

Table 6.1 – Static H II region Models

Model	P_{rad}	$\log \Omega$
RPWW (Radiation Pressure Weak Winds)	yes	−1.5
RPSW (Radiation Pressure Strong Winds)	yes	2
GPWW (Gas Pressure Weak Winds)	no	−1.5
GPSW (Gas Pressure Strong Winds)	no	2

that is directly comparable with observed galaxies in the BPT diagram or similar line ratio diagrams. The procedure consists of two parts. First, we create synthetic line emission predictions for a variety of single H II regions over a large grid in stellar luminosity, radius, and age. We describe this procedure in detail in Paper I, but for convenience we briefly summarize it below. Second, we build a population synthesis code that creates, evolves and destroys H II regions, and computes the summed line emission.

6.2.1 Spectral synthesis and photoionization models

We create a population of static, single H II regions, with a wide range of sizes and ionizing luminosities. To do so we use Starburst99 (Leitherer et al. 1999) to generate ionizing continua from coeval star clusters of different ages. We feed the synthetic spectra into Cloudy 08.00, last described by Ferland et al. (1998), as the ionizing continuum emitted at the center of each simulated H II region. Each H II region is spherical and in perfect force balance. We adopt Cloudy's default solar abundances and ISM dust grain size distributions, and the same gas phase abundances as Dopita et al. (2000). We compute a grid of models covering a wide range in density, from $\log n_{\mathrm{H,in}} = -1$ to 5, where $n_{\mathrm{H,in}}$ is the number density of hydrogen nuclei at the inner boundary of each H II region. Each set of the simulations outputs the integrated luminosity of selected optical emission lines, including Hα, Hβ, [O III], and [N II], i.e. the lines that enter the BPT diagram. For more details we refer readers to Paper I.

We compute four sets of static H II region models, corresponding to four combinations of radiation pressure (P_{rad}) and stellar wind strength (Table 6.1). In the models with P_{rad}, radiation pressure is allowed to exceed ionized gas pressure, in contrast to Cloudy's default setting. For models where radiation pressure is absent, the outward force due to the incident radiation field is turned off. We parameterize the strength of the stellar wind by Ω, which is defined as

$$\Omega \equiv \frac{P_{\mathrm{in}} V_{\mathrm{in}}}{P_{\mathrm{IF}} V_{\mathrm{IF}} - P_{\mathrm{in}} V_{\mathrm{in}}}, \tag{6.1}$$

where $P_{\mathrm{IF}} V_{\mathrm{IF}} - P_{\mathrm{in}} V_{\mathrm{in}}$ is the difference of the product of gas pressure and volume between the ionization front ($P_{\mathrm{IF}} V_{\mathrm{IF}}$) and the inner edge of the H II region ($P_{\mathrm{in}} V_{\mathrm{in}}$), which is the outer edge of a hot, wind-pressurized bubble. Ω is the same wind parameter defined in Yeh & Matzner (2012), and we refer readers to Table 1 and Section 4.1 in that paper for detailed discussion of its meaning. However, an intuitive explanation of Ω is that it measures the relative energy content of the hot stellar wind gas and the warm photoionized

Table 6.2 – Fiducial parameters

Parameter	Value
$M_{a,\mathrm{min}}$	20 M$_\odot$
$M_{a,\mathrm{max}}$	5×10^9 M$_\odot$
k_ρ	1
$\mathcal{M}$	30
P_{amb}/k_B	10^4 K cm^{-3}
SFR	1 M$_\odot$ yr^{-1}
P_{rad}	yes
f_{trap}	2
ϕ	0.73
ψ	3.2

gas; high values of Ω correspond to wind-dominated H II regions, while low values to ones where winds are dynamically unimportant.

6.2.2 Population synthesis code

We treat a galaxy as a collection of H II regions only, with no contribution to line emission from other sources (e.g. stars or warm ionized medium). We generate, evolve, and destroy these H II regions using a population synthesis code derived from the GMCEVOL code described in Krumholz et al. (2006) and Goldbaum et al. (2011). In our models, we characterize a galaxy by two parameters: a (constant) star formation rate (SFR) and a mean ambient pressure P_{amb}, and we give fiducial values of these parameters in Table 6.2, though below we explore how our results depend on these choices. For all the results described in this paper, we run our simulation code for 200 Myr, and write output every 1 Myr. We describe each step the code takes below.

Creation - To create H II regions, we pick a series of stellar association masses M_a from a probability distribution

$$p(M_a) \propto M_a^{-2} \qquad (6.2)$$

in the range $M_{a,\mathrm{min}}$ to $M_{a,\mathrm{max}}$ (Williams & McKee 1997). We give fiducial values of the minimum and maximum masses in Table 6.2, but experimentation shows that these choices have almost no effect on our final result. Each association appears at a time dictated by the SFR; for example, if the first three associations drawn in a calculation have masses of 10^5 M$_\odot$, 10^6 M$_\odot$, and 10^7 M$_\odot$, and the SFR is 1 M$_\odot$ yr^{-1}, the first association turns on at 0.1 Myr into the simulation, the second at 1.1 Myr, and the third at 11.1 Myr. When an association turns on, we pick stars from a Kroupa (2001) IMF until we have enough stellar mass to add up to the association mass. For computational convenience we discard stars with masses below 5 M$_\odot$, since these contribute negligibly to the ionizing luminosity. For the stars we retain, we use the fits of Parravano et al. (2003)

to assign an ionizing luminosity and a main sequence lifetime. Each association becomes the power source for a new H II region, with an ionizing luminosity determined by the sum of the ionizing luminosities of the constituent stars. Note that we account for aging of the stellar population in the ionizing spectrum, but use step-function approximations for the luminosity, ionizing luminosity and wind trapping factor in our dynamical calculations. These we take to be constant during the ionizing lifetime of each cluster.

Expansion - The neutral gas in which each H II region expands has a radial density profile $\rho = \rho_0(r/r_0)^{-k_\rho}$, and our code allows $k_\rho = 0$ or 1. As we discuss in Section 6.3.3, this choice proves to make very little difference, so unless stated otherwise we simply adopt $k_\rho = 1$. We determine the mean values of ρ_0 and r_0 from two constraints, one related to the pressure of the galaxy and a second from the mass of the association. Specifically, we require that

$$M_a = [4\pi/(3 - k_\rho)]\bar{\rho}_0 \bar{r}_0^3 \tag{6.3}$$
$$P_{\text{amb}} = 2\pi G \, (\bar{\rho}_0 \bar{r}_0)^2 \; . \tag{6.4}$$

The first of these equations is equivalent to the statement that the mass of the association is comparable to the mass of the surrounding gas (i.e. that the star formation efficiency in the vicinity of an association is $\sim 50\%$), while the second is equivalent to the statement that the gas around an association is in approximate pressure balance with the mean pressure of the galaxy. These two statements uniquely determine $\bar{\rho}_0 \bar{r}_0$, but we add a random scatter on top of this to represent the expected density variation present in a turbulent medium. Such media have density distributions well-described by lognormal distributions (e.g. Padoan & Nordlund 2002). We therefore scale our value of ρ_0 by a factor x drawn from the distribution

$$p(x) = \frac{1}{\sqrt{2\pi\sigma_x^2}} \exp\left[-\frac{\left(\ln x - \overline{\ln x}\right)^2}{2\sigma_x^2}\right], \tag{6.5}$$

where $\overline{\ln x} = \sigma_x^2/2$, the dispersion of pressures is $\sigma_x = \sqrt{\ln(1 + \mathcal{M}^2/4)}$, and $\mathcal{M}$ is the Mach number that characterizes the turbulence. Thus the final value of $\rho_0 r_0$ we adopt for a given H II region is $\bar{\rho}_0 \bar{r}_0 x$, with $\bar{\rho}_0 \bar{r}_0$ determined by the solution to Equations (6.3) and (6.4), and x chosen from the distribution given by Equation (6.5). We adopt a fiducial Mach number $\mathcal{M} = 30$, appropriate for giant molecular clouds in nearby galaxies, but we have experimented with values up to $\mathcal{M} = 300$, appropriate for ultra luminous infrared galaxies (see Krumholz & Thompson 2007 for more detailed discussion). We find that the choice of $\mathcal{M}$ makes little difference to the final result.

Once we have the density distribution around an H II region, we can compute its expansion. We do so in two possible ways. The first is simply following the classical Spitzer (1978) similarity solution for gas pressure-driven expansion, generalized to our density profile. The second is using the Krumholz & Matzner (2009) generalization of this solution to the case where radiation pressure is dynamically significant. For this case, we use the approximate solution given by Equation (13) of Krumholz & Matzner. This solution involves a few free parameters, and the values we adopt are summarized in Table

6.2. The most important of these is f_{trap}, which represents the factor by which trapping of photons and wind energy within the expanding dust shell amplifies the radiation pressure force. We adopt a relatively low value $f_{\text{trap}} = 2$ as a fiducial value, based in part on recent simulations indicating the radiative trapping is likely to be very inefficient (Krumholz & Thompson 2012, 2013), but we also explore different values of f_{trap} below. Note that in the case $f_{\text{trap}} = 0$, the Krumholz & Matzner (2009) solution reduces to the classical Spitzer (1978) one. We discuss the remaining free parameters below. Finally, note that we do not consider the case of expansion following a Weaver et al. (1977) wind bubble solution, both because Dopita et al. (2006a) have already obtained results in this case, and because the observations discussed in the Introduction suggest that this model is unlikely to be correct.

Stalling - We stop the expansion of an H II region if its internal pressure ever falls to the pressure of the ambient medium (P_{amb}). We can express the internal pressure as the sum of the thermal pressure of the ionized gas and the radiation pressure. The thermal pressure of the ionized gas P_{gas} is

$$P_{\text{gas}} = \mu_{\text{H}} n_{\text{II}} m_{\text{H}} c_{\text{II}}^2 , \tag{6.6}$$

where n_{II} is the number density of hydrogen nuclei in the H II region, $c_{\text{II}} = 9.74$ km s^{-1} is the sound speed, $\mu_{\text{H}} = 1/X = 1.33$ is the mean mass per H nucleus in units of amu, and $X = 0.75$ is the hydrogen mass fraction. We derive n_{II} from photoionization balance, which requires that

$$\phi S = \frac{4}{3}\pi r^3 \alpha_B n_{\text{II}} n_e = \frac{4}{3}\pi r^3 \alpha_B \left(1 + \frac{Y}{4X}\right) n_{\text{II}}^2 , \tag{6.7}$$

where S is the number of ionizing photons per second injected into the region, n_{H} is the number density of H nuclei, n_e is the number density of electrons and α_B is the case-B recombination coefficient. The factor $1 + Y/4X = 1.1$ (assuming helium mass fraction $Y = 0.23$, and that He is singly ionized) accounts for the fact that there are electrons from He as well as from H, and the factor of $\phi = 0.73$ accounts for ionizing photons that are absorbed by dust instead of hydrogen. Thus we have

$$n_{\text{II}} = \sqrt{\frac{3\phi S}{4\pi r^3 \alpha_B (1 + \frac{Y}{4X})}}. \tag{6.8}$$

Note that this expression implicitly assumes that the density within the H II region is constant, which is not the case if radiation pressure exceeds gas pressure. However, in this case the gas pressure is non-dominant, so it matters little if we make an error in computing it. The radiation pressure P_{rad} is

$$P_{\text{rad}} = \frac{\psi S \epsilon_0 f_{\text{trap}}}{4\pi r^2 c} , \tag{6.9}$$

where $\psi = L/(S \epsilon_0)$ is the ratio of the star's bolometric power to its ionizing power counting only an energy $\epsilon_0 = 13.6$ eV per ionizing photon. We adopt $\psi = 3.2$ following Murray & Rahman (2010), Fall et al. (2010), and Lopez et al. (2011).
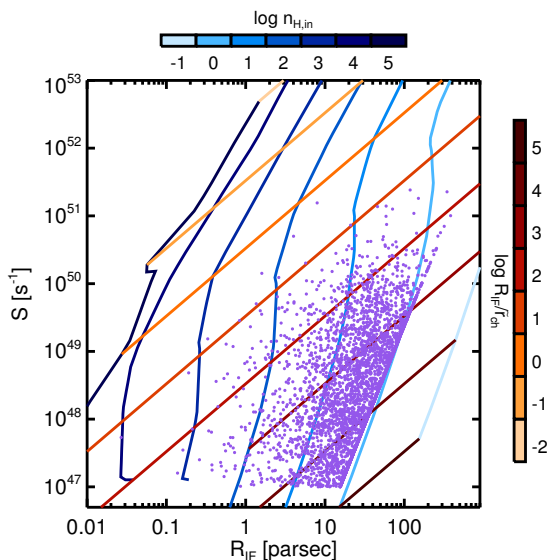
Figure 6.1 – Radius of the ionization front (R_{IF}) versus ionizing luminosity (S). Each data point represents a single H II region at one time step of one of our population synthesis calculations; the line against which points have accumulated on the right side of the plot is the stalling line (see Section 6.2.2). Colored lines indicate radii and ionizing luminosities of the H II regions in the RPWW model grid (see Section 6.2.1); note that only a subset of the models are shown in order to avoid clutter. Blue colors indicate models with constant density $\log n_{H,in}$, and red colors indicate models of constant $\log R_{IF}/\tilde{r}_{ch}$, where $\tilde{r}_{ch}$ is the characteristic radius at which radiation and gas pressure balance Yeh & Matzner (2012); note that $\tilde{r}_{ch}$ is a function of S alone, and does not depend on R_{IF}. The values of $\log n_{H,in}$ and $\log R_{IF}/\tilde{r}_{ch}$ are as indicated in the color bars.

Destruction - We remove an H II region from our calculation when the stars that provide half its total ionizing luminosity reach the end of their main sequence lifetimes. This may occur before or after stalling, depending on the ambient conditions.

6.2.3 Calculation of the line emission

The population synthesis code generates output files containing information about the H II regions present at each timestep. For each H II region, we keep track of the ionizing luminosity S of the driving stellar association, the radius R_{IF} of the ionization front, and the age t of the association. In order to assign line emission luminosities to each H II region, we perform a three-dimensional interpolation on R_{IF}, S, and t, using the tables of individual H II region models described in Section 6.2.1.

Figure 6.1 illustrates the procedure. The Figure shows the ionization front radii (R_{IF}) and ionizing luminosities (S) of all the H II regions present at a single time step in one of our population synthesis calculations, overlaid with a grid of models for single H II
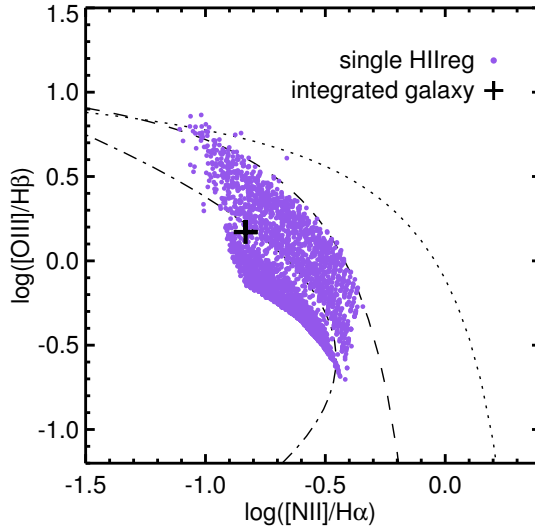
Figure 6.2 – Result of the interpolation plotted on the BPT plot for one snapshot of a simulated galaxy. The dashed line is the Kauffmann et al. (2003) line, an empirical separation of star forming galaxies and AGN based on the SDSS galaxies. The dotted line is the Kewley et al. (2001) theoretical limit for star forming galaxies. The dot-dashed line is a fit to the star forming galaxies from the SDSS galaxies Brinchmann et al. (2008). Each H II region is plotted with a dot (as in Figure 6.1) and the integrated galaxy is shown with the plus sign.

regions at an age of 0 Myr. The model grid is characterized by values of density $n_{\rm H,in}$ at the inner edge of the H II region and by the ratio of the ionization front radius to the characteristic radius $\tilde{r}_{\rm ch}$, defined by Yeh & Matzner (2012) as the value of $R_{\rm IF}$ for which gas pressure and unattenuated radiation pressure at the ionization front are equal. This radius is given by

$$\tilde{r}_{\rm ch} = \frac{\alpha_B L^2}{12\pi (2.2 k_B T_{\rm II} c)^2 S}, \tag{6.10}$$

where k_B is the Boltzmann constant, L is the bolometric luminosity, $T_{\rm II} = 7000$ K is the temperature of the ionized gas and the factor 2.2 is obtained by assuming that helium is singly ionized everywhere. Since $L = \psi S \epsilon_0$, the value of $\tilde{r}_{\rm ch}$ is simply proportional to S. For the simplest case of H II regions with an age of 0 Myr, we assign each one a luminosity in the [O III], [N II], Hα and Hβ lines by interpolating between the line luminosities of the nearest points in the overlaid model grid. The procedure for older H II regions is analogous, except that there is an additional interpolation in age. Once we have assigned a luminosity to each H II region, the total line luminosity of the galaxy is simply the sum over individual H II regions. Figure 6.2 shows the final result, where we have used the computed line ratios of both the individual H II regions from Figure 6.1 and the integrated galaxy to place them in the BPT diagram.

6.3   Results

Our aim is to investigate how radiation pressure and stellar winds affect galaxies' emission line ratios. As discussed above, the effects are both internal – changing the density distribution and thus the emission produced within single H II regions – and external – changing the distribution of H II region radii and other properties. It is easiest to understand the results if we tackle the internal effects separately first, which we do in Section 6.3.1. Then in Section 6.3.2 we consider external effects and how these interact with internal ones. In Section 6.3.3 we consider how the results depend on the properties of the galaxy as a whole (e.g. star formation rate, ambient pressure).

6.3.1   Internal effects of radiation pressure and winds

We first examine how our four internal structure models from Table 6.1 distribute H II regions in the BPT diagram.

6.3.1.1   Models with weak winds

We compare the two models with weak winds, RPWW and GPWW, in Figure 6.3. We show H II region models with constant $\log n_{H,in}$ = -1 to 5 (blue) and with constant $\log R_{IF}/\tilde{r}_{ch}$ (red), where R_{IF} is the ionization front radius and $\tilde{r}_{ch}$ is the characteristic radius in Krumholz & Matzner (2009) at which radiation and gas pressure balance. The ratio $R_{IF}/\tilde{r}_{ch}$ is related to the ionization parameter, as discussed in Paper I. Within each column, we plot three stages of the evolution of the cluster: 0, 2 and 4 Myr (from top to bottom).

We confirm some trends that have been seen in the past (Dopita et al. 2000, 2006a, Kewley et al. 2001), such as the decrease of line ratios as the cluster ages and increase of the ionization parameter from bottom right to top left. We explore for the first time a large range of values for the density. We find that the higher the density the stronger the [N II] and [O III] emission, up to the point that the gas density exceeds $\sim 10^4$ cm^{-3}. Beyond this, the density in the H II region exceeds the critical densities of the [N II] and [O III] lines (6.6×10^4 cm^{-3} and 6.8×10^5 cm^{-3}, respectively) causing the line intensity to stop increasing. However, before this point is reached, in the highest density models the [O III] emission is large enough that the [O III]/Hβ ratio exceeds the upper limit for starburst models described by Kewley et al. (2001) (black dotted line in Figure 6.3).

We can understand why our models exceed the Kewley et al. (2001) limits as follows. Kewley et al. created a grid of photoionization models with fixed initial density $n_{H,in}$ = 350 cm^{-3} and strong stellar winds (i.e. assuming planar geometry), with a range of metallicities and ionization parameters, and without the effect of radiation pressure. They find that the line ratios in their model never exceed the limit indicated by the black dotted line in Figure 6.3. Our models exceed this limit because they reach regimes of very high density and very high radiation field that the Kewley et al. models, due to their assumption of a fixed density and planar geometry, are unable to access. The underlying physical processes become clear if we compare our various models. Both models GPWW
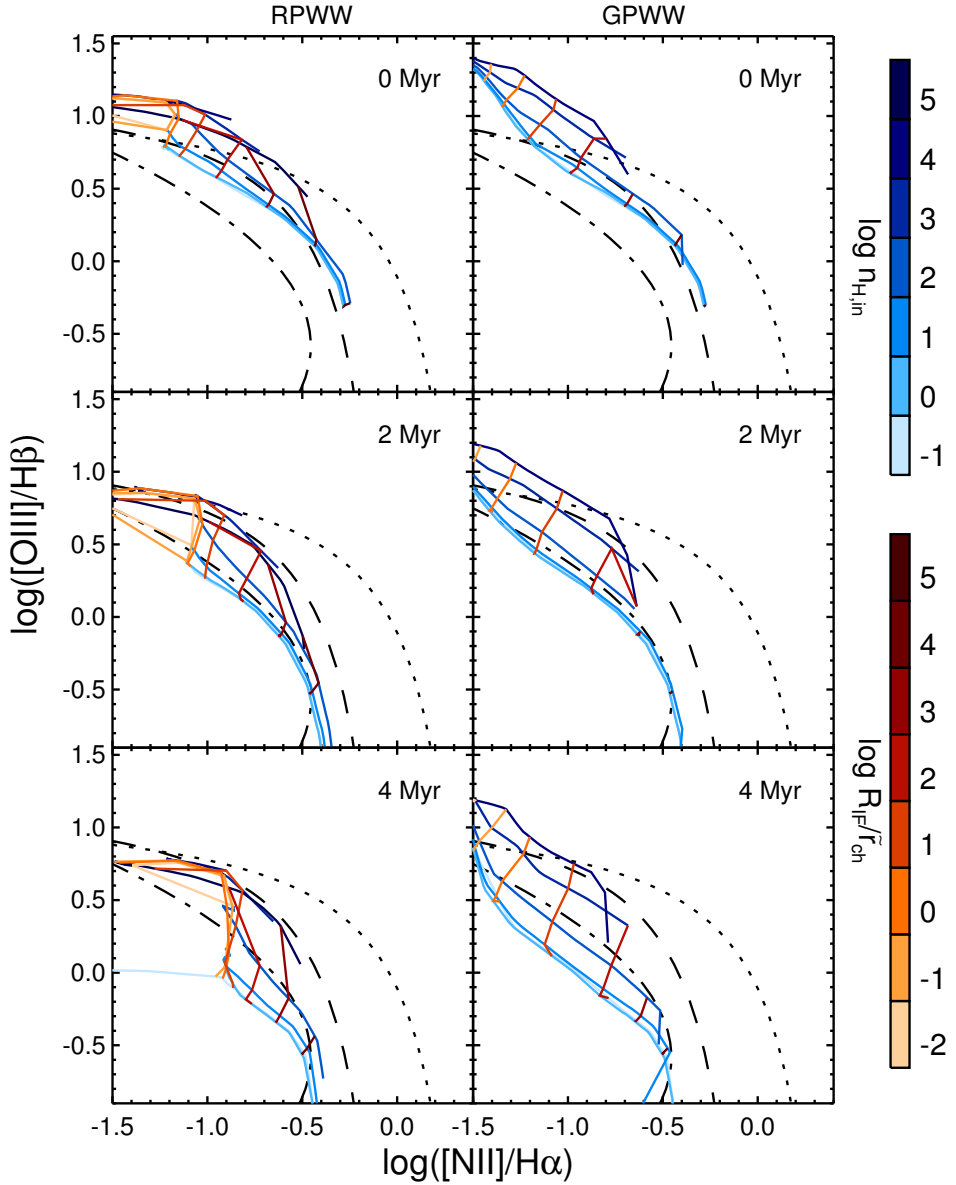
Figure 6.3 – BPT diagram for the models with weak winds evolving from 0 to 4 Myr (from top to bottom). The left column shows Model RPWW (with radiation pressure) and the right column shows Model GPWW (without radiation pressure). The models are shown with lines of constant $\log n_{\mathrm{H,in}} = -1$ to 5 (blue) and constant $\log R_{\mathrm{IF}}/\tilde{r}_{\mathrm{ch}}$ (red), where R_{IF} is the ionization front radius and $\tilde{r}_{\mathrm{ch}}$ is the characteristic radius in Yeh & Matzner (2012) at which radiation and gas pressure balance.

and RPWW can exceed the Kewley et al. limit, while our strong wind models either do not exceed or barely exceed it (see Section 6.3.1.2). In model GPWW, the density of the gas near the ionizing source can remain unphysical high even when the luminosity is very high; as a result there is significant emission from high-density, highly-irradiated gas. By contrast, in model RPWW, strong radiation pressure pushes gas away from the ionizing source when the luminosity is high, which in turn reduces the amount of gas that is both dense and highly irradiated. This model still breaks the Kewley et al. limit, but by less than GPWW. When stellar winds are included, on the other hand, the wind pushes the gas away from the source, reducing the radiation flux it experiences. This strongly limits the amount of dense, highly-irradiated gas in both of our strong wind models, and in the Kewley et al. models. We therefore see that the Kewley et al. limit is not a limit imposed by the physics of H II regions in general; instead, it is driven by Kewley et al.'s assumptions about the structure of H II regions, and the limitations on density and ionizing luminosity that these assumptions imply.

Comparing the cases with and without radiation pressure, we see that models with radiation pressure often produce less [O III] emission that those without. This effect arises because H II regions with radiation pressure and that have $R_{\mathrm{IF}}/\tilde{r}_{\mathrm{ch}} \ll 1$ have most of their gas in a radiation-confined shell that has a steep density gradient. This should be compared to the mostly uniform density produced if one ignores radiation pressure (Draine 2011, Yeh & Matzner 2012; Paper I). The higher density in this shell means that the density in the bulk of the emitting gas can exceed the critical density for a line even when the mean density of the H II region is below this value. Hence, Model RPWW saturates at a lower value of [O III]/Hβ than model GPWW.

6.3.1.2 Models with strong winds

We show the BPT diagram locations of the strong stellar wind models, RPSW and GPSW, in Figure 6.4. The first thing that is evident from the Figure is that Model RPSW produces line ratios in the BPT diagram far from both the other models and from the locations of observed galaxies. The region of parameter space where the models are not physical within the context of RPSW corresponds to H II regions with large ionizing luminosities but small radii, and one can understand why Model RPSW avoids this region with a small thought experiment. A value of $\Omega = 100$ implies that $P_{\mathrm{IF}}V_{\mathrm{IF}}/P_{\mathrm{in}}V_{\mathrm{in}} - 1 \ll 1$ (see Equation 6.1), meaning that the shocked wind gas dominates the total energy budget. This in turn requires that $V_{\mathrm{IF}} \approx V_{\mathrm{in}}$ and $P_{\mathrm{IF}} \approx P_{\mathrm{in}}$, so that the wind bubble fills almost the entire volume of the H II region, leaving only a thin shell of photoionized gas, and the gas pressures are nearly identical at the inner and outer edges of this shell. However, if the ionizing luminosity is large enough (specifically if it is large enough so that $R_{\mathrm{IF}} < \tilde{r}_{\mathrm{ch}}$), this is impossible. As $S \to \infty$ the radiation pressure at the inner edge of the photoionized shell must greatly exceed the gas pressure, and the gas pressure P_{IF} at the outer edge of the H II region, where all of the radiation has been absorbed, must be equal to the *total* pressure at the inner edge, which is the sum of the small gas pressure P_{in} and the much larger radiation pressure. It therefore follows that at sufficiently large S one must have $P_{\mathrm{IF}}/P_{\mathrm{rad}} \gg 1$, giving $\Omega \ll 1$, a point also made by Yeh & Matzner (2012). Thus one

cannot simultaneously have arbitrarily large S, arbitrarily small R_{IF}, and $\Omega \gg 1$. This issue is discussed further in Paper I.

This problem does not affect Model GPSW, since in this model one ignores radiation pressure. These models thus represent wind-dominated H II regions, and are qualitatively similar to the models of Dopita et al. (2000) and Kewley et al. (2001). In Paper I, we show a comparison of these models with those of Dopita et al. (2000), and find a good match with their results.

6.3.2 Dynamical effects of radiation pressure

Having understood the effects of radiation pressure and winds on the internal structure of H II regions, we are now ready to study their dynamical effects.

6.3.2.1 Distribution of H II region radii

In the expansion of an H II region, the radiation pressure term contributes as an additional push towards a faster radial expansion. To study this effect we examine the distribution of H II region radii produced by our population synthesis code, and how it is influenced by radiation pressure. Figure 6.5 shows a scatter plot of the radius of the ionization front (R_{IF}) versus the ionizing photon luminosity (S) for all the H II regions present at one time step in two of our simulations, one with $P_{amb}/k_B = 10^4$ K cm^{-3} (left column) and one with $P_{amb}/k_B = 10^6$ K cm^{-3} (right column). We show three cases: $f_{trap} = 0$ is a model where radiation pressure does not affect the dynamics at all, $f_{trap} = 2$ is our fiducial case, and $f_{trap} = 50$ is a model where the radiation pressure is assumed to be strongly trapped within the H II region, and affects the dynamics much more strongly. The case $f_{trap} = 0$ corresponds to H II regions that follow the classical Spitzer (1978) solution, $f_{trap} = 2$ corresponds roughly to the value favored by the radiation-hydrodynamic simulations of Krumholz & Thompson (2012, 2013), while $f_{trap} = 50$ corresponds to the peak of the values adopted in the subgrid models of Hopkins et al. (2011), where radiation is assumed to build up inside H II regions and produce large forces. In each panel we also show with full lines the stalling radii, defined as the radii where the internal pressure of the H II region drops to P_{amb}. Each H II region, when is created, is assigned a value of S and has $R_{IF} = 0$. As time passes, the H II region evolves and moves horizontally in the R_{IF} versus S plane till it reaches this limiting line at the stall radius. Since P_{rad}/P_{gas} decreases as R_{IF} grows at fixed S, depending on the value of S and P_{amb}, this can happen when $P_{gas} \ll P_{rad}$, when $P_{gas} \gg P_{rad}$, or when $P_{gas} \simeq P_{rad}$. If the H II region stalls when the gas is dominated by radiation pressure, $P_{amb} \simeq P_{rad}$, and from Equation (6.9) we have $R_{IF} \propto S^{1/2}$; if stalling occurs when an H II region is dominated by gas pressure, then $P_{amb} \simeq P_{gas}$, and from Equation (6.6) we have $R_{IF} \propto S^{1/3}$. Figure 6.5 shows also these two dependencies as dotted and dashed lines respectively.

The Figure shows that radiation pressure has two distinct effects on the dynamics. First, H II regions with radiation pressure expand faster than classical ones, so that models are shifted to increasingly large values of R_{IF} as f_{trap} increases. The shift from $f_{trap} = 0$ to 2 is relatively modest, while the gap between $f_{trap} = 2$ and 50 is somewhat larger,
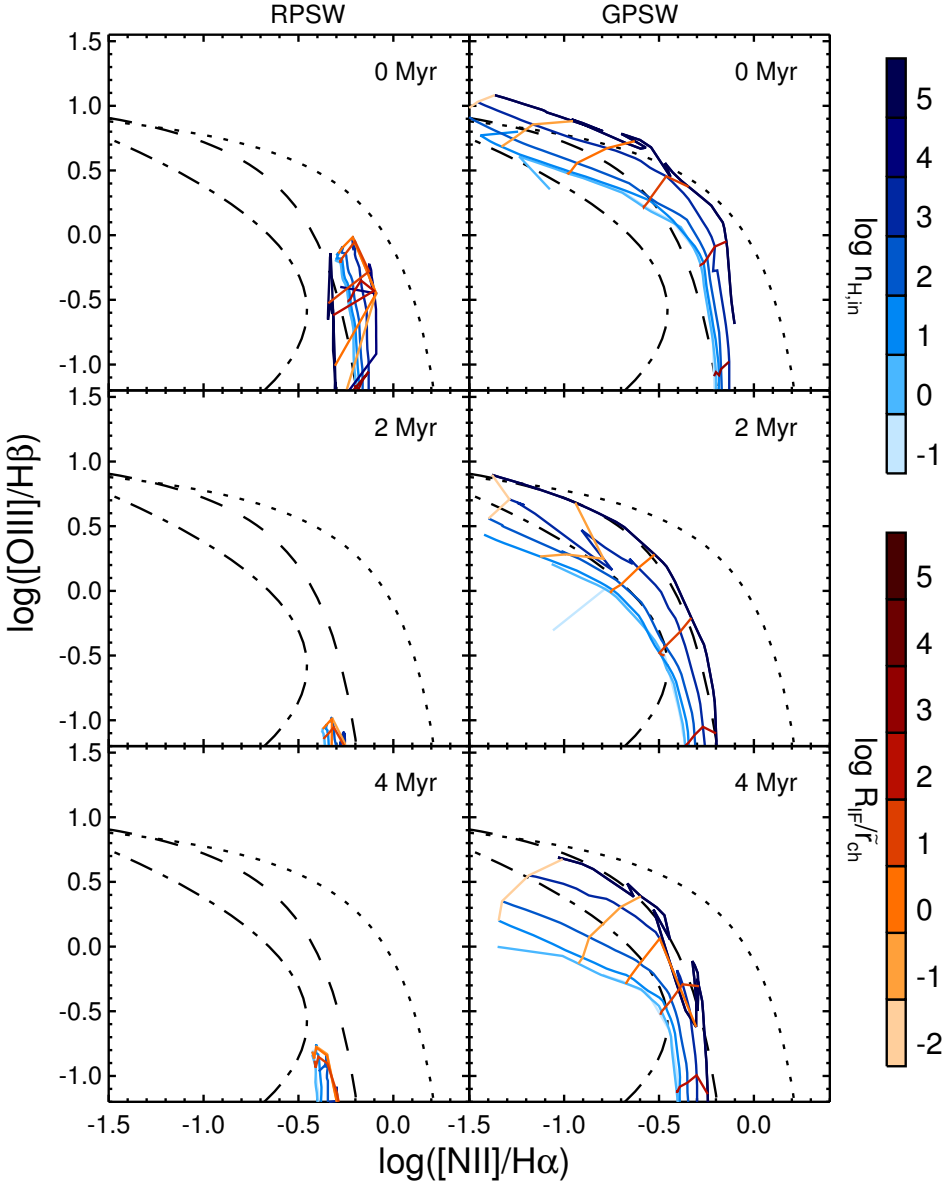
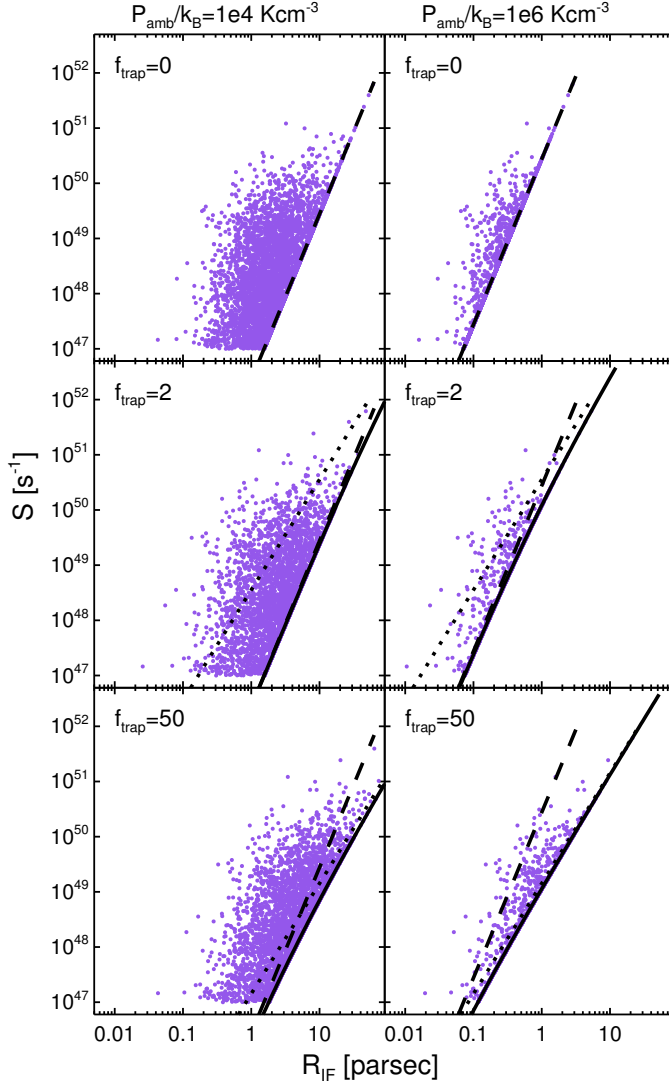Figure 6.4 – Same as Figure 6.3, but for the strong-wind Models GPSW and RPSW.

Figure 6.5 – Radius of the ionization front R_{IF} versus ionizing photon luminosity S for all the H II regions present at one time step in simulated galaxy (dots). We show simulations with two different values of P_{amb}/k_B (10^4 K cm^{-3} in the left column, and 10^6 K cm^{-3} in the right column), and three different values of f_{trap} (0 in the top row, 2 in the middle row, 50 in the bottom row). Black lines show the location of the stall radii for the simulations, with dashed lines corresponding to stalling when the pressure is gas-dominated, dotted lines to stalling when the pressure is radiation-dominated and full lines when to stalling when both radiation and gas pressure are relevant. The SFR is 1 $M_\odot$ yr^{-1} in all the simulations shown, so the number of H II regions present in each panel is approximately the same.
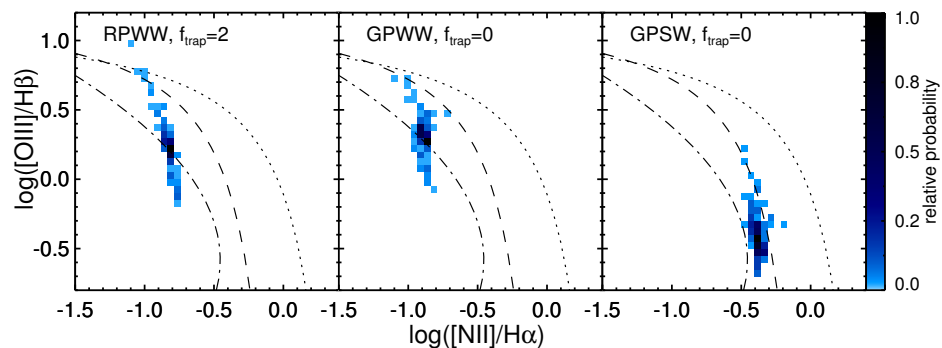
Figure 6.6 – Synthetic galaxies on the BPT diagram generated with our fiducial parameters and H II region modeling. Each model is a single time snapshot from our simulations, with the snapshots taken at intervals of 1 Myr. The region shown has been rasterized into pixels of $(0.05 \, \mathrm{dex})^2$. The color in each pixel corresponds to the number of models that fall into that pixel, normalized by the pixel containing the most models. The three cases shown are Model RPWW with $f_{\mathrm{trap}} = 2$, corresponding to H II regions with weak winds whose dynamics and internal structure include radiation pressure; Model GPWW with $f_{\mathrm{trap}} = 0$, corresponding to H II regions that are classical Strömgren spheres with neither radiation nor wind pressure affecting their internal structure or dynamics; and Model GPSW with $f_{\mathrm{trap}} = 0$, for which H II regions are wind-dominated bubbles without radiation pressure.

corresponding to nearly half a dex in radius. The second effect of radiation pressure is to increase the stalling radius. When the ambient pressure is small, this has a relatively small effect, because the stalling radius is large and most H II regions turn off before reaching it. One the other hand, when the pressure is high, the stalling radius is smaller and most H II regions stall before their driving stars evolve off the main sequence. In this case most H II regions are clustered up against the stalling radius, and the increase in stalling radius with f_{trap} has very significant effects.

6.3.2.2 Distribution of H II regions in the BPT diagram

We are now ready to use our population synthesis code to determine where simulated galaxies lie in the BPT diagram. We run three classes of models. The first, which we consider the most physically realistic given the observed properties of H II regions in the local Universe, uses Model RPWW for the internal structures of H II regions, and uses $f_{\mathrm{trap}} = 2$ to determine their dynamical evolution. The other two models use $f_{\mathrm{trap}} = 0$ (i.e. assume that H II regions expand as classical Spitzer H II regions), and use Models GPWW and GPSW for the internal structures. The latter choice is not fully consistent, in that with strong wind models we should use a wind-dominated dynamical solution such as that of Castor et al. (1975). We do not do so, however, both because Dopita et al. (2006a) have already explored this case, and because observations now strongly disfavor it.

Figure 6.6 shows the comparison of the three models on the BPT diagram for our
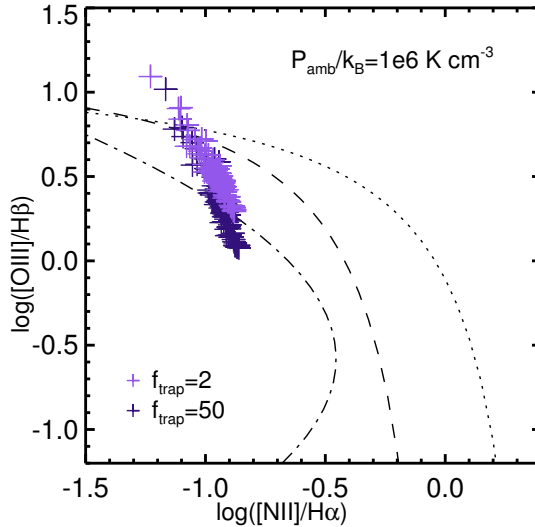
Figure 6.7 – Comparison of BPT diagrams for two runs with $P_{amb}/k_B = 10^6$ K cm^{-3} and $f_{trap} = 2$ and 50. Each plus sign represents a single time snapshot from our simulations, with the snapshots taken at intervals of 1 Myr. Both runs use Model RPWW, and are otherwise identical to the runs shown in Figure 6.6.

fiducial parameter choices (see Table 6.2). Each model represents the line ratio produced by summing the line emission over all the H II regions present in a simulated galaxy at a given snapshot in time, and for each model we show 200 such snapshots, separated by intervals of 1 Myr. The region shown in the plot has been rasterized into pixels of $(0.05$ dex$)^2$. The color in each pixel corresponds to the number of models that fall into that pixel, normalized by the pixel containing the most models. The plot shows several interesting results. Model GPSW, in which H II regions' internal structures are wind-dominated, are systematically shifted to lower [O III]/Hβ and higher [N II]/Hα than the weak wind models. Model RPWW spans a wide range of parameter space, including some snapshots that exceed the Kewley et al. (2001) theoretical limit. These snapshots tend to be immediately after the formation of a very large, bright, association. Model GPWW is covers a smaller range in the plot, and stays below the Kewley et al. (2001) limit.

We varied a number of the fiducial parameters, and found them to have little effect on the results. Parameters whose influence is negligible include $M_{a,min}$ and $M_{a,max}$, minimum and maximum value of the association mass, $\mathcal{M}$, the Mach number used to set the width of the density distribution, and k_ρ the powerlaw index that describes the density distribution into which H II regions expand. Perhaps surprisingly, the value of f_{trap} also has relatively little effect if we hold the internal models fixed, as illustrated in Figure 6.7. In other words, if we use Model RPWW to describe the internal structure of H II regions, the differences
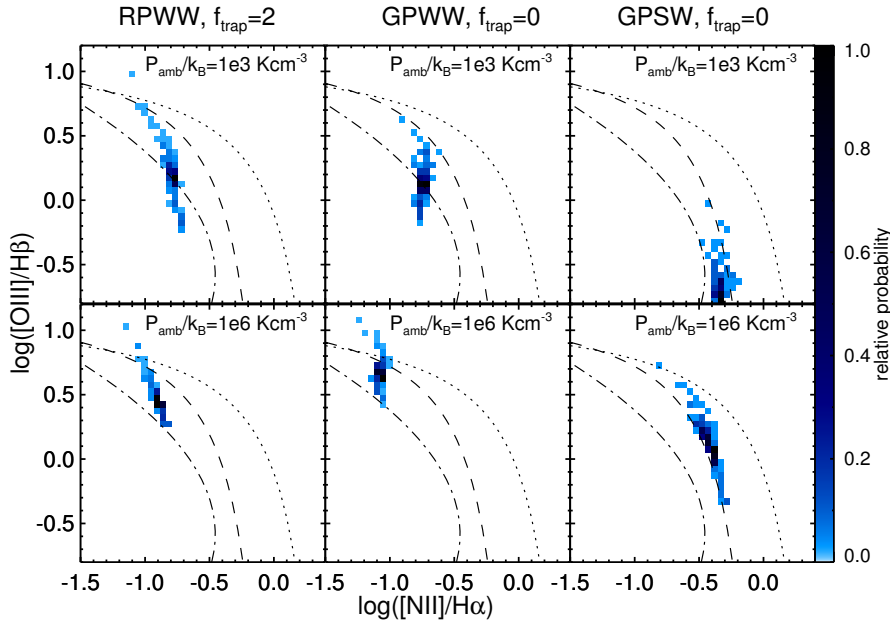
Figure 6.8 – Simulation results with varying P_{amb}. Models RPWW, GPWW, and GPSW are plotted respectively on the left, center and right column for $P_{\mathrm{amb}}/k_B = 10^3$ and 10^6 K cm^{-3} (top and bottom rows). The region shown has been rasterized into pixels of $(0.05 \text{ dex})^2$. The color in each pixel corresponds to the number of models that fall into that pixel, normalized by the pixel containing the most models. All other parameters are the same as in the fiducial case.

in the distributions of H II region radii visible in Figure 6.5 as we vary f_{trap} from 0 to 50 do not produce corresponding differences in the locations of the resulting galaxies in the BPT diagram – or at least the differences they produce are mostly within the scatter produced simply by stochastic drawing of association masses and surrounding densities. In Figure 6.1 we show the grid of models covering over 5 orders of magnitude both in R_{IF} and S. The grid dramatically shrinks in the BPT diagram (Figure 6.3) causing the small effect of f_{trap} in Figure 6.7. Thus there does not appear to be an obvious way to use line ratio observations of integrated galaxies to measure the value of the dynamical parameter f_{trap}. We stress, however, that f_{trap} includes the influence of wind pressure, and a wind-pressure dominated state can be identified, on the basis of line ratio observations, through its effect on the internal structures of H II regions. In particular, wind-dominated regions cannot access high values of the ionization parameter and are limited to the lower right of the BPT diagram; see Paper I and Yeh & Matzner (2012) for a thorough discussion.
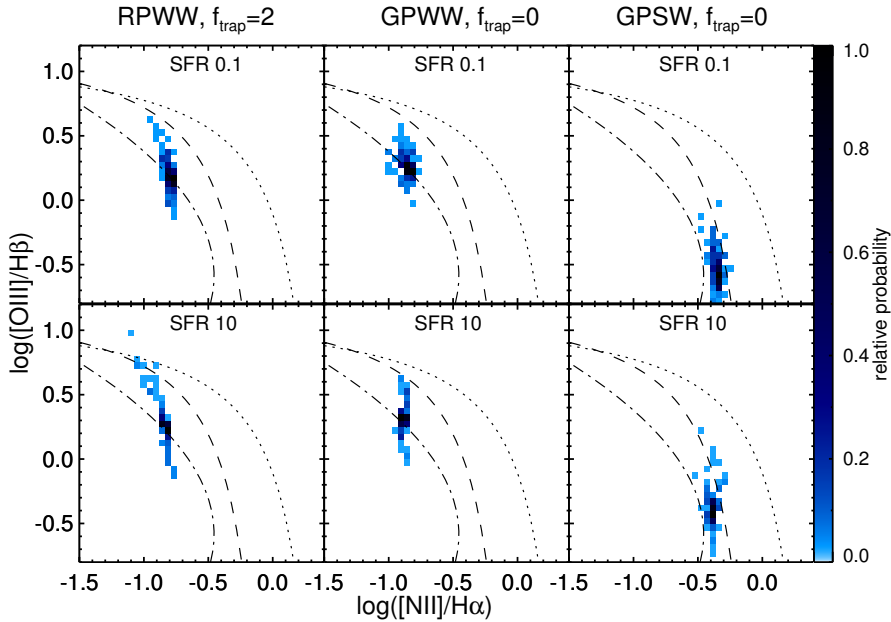
Figure 6.9 – Same as Figure 6.8, but here the top and bottom rows correspond to star formation rates of 0.1 and 10 $M_\odot$ yr^{-1}. All other parameters are the same as in the fiducial case.

6.3.3 Influence of galactic parameters

While there are a number of parameters in our model that make very little difference to the results, the two parameters P_{amb} and SFR that we use to characterize our galaxies do have a measurable influence. Figure 6.8 shows how the ambient pressure influences the position of simulated galaxies on the BPT diagram. We show our three models computed with $P_{\mathrm{amb}}/k_B = 10^3$ and 10^6 K cm^{-3} (top and bottom rows). At low ambient pressure, we find a significantly larger spread in the simulated galaxies. This is because for low ambient pressure the stalling radius is large, many H II regions do not live to reach it, and thus H II regions span a large range of radii. Exactly where H II regions fall in the plane of S and R_{IF} is therefore subject to a great deal of stochastic variation. In contrast, as show in Figure 6.5, increasing the ambient pressure causes all the H II regions in a galaxy to cluster along the stall radius line. In Figure 6.8 we can also see that the ambient pressure controls the overall location in the BPT plot, moving all the synthetic galaxies to a higher position in the BPT diagram, and at higher ionization parameter.

Figure 6.9 shows the effects of varying the SFR on the location of our synthetic galaxies on the BPT diagram. As the Figure shows, a smaller SFR leads a bigger spread of points in the BPT diagram. This is due to the stochastic nature of star formation at low SFRs, something that can also lead to large variations in absolute line fluxes as well as line ratios (Fumagalli et al. 2011, da Silva et al. 2012, Weisz et al. 2012). If we draw

a large mass for the next association to be created, a long time passes until it appears, especially when the SFR is low. During this phase there are no young, bright H II regions present, and so the galaxy is located in the bottom-right part of the BPT plot. When the association finally forms, the galaxy's line emission becomes dominated by the resulting bright, young H II region, which drives it to the top-left part of the BPT diagram. As a result, there is a great deal of variation in the galaxy's location. When the SFR is high, on the other hand, H II regions form continuously, causing the population of H II regions to be more numerous and uniform. We do caution that our mechanism for handling H II region creation may overestimate the amount of stochasticity found in real galaxies, but that the general sense of the effect will be the same as we have found, even if its magnitude is overestimated. A more realistic formalism for handling the problem of drawing association masses and birth times subject to an overall constraint on the star formation rate is implemented in the SLUG code (da Silva et al. 2012); adding this formalism to our code is left for future work.

6.4   Comparison to observations

Having understood the physics that drives the location of galaxies in the BPT diagram, we are now in a position to compare our models to observations. Such observations come in two varieties: spatially resolved ones of individual H II regions or portions of galaxies, and unresolved ones in which the line fluxes from all the H II regions in a galaxy are summed. Since our code produces collections of stochastically-sampled H II regions, we can compare to both. For reference and to facilitate comparison, we show in both cases unresolved observations of local galaxies from the SDSS (Brinchmann et al. 2004, Tremonti et al. 2004) along with a fit to this sequence (Brinchmann et al. 2008), the empirically-determined line separating star-forming galaxies from AGN (Kauffmann et al. 2003), and the Kewley et al. (2001) theoretical upper limit to star forming galaxies. The single H II region sequence and the SDSS star forming galaxy sequence overlap, at least in the upper left part of the BPT diagram, while high redshift galaxies seem to create a different sequence, upward and to the right (Liu et al. 2008, Brinchmann et al. 2008, Hainline et al. 2009, Erb et al. 2010).

Figure 6.10 shows a collection of observations of single H II regions and pixel by pixel observations taken from the literature. For the local Universe, our comparison data set consists of single H II regions from NGC 1365 (Roy & Walsh 1997), NGC 1313 (Walsh & Roy 1997), and the Orion region in our own galaxy (Sánchez et al. 2007). We also plot individual pixels in three lensed galaxy at $z \sim 2$ from Jones et al. (2012), which scatter about a locus that passes close to the location of Orion in the BPT diagram. As pointed out by Walter et al. (2009), the SFR surface density of Orion is similar to that of a high redshift object undergoing a burst of star formation.

On top of these data, we overlay the results of our simulations using model RPWW, which we consider most realistic based on observations of nearby H II regions. The results shown are single snapshots of all the H II regions produced in two different simulations, one with $P_{amb}/k_B = 10^4$ K cm^{-3} one with 10^6 K cm^{-3}. These two cases should roughly
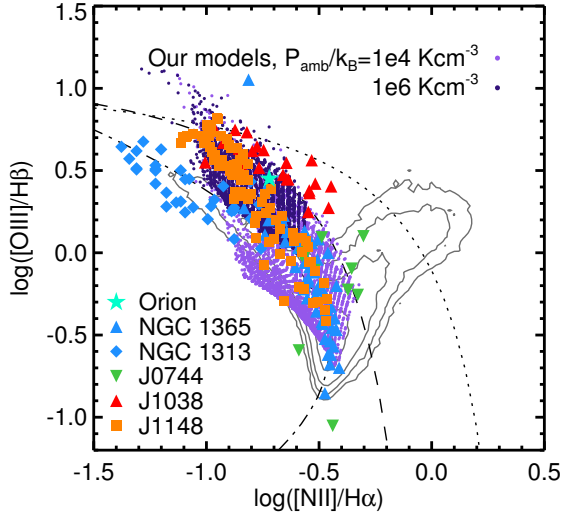
Figure 6.10 – A comparison between resolved H II regions and individual H II regions produced in our simulations in the BPT diagram. We show H II regions in galaxies at $z = 0$ with blue symbols; the galaxies shown are NGC 1365 (Roy & Walsh 1997) (triangles), NGC 1313 (Walsh & Roy 1997) (diamonds), and the integrated value for the Orion nebula (Sánchez et al. 2007) (star). We also show single spatial pixels measured with OSIRIS for three lensed galaxies at redshift $z \sim 2.0$-2.4 from (Jones et al. 2012) (green, red, and orange). Contours represent galaxies from the SDSS catalogue (Brinchmann et al. 2004), enclosing respectively, 5, 10, 20, 50, 90 and 99% of all galaxies in which the four emission lines are detected at a greater than 3σ significance level. Blue and purple points show the results of our models using fiducial parameters and $P_{amb}/k_B = 10^4$ and 10^6 K cm^{-3}, respectively. Finally, the dotted line is the theoretical upper limit of Kewley et al. (2001), the dashed line is the empirical AGN - star-forming galaxy separating line (Kauffmann et al. 2003), and the dot-dashed line is the fit to the SDSS sample of Brinchmann et al. (2008).

bracket what we expect for Milky Way-like galaxies and for the dense, more strongly star-forming galaxies found at high redshift. The plot shows that our simulations are able to roughly reproduce the locus of observed H II regions in the BPT diagram for a reasonable range of ambient pressures. We cannot reproduce most of the H II regions in NGC 1313, because the galaxy has a metallicity lower than solar and our model considers only solar metallicities. Lower metallicity produces a shift of the models towards lower [N II]/Hα values (Dopita et al. 2000). The pixel by pixel high-z galaxies are best fit by the models with high P_{amb}, consistent with observations that these galaxies have high surface and volume densities.

Figure 6.11 shows the comparison with integrated galaxy measurements; these come from the SDSS for the local Universe, and from a variety of surveys at high-z. Many SDSS star forming galaxies lie in the lower part of the star forming sequence due to the presence of a diffuse warm component in the interstellar medium. Brinchmann et al.
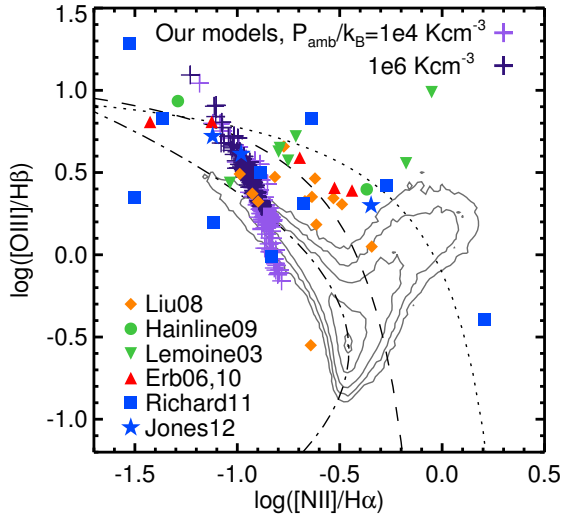
Figure 6.11 – A comparison between observed unresolved galaxies and simulated produced by our code in the BPT diagram. Contours and lines are the same as in Figure 6.10. Diamonds show galaxies at $z \sim$ 1-1.4 taken from the DEEP2 survey Shapley et al. (2005), Liu et al. (2008); triangles show galaxies at $z \sim 2$ taken from Erb et al. (2006a, 2010); lensed galaxies at a variety of redshifts and samples are indicated by inverted triangles (Lemoine-Busserolle et al. 2003), circles (Hainline et al. 2009), squares (Richard et al. 2011), and stars (Jones et al. 2012). Blue and purple plus signs show the results for integrated galaxies in of our models using fiducial parameters, Model RPWW, and ambient pressures of $P_{amb}/k_B = 10^4$ and 10^6 K cm^{-3}. Each point represents a single time snapshot taken at 1 Myr intervals from a simulation that evolves for 200 Myr.

(2004) point out that a significant amount of the emission line flux in these galaxies comes from the diffuse ionized gas, rather than from H II regions. The combination of the diffuse ionized gas and the H II regions typically has a lower effective ionization parameter, and compared to H II regions alone it shows an enhanced [N II]/Hα and depressed [O III]/Hβ (Mathis 2000). Therefore, we only expect our models, which do not include the diffuse ionized gas, to reproduce the upper part of the star forming sequence of the SDSS.

In Figure 6.11 we also overplot the whole-galaxy results produced by our code. As the plot shows, while we are able to reproduce the full spread of individual H II regions, our simulations of whole galaxies cover a more limited range of BPT than the observations. In particular, we tend to underpredict the observed [N II]/Hα ratios. There are several possible explanations for why we might successfully reproduce individual H II regions, even in high-z galaxies, but not fully cover the range of integrated galaxy properties. One we have already discussed in the introduction: the offset at high-z may be due to the contribution of a weak AGN, which our models obviously do not include. A second possibility is that the contribution of diffuse ionized gas to the line ratios cannot be neglected even

in these high redshift galaxies. Another is that our weighting of the different H II regions is incorrect because the association mass function is different than the -2 powerlaw we have adopted based on local observations, or because of biases introduced by dust extinction, despite the extinction-independent nature of the BPT line ratios (see Yeh & Matzner 2012). A fourth possibility is that our lognormal distribution of densities provides a poor fit to the true range of densities into which H II regions expand in high-z galaxies, so that the amount of time individual H II regions spend in the upper left versus the lower right parts of the BPT diagram is off in our models.

As a last possibility, we recognize that the ability of our models for individual H II regions to reproduce the observations of Orion very well (Figure 6.10) may be partly a matter of good luck. Our models are not designed to mimic the champagne flow phase of young ($< 10^5$ yr), compact H II regions. In particular, we assume a state of quasi-static force balance which holds only approximately in accelerating flows; see Yeh & Matzner (2012) Section 3.4 on this point. Indeed, Orion does not resemble the typical H II region - e.g., a few million years old and at the stalling radius - in our galaxy simulations. It is possible that the different distribution of high-z galaxies in the BPT plot as compared to local SDSS galaxies is due to the higher pressure environment in the former, which keeps the H II regions longer in a champagne flow-like phase. Future studies might assess our models' accuracy in the champagne phase, extend their range of validity, and quantify the importance of this dynamical detail for high-z galaxies.

6.5 Discussion and conclusions

Motivated by recent observations suggesting that H II regions are shaped much less than expected by the pressure of shocked stellar wind gas, and much more by direct radiation pressure (Harper-Clark & Murray 2009, Lopez et al. 2011, Yeh & Matzner 2012), we revisit the problem of determining the line flux emitted by a population of H II regions. We adopt as our default a model of H II regions where the pressure of winds is subdominant, and radiation pressure is not neglected, and we compare this result to traditional models with strong winds and weak radiation pressure. In Paper I we discuss how we generate grids of static, single H II regions, with a wide range of sizes and ionizing luminosities, with varying strengths of winds and radiation pressure. In this paper we construct dynamical expansion models for these H II regions, and explore how changing the strength of winds and radiation pressure affects their line ratios in the BPT diagram. We find that radiation pressure has two important effects. First, P_{rad} changes the internal structure of the H II region, creating a density gradient towards the outer shell. This affects the expected line emission, allowing the H II regions to exceed the upper limit form starburst models set by Kewley et al. (2001). Second, radiation pressure provides an extra boost to the expansion, leading to larger radii at earlier times.

We embed these models in a population synthesis code that generates galactic collections of stochastically-generated H II regions expanding into a turbulent medium. The code follows H II regions as they are born, evolve, stall and die. Using this code we predict the integrated line emission of galaxies as a function of several galactic properties. We

find that the two most important ones in controlling where galaxies appear in the BPT diagram are the ambient pressure, which shifts galaxies up and to the left as it increases, and the star formation rate, which affects the amount of stochastic scatter in a galaxy's line ratios.

We compare with observations in two distinct ways. First, we select single H ii regions observed in the local universe and pixel by pixel observations of $z \sim 2$ galaxies, and we compare these to the distributions of individual H ii regions produced in our model. We show that our model produces good agreement with the observations for reasonable ranges of SFR and ambient pressure. The high redshift pixel data are best reproduced by H ii regions evolving in a high pressure medium and with high SFR, which we interpret as a sign of intense star formation in a dense interstellar medium, consistent with the observed properties of high-z galaxies (e.g. Elmegreen et al. 2009, Genzel et al. 2011).

Second, we compare integrated galaxies from the SDSS catalogue and the high redshift universe to our synthetic galaxies. We find that, while we are able to reproduce the spread of individual H ii regions, our models for integrated galaxies cluster too tightly compared to the observed range of line ratios in real galaxies, particularly at high-z. This might be due to a number of factors. One possibility is that the lognormal distribution of the ambient density we have adopted is a poor description of the density distribution in high-z galactic disks. Another possibility is that winds might be important at high redshift or that the presence of the diffuse ionized medium is not negligible. A third possibility is that a higher pressure environment in high-z galaxies keeps the H ii regions longer in a champagne flow-like phase. One last possibility is that $z \sim 2$ star forming galaxies may contain an AGN that partially contributes to the line emission. We leave these possibilities as a subject for future work.

Bibliography

Abel, T., Norman, M. L., & Madau, P. 1999, ApJ, 523, 66

Alves, J. F., Lada, C. J., & Lada, E. A. 2001, Nature, 409, 159

Anderson, L. D. & Bania, T. M. 2009, ApJ, 690, 706

Anderson, L. D., Bania, T. M., Balser, D. S., & Rood, R. T. 2012, ApJ, 754, 62

Aniano, G., Draine, B. T., Gordon, K. D., & Sandstrom, K. 2011, PASP, 123, 1218

Arthur, S. J. 2012, MNRAS, 421, 1283

Arthur, S. J. & Hoare, M. G. 2006, ApJS, 165, 283

Baldwin, J. A., Phillips, M. M., & Terlevich, R. 1981, PASP, 93, 5

Bania, T. M., Anderson, L. D., Balser, D. S., & Rood, R. T. 2010, ApJ, 718, L106

Beaumont, C. N. & Williams, J. P. 2010, ApJ, 709, 791

Beltran, M. T., Olmi, L., Cesaroni, R., et al. 2013, ArXiv e-prints

Bendo, G. J., Galliano, F., & Madden, S. C. 2012, MNRAS, 423, 197

Benjamin, R. A., Churchwell, E., Babler, B. L., et al. 2003, PASP, 115, 953

Bernard, J.-P., Reach, W. T., Paradis, D., et al. 2008, AJ, 136, 919

Bertelli, G., Bressan, A., Chiosi, C., Fagotto, F., & Nasi, E. 1994, A&AS, 106, 275

Bianchi, L., Scuderi, S., Massey, P., & Romaniello, M. 2001, AJ, 121, 2020

Binette, L., Wilson, A. S., Raga, A., & Storchi-Bergmann, T. 1997, A&A, 327, 909

Bodenheimer, P., Tenorio-Tagle, G., & Yorke, H. W. 1979, ApJ, 233, 85

Brinchmann, J., Charlot, S., White, S. D. M., et al. 2004, MNRAS, 351, 1151

Brinchmann, J., Pettini, M., & Charlot, S. 2008, MNRAS, 385, 769

Broos, P. S., Feigelson, E. D., Townsley, L. K., et al. 2007, ApJS, 169, 353

Cannon, J. M., O'Leary, E. M., Weisz, D. R., et al. 2012, ApJ, 747, 122

Cannon, J. M., Walter, F., Armus, L., et al. 2006, ApJ, 652, 1170

Carey, S. J., Noriega-Crespo, A., Mizuno, D. R., et al. 2009, PASP, 121, 76

Castor, J., McCray, R., & Weaver, R. 1975, ApJ, 200, L107

Cesaroni, R., Churchwell, E., Hofner, P., Walmsley, C. M., & Kurtz, S. 1994, A&A, 288, 903

Chandrasekhar, S. 1961, Hydrodynamic and hydromagnetic stability

Charbonnel, C., Meynet, G., Maeder, A., & Schaerer, D. 1996, A&AS, 115, 339

Churchwell, E., Povich, M. S., Allen, D., et al. 2006, ApJ, 649, 759

Churchwell, E., Watson, D. F., Povich, M. S., et al. 2007, ApJ, 670, 428

Comeron, F. & Kaper, L. 1998, A&A, 338, 273

Condon, J. J. 1992, ARA&A, 30, 575

Condon, J. J., Cotton, W. D., Greisen, E. W., et al. 1998, AJ, 115, 1693

Cowie, L. L. & McKee, C. F. 1977, ApJ, 211, 135

Cox, A. N. 2000, Allen's astrophysical quantities (Springer-Verlag)

da Silva, R. L., Fumagalli, M., & Krumholz, M. 2012, ApJ, 745, 145

Dale, D. A., Helou, G., Contursi, A., Silbermann, N. A., & Kolhatkar, S. 2001, ApJ, 549, 215

de Blok, W. J. G. & Walter, F. 2000, ApJ, 537, L95

de Blok, W. J. G. & Walter, F. 2006, AJ, 131, 343

De Buizer, J. M., Watson, A. M., Radomski, J. T., Piña, R. K., & Telesco, C. M. 2002, ApJ, 564, L101

Deharveng, L., Schuller, F., Anderson, L. D., et al. 2010, A&A, 523, A6

Deharveng, L., Zavagno, A., Schuller, F., et al. 2009, A&A, 496, 177

Dopita, M. A., Fischera, J., Sutherland, R. S., et al. 2006a, ApJS, 167, 177

Dopita, M. A., Fischera, J., Sutherland, R. S., et al. 2006b, ApJ, 647, 244

Dopita, M. A., Groves, B. A., Fischera, J., et al. 2005, ApJ, 619, 755

Dopita, M. A., Groves, B. A., Sutherland, R. S., Binette, L., & Cecil, G. 2002, ApJ, 572, 753

Dopita, M. A., Kewley, L. J., Heisler, C. A., & Sutherland, R. S. 2000, ApJ, 542, 224

Draine, B. T. 2011, ApJ, 732, 100

Dudik, R. P., Weingartner, J. C., Satyapal, S., et al. 2007, ApJ, 664, 71

Dwek, E. 1987, ApJ, 322, 812

Dyson, J. E., Williams, R. J. R., & Redman, M. P. 1995, MNRAS, 277, 700

Efremova, B. V., Bianchi, L., Thilker, D. A., et al. 2011, ApJ, 730, 88

Ekström, S., Georgy, C., Eggenberger, P., et al. 2012, A&A, 537, A146

Elmegreen, B. G. & Lada, C. J. 1977, ApJ, 214, 725

Elmegreen, D. M., Elmegreen, B. G., Marcus, M. T., et al. 2009, ApJ, 701, 306

Erb, D. K., Pettini, M., Shapley, A. E., et al. 2010, ApJ, 719, 1168

Erb, D. K., Shapley, A. E., Pettini, M., et al. 2006a, ApJ, 644, 813

Erb, D. K., Steidel, C. C., Shapley, A. E., et al. 2006b, ApJ, 646, 107

Everett, J. E. & Churchwell, E. 2010, ApJ, 713, 592

Fall, S. M., Krumholz, M. R., & Matzner, C. D. 2010, ApJ, 710, L142

Fazio, G. G., Hora, J. L., Allen, L. E., et al. 2004, ApJS, 154, 10

Ferland, G. J., Korista, K. T., Verner, D. A., et al. 1998, PASP, 110, 761

Ferland, G. J., Porter, R. L., van Hoof, P. A. M., et al. 2013, Rev. Mexicana Astron. Astrofis., 49, 137

Fey, A. L., Gaume, R. A., Claussen, M. J., & Vrba, F. J. 1995, ApJ, 453, 308

Fioc, M. & Rocca-Volmerange, B. 1997, A&A, 326, 950

Frank, A. & Mellema, G. 1994, A&A, 289, 937

Freyer, T., Hensler, G., & Yorke, H. W. 2003, ApJ, 594, 888

Freyer, T., Hensler, G., & Yorke, H. W. 2006, ApJ, 638, 262

Fryxell, B., Olson, K., Ricker, P., et al. 2000, ApJS, 131, 273

Fumagalli, M., da Silva, R. L., & Krumholz, M. R. 2011, ApJ, 741, L26

Galametz, M., Hony, S., Galliano, F., et al. 2013, MNRAS, 431, 1596

Galametz, M., Madden, S. C., Galliano, F., et al. 2010, A&A, 518, L55

Galliano, F., Hony, S., Bernard, J.-P., et al. 2011, A&A, 536, A88

García-Benito, R., Díaz, A., Hägele, G. F., et al. 2010, MNRAS, 408, 2234

Genzel, R., Newman, S., Jones, T., et al. 2011, ApJ, 733, 101

Girardi, L., Bertelli, G., Bressan, A., et al. 2002, A&A, 391, 195

Goldbaum, N. J., Krumholz, M. R., Matzner, C. D., & McKee, C. F. 2011, ApJ, 738, 101

Gritschneder, M. & Burkert, A. 2013, ArXiv e-prints

Groves, B., Dopita, M. A., Sutherland, R. S., et al. 2008, ApJS, 176, 438

Groves, B. A., Dopita, M. A., & Sutherland, R. S. 2004, ApJS, 153, 75

Güdel, M., Briggs, K. R., Montmerle, T., et al. 2008, Science, 319, 309

Hainline, K. N., Shapley, A. E., Kornei, K. A., et al. 2009, ApJ, 701, 52

Harper-Clark, E. & Murray, N. 2009, ApJ, 693, 1696

Hartquist, T. W., Dyson, J. E., Pettini, M., & Smith, L. J. 1986, MNRAS, 221, 715

Helfand, D. J., Becker, R. H., White, R. L., Fallon, A., & Tuttle, S. 2006, AJ, 131, 2525

Henney, W. J. & Arthur, S. J. 1998, AJ, 116, 322

Hindmarsh, A. C. 1980, SIGNUM Newsl., 15, 10

Hopkins, P. F., Quataert, E., & Murray, N. 2011, MNRAS, 1513, in press, arXiv:1101.4940

Houck, J. R., Roellig, T. L., van Cleve, J., et al. 2004, ApJS, 154, 18

Iliev, I. T., Ciardi, B., Alvarez, M. A., et al. 2006, MNRAS, 371, 1057

Iliev, I. T., Whalen, D., Mellema, G., et al. 2009, MNRAS, 400, 1283

Jones, T., Ellis, R. S., Richard, J., & Jullo, E. 2012, ArXiv e-prints

Kahn, F. D. & Breitschwerdt, D. 1990, MNRAS, 242, 209

Kandori, R., Nakajima, Y., Tamura, M., et al. 2005, AJ, 130, 2166

Kauffmann, G., Heckman, T. M., Tremonti, C., et al. 2003, MNRAS, 346, 1055

Kendrew, S., Simpson, R., Bressert, E., et al. 2012, ApJ, 755, 71

Kennicutt, Jr., R. C., Armus, L., Bendo, G., et al. 2003, PASP, 115, 928

Kewley, L. J., Dopita, M. A., Leitherer, C., et al. 2013a, ArXiv e-prints

Kewley, L. J., Dopita, M. A., Sutherland, R. S., Heisler, C. A., & Trevena, J. 2001, ApJ, 556, 121

Kewley, L. J., Maier, C., Yabe, K., et al. 2013b, ArXiv e-prints

Kroupa, P. 2001, MNRAS, 322, 231

Krumholz, M. R. & Matzner, C. D. 2009, ApJ, 703, 1352

Krumholz, M. R., Matzner, C. D., & McKee, C. F. 2006, ApJ, 653, 361

Krumholz, M. R. & Thompson, T. A. 2007, ApJ, 669, 289

Krumholz, M. R. & Thompson, T. A. 2012, ApJ, 760, 155

Krumholz, M. R. & Thompson, T. A. 2013, ArXiv e-prints

Leitherer, C., Schaerer, D., Goldader, J. D., et al. 1999, ApJS, 123, 3

Lejeune, T., Cuisinier, F., & Buser, R. 1997, A&AS, 125, 229

Lejeune, T., Cuisinier, F., & Buser, R. 1998, A&AS, 130, 65

Lemoine-Busserolle, M., Contini, T., Pelló, R., et al. 2003, A&A, 397, 839

Levesque, E. M., Kewley, L. J., & Larson, K. L. 2010, AJ, 139, 712

Liu, X., Shapley, A. E., Coil, A. L., Brinchmann, J., & Ma, C.-P. 2008, ApJ, 678, 758

Lopez, L. A., Krumholz, M. R., Bolatto, A. D., Prochaska, J. X., & Ramirez-Ruiz, E. 2011, ApJ, 731, 91

López-Hernández, J., Terlevich, E., Terlevich, R., et al. 2013, MNRAS, 430, 472

Mac Low, M.-M., Toraskar, J., Oishi, J. S., & Abel, T. 2007, ApJ, 668, 980

Mac Low, M.-M., van Buren, D., Wood, D. O. S., & Churchwell, E. 1991, ApJ, 369, 395

Mackey, J., Langer, N., & Gvaramadze, V. V. 2013, ArXiv e-prints

Madden, S. C., Rémy-Ruyer, A., Galametz, M., et al. 2013, PASP, 125, 600

Marcolino, W. L. F., Bouret, J.-C., Martins, F., et al. 2009, A&A, 498, 837

Martín-Hernández, N. L., Bik, A., Kaper, L., Tielens, A. G. G. M., & Hanson, M. M. 2003, A&A, 405, 175

Martín-Hernández, N. L., Peeters, E., Morisset, C., et al. 2002, A&A, 381, 606

Martins, F., Pomarès, M., Deharveng, L., Zavagno, A., & Bouret, J. C. 2010, A&A, 510, A32

Bibliography

Martins, F., Schaerer, D., & Hillier, D. J. 2005, A&A, 436, 1049

Massey, P., Olsen, K. A. G., Hodge, P. W., et al. 2007, AJ, 133, 2393

Mateo, M. L. 1998, ARA&A, 36, 435

Mathis, J. S. 2000, ApJ, 544, 347

Matzner, C. D. 2002, ApJ, 566, 302

Mellema, G., Iliev, I. T., Pen, U.-L., & Shapiro, P. R. 2006, MNRAS, 372, 679

Misselt, K. A., Clayton, G. C., & Gordon, K. D. 1999, ApJ, 515, 128

Mokiem, M. R., de Koter, A., Puls, J., et al. 2005, A&A, 441, 711

Molinari, S., Swinyard, B., Bally, J., et al. 2010, PASP, 122, 314

Monreal-Ibero, A., Relaño, M., Kehrig, C., et al. 2011, MNRAS, 413, 2242

Moorwood, A., Cuby, J.-G., Biereichel, P., et al. 1998, The Messenger, 94, 7

Morisset, C., Schaerer, D., Martín-Hernández, N. L., et al. 2002, A&A, 386, 558

Mukai, K. 1993, Legacy, vol. 3, p.21-31, 3, 21

Murray, N., Quataert, E., & Thompson, T. A. 2010, ApJ, 709, 191

Murray, N. & Rahman, M. 2010, ApJ, 709, 424

Najarro, F., Hanson, M. M., & Puls, J. 2011, A&A, 535, A32

O'Dell, C. R., Hodge, P. W., & Kennicutt, Jr., R. C. 1999, PASP, 111, 1382

Oskinova, L. M., Gruendl, R. A., Ignace, R., et al. 2010, ApJ, 712, 763

Osterbrock, D. E. & Ferland, G. J. 2006, Astrophysics of gaseous nebulae and active galactic nuclei
    (Sausalito, CA: University Science Books)

Padoan, P. & Nordlund, Å. 2002, ApJ, 576, 870

Parravano, A., Hollenbach, D. J., & McKee, C. F. 2003, ApJ, 584, 797

Pellegrini, E. W., Baldwin, J. A., & Ferland, G. J. 2011, ApJ, 738, 34

Peters, T., Banerjee, R., Klessen, R. S., et al. 2010, ApJ, 711, 1017

Pilbratt, G. L., Riedinger, J. R., Passvogel, T., et al. 2010, A&A, 518, L1

Pillai, T., Kauffmann, J., Wyrowski, F., et al. 2011, A&A, 530, A118

Pittard, J. M., Dyson, J. E., & Hartquist, T. W. 2001a, A&A, 367, 1000

Pittard, J. M., Hartquist, T. W., & Dyson, J. E. 2001b, A&A, 373, 1043

Pratap, P., Megeath, S. T., & Bergin, E. A. 1999, ApJ, 517, 799

Puls, J., Urbaneja, M. A., Venero, R., et al. 2005, A&A, 435, 669

Puls, J., Vink, J. S., & Najarro, F. 2008, A&A Rev., 16, 209

Raga, A. C., Noriega-Crespo, A., Cantó, J., et al. 1997, Rev. Mexicana Astron. Astrofis., 33, 73

Raicevic, M. 2010, PhD thesis

Redman, M. P., Williams, R. J. R., & Dyson, J. E. 1996, MNRAS, 280, 661

Relaño, M., Monreal-Ibero, A., Vílchez, J. M., & Kennicutt, R. C. 2010, MNRAS, 402, 1635

Rémy-Ruyer, A., Madden, S. C., Galliano, F., et al. 2013, ArXiv e-prints

Repolust, T., Puls, J., & Herrero, A. 2004, A&A, 415, 349

Richard, J., Jones, T., Ellis, R., et al. 2011, MNRAS, 413, 643

Rieke, G. H., Young, E. T., Engelbracht, C. W., et al. 2004, ApJS, 154, 25

Rijkhorst, E.-J., Plewa, T., Dubey, A., & Mellema, G. 2006, A&A, 452, 907

Roy, J.-R. & Walsh, J. R. 1997, MNRAS, 288, 715

Russeil, D., Pestalozzi, M., Mottram, J. C., et al. 2011, A&A, 526, A151

Rybicki, G. B. & Lightman, A. P. 1979, Radiative processes in astrophysics

Salgado, F., Berné, O., Adams, J. D., et al. 2012, ApJ, 749, L21

Sánchez, S. F., Cardiel, N., Verheijen, M. A. W., et al. 2007, A&A, 465, 207

Sarazin, C. L. 2009, X-Ray Emission from Clusters of Galaxies

Schaerer, D., Charbonnel, C., Meynet, G., Maeder, A., & Schaller, G. 1993a, A&AS, 102, 339

Schaerer, D., Meynet, G., Maeder, A., & Schaller, G. 1993b, A&AS, 98, 523

Schaller, G., Schaerer, D., Meynet, G., & Maeder, A. 1992, A&AS, 96, 269

Schmutz, W. 1998, in Astronomical Society of the Pacific Conference Series, Vol. 131, Properties of Hot Luminous Stars, ed. I. Howarth, 119

Shapley, A. E., Coil, A. L., Ma, C.-P., & Bundy, K. 2005, ApJ, 635, 1006

Silich, S. & Tenorio-Tagle, G. 2013, ApJ, 765, 43

Simpson, R. J., Povich, M. S., Kendrew, S., et al. 2012, MNRAS, 424, 2442

Smith, J. D. T., Armus, L., Dale, D. A., et al. 2007, PASP, 119, 1133

Spitzer, L. 1978, Physical processes in the interstellar medium (Wiley-Interscience)

Sutherland, R. S. & Dopita, M. A. 1993, ApJS, 88, 253

Teixeira, P. S., Lada, C. J., & Alves, J. F. 2005, ApJ, 629, 276

Tenorio-Tagle, G. 1979, A&A, 71, 59

Theuns, T., Leonard, A., Efstathiou, G., Pearce, F. R., & Thomas, P. A. 1998, MNRAS, 301, 478

Townsley, L. K., Broos, P. S., Chu, Y.-H., et al. 2011, ApJS, 194, 16

Townsley, L. K., Feigelson, E. D., Montmerle, T., et al. 2003, ApJ, 593, 874

Tramper, F., Sana, H., de Koter, A., & Kaper, L. 2011, ApJ, 741, L8

Tremonti, C. A., Heckman, T. M., Kauffmann, G., et al. 2004, ApJ, 613, 898

Trump, J. R., Weiner, B. J., Scarlata, C., et al. 2011, ApJ, 743, 144

Tsujimoto, M., Hosokawa, T., Feigelson, E. D., Getman, K. V., & Broos, P. S. 2006, ApJ, 653, 409

Vacca, W. D., Garmany, C. D., & Shull, J. M. 1996, ApJ, 460, 914

van Buren, D., Mac Low, M.-M., Wood, D. O. S., & Churchwell, E. 1990, ApJ, 353, 570

Veilleux, S., Cecil, G., & Bland-Hawthorn, J. 2005, ARA&A, 43, 769

Veilleux, S. & Osterbrock, D. E. 1987, ApJS, 63, 295

Verdolini, S., Raicevic, M., & Tramper, F. 2013a, in prep.

Verdolini, S., Yeh, S. C. C., Krumholz, M. R., Matzner, C. D., & Tielens, A. G. G. M. 2013b, ApJ, 769, 12

Vink, J. S., de Koter, A., & Lamers, H. J. G. L. M. 2000, A&A, 362, 295

Vishniac, E. T. 1983, ApJ, 274, 152

Walsh, J. R. & Roy, J.-R. 1997, MNRAS, 288, 726

Walter, F., Riechers, D., Cox, P., et al. 2009, Nature, 457, 699

Watson, A. M., Coil, A. L., Shepherd, D. S., Hofner, P., & Churchwell, E. 1997, ApJ, 487, 818

Watson, A. M. & Hanson, M. M. 1997, ApJ, 490, L165

Weaver, R., McCray, R., Castor, J., Shapiro, P., & Moore, R. 1977, ApJ, 218, 377

Weisz, D. R., Johnson, B. D., Johnson, L. C., et al. 2012, ApJ, 744, 44

Werner, M. W., Roellig, T. L., Low, F. J., et al. 2004, ApJS, 154, 1

Williams, J. P. & McKee, C. F. 1997, ApJ, 476, 166

Williams, R. J. R., Dyson, J. E., & Redman, M. P. 1996, MNRAS, 280, 667

Wood, D. O. S. & Churchwell, E. 1989, ApJS, 69, 831

Wright, S. A., Larkin, J. E., Graham, J. R., & Ma, C.-P. 2010, ApJ, 711, 1291

Yeh, S. C. C. & Matzner, C. D. 2012, ApJ, 757, 108

Yeh, S. C. C., Verdolini, S., Krumholz, M. R., Matzner, C. D., & Tielens, A. G. G. M. 2013, ApJ,

769, 11

Yorke, H. W., Tenorio-Tagle, G., & Bodenheimer, P. 1983, A&A, 127, 313

Zavagno, A., Pomarès, M., Deharveng, L., et al. 2007, A&A, 472, 835

Zhu, Q.-F., Lacy, J. H., Jaffe, D. T., Richter, M. J., & Greathouse, T. K. 2005, ApJ, 631, 381

Zhu, Q.-F., Lacy, J. H., Jaffe, D. T., Richter, M. J., & Greathouse, T. K. 2008, ApJS, 177, 584

Zinnecker, H. & Yorke, H. W. 2007, ARA&A, 45, 481

Het modelleren
van interstellaire bellen:
dichtbij en veraf

Het leven van een ster

Sterren zijn de bouwstenen van het zichtbare heelal. Ze zijn de grootste bron van licht dat we 's nachts kunnen zien en grote hoeveelheden sterren vormen tezamen sterrenstelsels. Een typisch sterrenstelsel, zoals ons Melkwegstelsel, bevat ongeveer 100 miljard sterren en het heelal als geheel bevat weer miljarden sterrenstelsels.

Sterren zijn gaswolken die bij elkaar worden gehouden door zwaartekracht. Elke ster heeft zijn eigen levensloop. Astronomen categoriseren sterren op basis van massa. De massa van een ster is zijn belangrijkste karakteristiek en bepaalt in grote mate andere eigenschappen van de ster, waaronder hoe het leven van de ster verloopt. Sterren met een kleine massa, zoals onze zon, zijn zeer stabiel en leven lang: tot ruim 10 miljard jaar. Ze verbranden waterstof in hun kern om de energie te produceren die als licht wordt uitgestraald. Dit licht is wat we zien als sterren aan de hemel en ook het licht van de zon wordt op deze manier geproduceerd.

Sterrenkundigen bestuderen de vorming en evolutie van sterren. Sterren met een kleine massa worden redelijk goed begrepen, maar over sterren met een grote massa van 10 tot 50 keer de massa van de zon is nog veel onduidelijk. Ondanks dat deze sterren een grotere massa en daardoor veel meer brandstof hebben, leven ze toch maar tot een fractie van de leeftijd van de lichtere sterren. Dit komt doordat massieve sterren naar verhouding veel meer licht uitstralen en daardoor veel sneller door hun brandstof heen branden. Massieve sterren leven daardoor 'slechts' een aantal miljoen jaar. De grote hoeveelheid licht die deze sterren uitstralen, ioniseert het omliggende gas, waardoor een plasma ontstaat dat licht uitstraalt in ultraviolet, optische, infrarood en radio golflengtes. Gedurende hun leven stoten zware sterren ook een deel van hun massa uit naar hun omgeving in de vorm van stellaire winden en aan het einde van hun levensloop in een supernova explosie. Deze massieve sterren en hun impact op hun omgeving zijn het onderwerp van dit proefschrift.

De geboorte van een ster

Sterren vormen uit zeer ijle gaswolken die voornamelijk bestaan uit waterstof en een kleine hoeveelheid moleculen. Deze wolken worden moleculaire wolken genoemd. Mo-

leculaire wolken willen in elkaar storten onder hun eigen zwaartekracht, maar worden in stand gehouden door thermische en magnetische krachten en turbulentie. Echter, de wolken zijn niet homogeen en hebben gebieden van hogere dichtheid. Deze dichtere gebieden zullen onder hun eigen zwaartekracht inkrimpen en in elkaar storten. Dit proces resulteert in een dichte kern waar een ster zal vormen. Rond de ster vormt zich een envelop van materiaal dat op de ster valt. Deze envelop vormt uiteindelijk een schijf rond de ster en loodrecht op de schijf wordt een deel van het materiaal weer uitgestoten. Zodra de gasbol in de kern een dichtheid heeft bereikt die groot genoeg is om waterstoffusie tot stand te brengen, is een nieuwe ster geboren.

Het bovenstaande beschrijft het proces voor lichte sterren, maar het is niet duidelijk in hoeverre dit ook geldt voor massievere sterren. Over zware sterren is veel minder bekend doordat ze zeer moeilijk te observeren te zijn. Omdat ze relatief zo kort leven is de kans ze te vinden klein. Daarnaast worden er minder zware sterren gevormd. In plaats van één zware ster is de kans groter dat er meerdere lichtere sterren gevormd worden. Als laatste vormt de moleculaire wolk een barrière. Als de ster geboren wordt, bevindt deze zich middenin een dichte moleculaire wolk. De wolk is zo dicht dat het licht van de ster er niet doorheen kan dringen. Dit betekent dat de ster effectief aan het zicht onttrokken wordt.

H II gebieden en interstellaire bellen
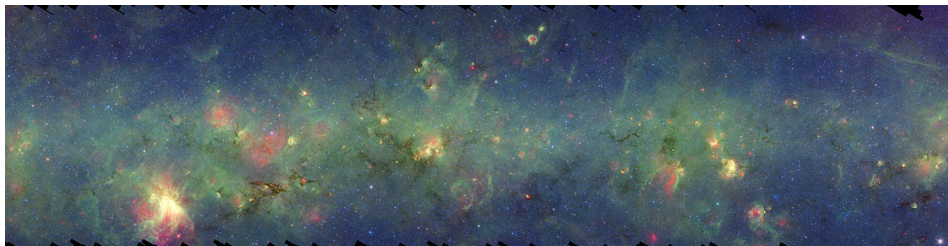
Figuur 1 – Segment van een infrarood portret van stof en sterren in de binnenste regionen van de Melkweg. Blauw is IRAC 3.6 μm (de PAH deeltjes), groen is IRAC 8 μm (de PAH deeltjes), en rood is MIPSGAL 24 μm (warme stofdeeltjes). Credit: NASA/JPL-Caltech/Univ. of Wisconsin.

Ondanks de observationele moeilijkheden is er wel een stadium van massieve stervorming dat waarneembaar is: zodra de ster grote hoeveelheden hoge-energie ultraviolette fotonen begint uit te stralen, zal hij het gas in de directe omgeving beginnen te ioniseren. Dit resulteert in wat astronomen een H II gebied noemen. Deze bestaat voornamelijk uit waterstof. Dit wordt al door de naam aangegeven, H II staat voor geïoniseerd waterstof, een atoom waterstof zonder zijn elektron. Het H II gebied heeft een temperatuur van rond de 10.000 graden Kelvin. Het licht dat deze H II gebieden uitstralen, geeft ons informatie over de omgeving van massieve sterren in wording.

Behalve het ioniseren van waterstof (en andere elementen) in hun omgeving kunnen sterren ook speciale moleculen aanslaan. Deze moleculen heten polycyclische aromatisch koolwaterstoffen (PAKs). Ze bestaan uit koolstofatomen in een honingraatstructuur om-

geven door waterstofatomen. Als deze aangeslagen worden door ultraviolette fotonen van een massieve ster dan fluoresceren ze in het mid-infrarood. Ook stofdeeltjes worden door de ster beïnvloed. Stofdeeltjes zijn in dit geval zeer kleine deeltjes die vooral bestaan uit koolstof, silicium en zuurstof. Deze worden door de ster opgewarmd, waardoor het stof licht uitstraalt in langere golflengtes. Zowel PAKs als stofdeeltjes bevinden zich in het interstellaire medium – het materiaal dat zich tussen sterren in een sterrenstelsel bevindt – tezamen met sterk verdund waterstofgas.

Al deze processen rondom de massieve ster resulteren in de indrukwekkende foto's van het Galactisch vlak genomen door de *Spitzer Space Telescope* (zie Figuur 1). Opvallend zijn de complexiteit en de variatie in de soort ' bellen' die waar te nemen zijn. Sommige regionen zijn complex van vorm en uitgebreid qua formaat, terwijl anderen kleiner zijn en minder grillig van vorm. Dergelijke structuren worden ' bellen' genoemd, ze zijn driedimensionale schillen die geassocieerd worden met de eerder genoemde H II gebieden. In principe zijn de schillen en de H II gebieden onderdeel van hetzelfde proces – een ster die zijn direct omgeving beïnvloedt – maar gezien op verschillende manieren. Het H II gebied is de binnenkant van het object, terwijl de bel de grens van het gebieden met de omliggende omgeving is. Mede dankzij het Milky Way Project, een wetenschappelijk burgerinitiatief, is het aantal bekende infrarode bellen in het Galactisch vlak gegroeid naar ongeveer 5100. Dit is 10 keer zoveel als voorheen ontdekt was door reguliere studies ondernomen door astronomen.

H II gebieden: ballonnen tussen de sterren

Eén van de vragen die wij proberen te beantwoorden in dit proefschrift is gerelateerd aan de evolutie van een H II gebied. De uitdijing van een H II gebied is vergelijkbaar met het opblazen van een ballon: de afmeting van de ballon neemt toe naarmate er meer lucht in de ballon wordt geblazen. Wat er fysisch gezien gebeurt is dat de druk binnen de ballon toeneemt ten opzichte van de druk van de omgeving. In een soortgelijk proces weet de ster de druk in zijn directe omgeving te verhogen. Hierdoor ontstaat er een bel om de ster heen die uitzet en daarbij het omliggende materiaal naar buiten opveegt. De bel is dus een radiaal uitzettende schil van materiaal.

Er is een open discussie over wat de precieze oorzaak is van de druktoename in de omgeving rond de ster. Volgens sommigen is deze het gevolg van straling, terwijl het volgens anderen door stellaire winden wordt veroorzaakt. Figuur 2 illustreert enkele oplossingen aangedragen door astronomen om H II gebieden te verklaren. Als het gas rondom de ster homogeen is, dan zal het H II gebied bolvormig zijn. In Figuur 2 wordt dit geïllustreerd in scenario's (A) en (B).

In het geval van scenario (A) wordt het medium rondom de ster simpelweg geïoniseerd door de straling van de ster. Door deze ionisatie heeft het medium een hogere temperatuur en druk dan zijn omgeving en zal hierdoor uitdijen. Deze uitdijing neemt de vorm aan van een schokgolf die het omliggende materiaal als het ware opveegt. Scenario (B) in Figuur 2 laat de structuur van een H II gebied zien als er stellaire winden aanwezig zijn. Dergelijke uitstromen met hoge snelheid veroorzaken een extra schokgolf binnenin het H II gebied. Als laatste wordt in scenario (C) geïllustreerd wat er gebeurt als het omliggende materiaal
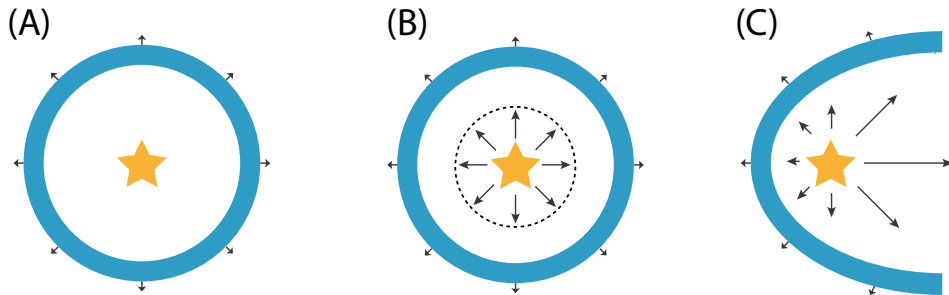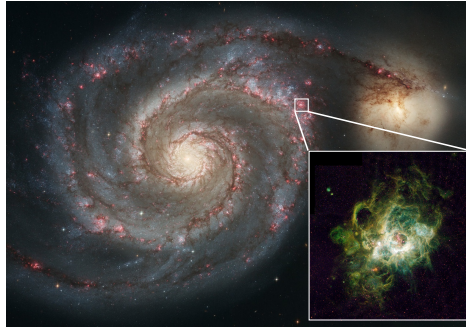
Figuur 2 – Schetsen van H II gebieden (A) gedreven door overdruk veroorzaakt door het geïoniseerde gas; (B) gedreven door stellaire winden ; en (C) als er een dichtheidsgradiënt in het omliggende materiaal aanwezig is (het zogenaamde champagne model). Credit: Bram Ochsendorf.

een gradiënt in dichtheid heeft. Een gradiënt in de dichtheid betekent dat de dichtheid rondom de ster niet overal even groot is en dus bijvoorbeeld hoger is aan één zijde van een ster en langzaam afneemt richting de andere zijde. In dit geval is het H II gebied niet langer bolvormig, maar krijgt deze de vorm van een komeet. Het gas in het H II gebied beweegt naar buiten waardoor dit model ook wel het champagne model genoemd wordt.

Er zijn veel factoren die bijdragen aan de vorming en evolutie van H II gebieden en het is niet moeilijk om voor te stellen dat de natuurkunde die hierbij aan te pas komt zeer complex kan zijn. Men hoeft maar naar het bekendste voorbeeld van een H II gebied te kijken, de Orion nevel (Figuur 1.1), om dit te beseffen.

Ultracompacte H II gebieden

De vroege fase in de evolutie van een H II gebied heet een Ultracompacte H II gebied. In Hoofdstuk 2 bestuderen we dergelijke objecten. In dit hoofdstuk focussen wij ons op een prototypische gebied, G29.96-0.02, en onderzoeken we de ontbrekende röntgenemissie bij stellaire wind bellen in H II gebieden. We voeren een brede studie uit waarbij we röntgenwaarnemingen van het hete gas combineren met een spectroscopische studie naar de eigenschappen van de ioniserende ster en een hydrodynamische studie naar de dynamische evolutie van deze gebieden. We construeren een driedimensionaal hydrodynamisch model van de Ultracompacte H II gebied. Hierbij wordt rekening gehouden met de effecten van foto-ionisatie, stellaire winden, radiatieve processen en de boegschok veroorzaakt door de beweging van de ster door de wolk. Ook wordt rekening gehouden met 'mass loading'. In de omgeving van de ster zijn vaak dichte wolken gas en stof te vinden. Deze worden niet zomaar geïoniseerd, maar verdampen langzaam. Dit kan gevolgen hebben voor het H II gebied. We vinden dat het champagne model het beste de morfologie en gasdynamica verklaren. Ook blijkt dat 'mass loading' nodig is om het gas in de stellaire wind af te koelen, zodat het consistent is met de röntgenwaarnemingen.

Figuur 3 – De verhouding tussen een sterrenstelsel en een H II gebied. De grote afbeelding is M51, een spiraalstelsel, en de kleine afbeelding is NGC 604, een gigantische H II gebied in M33. De afstandsschalen van de beide figuren zijn niet vergelijkbaar. De vergelijking is voornamelijk om te illustreren hoeveel meer we zouden kunnen zien als het sterrenstelsel dichtbij genoeg zou staan om de individuele sterren te onderscheiden.

Stoffige H II gebieden

In Hoofdstuk 3 presenteren we een klasse van H II gebieden die gevormd zijn door het champagne model om de komeetvorm van de stofemissie te verklaren zoals deze wordt waargenomen in H II gebieden. Wij denken dat de boogachtige structuur waargenomen bij 24 μm het resultaat is van de stralingsdruk van sterfotonen op het stof dat zich in de stroom van geïoniseerd gas bevindt. Dit geïoniseerde gas is afkomstig van de moleculaire wolk waarin de ster zich heeft gevormd. Deze interactie tussen ster en stof noemen wij een *dust wave*. We laten zien dat als het champagne model geldt, het geïoniseerde gas in het H II gebied snelheden bereikt op de locatie van de ster die groot genoeg zijn om een dergelijke *dust wave* mogelijk te maken. Deze modellen kunnen ook waargenomen morfologieën en emissiekarakteristieken van H II gebieden reproduceren.

Van sterren naar sterrenstelsels

Sterrenstelsels zijn verzamelingen van miljarden sterren. Op basis van waarnemingen kunnen we sterrenstelsels opdelen in twee categorieën: elliptische stelsels en spiraalstelsels. In dit werk zijn we geïnteresseerd in spiraalsterrenstelsels omdat deze nog actief sterren vormen, terwijl elliptische stelsels dit niet meer doen. Dit onderscheid is belangrijk omdat onze focus op zware sterren ligt en deze slechts zeer kort leven. Figuur 3 toont een typisch spiraalsterrenstelsel (M51). Langs de spiraalarmen worden grote hoeveelheden sterren gevormd en zijn er veel H II gebieden zichtbaar. In dezelfde figuur wordt ook NGC 604 getoond. Dit is een gigantische H II gebied in M33, een sterrenstelsel dichtbij onze Melkweg. De figuur laat zien hoe de afmeting van een sterrenstelsel zich verhoudt tot de afmeting van een H II gebied. Veel van het licht afkomstig van een stervormend sterrenstelsel is het resultaat van alle H II gebieden binnen het sterrenstelsel. Echter, de

meeste sterrenstelsels staan op grote afstanden van ons en daardoor is het onmogelijk om ze zo mooi in beeld te brengen zoals in Figuur 3. Meestal is een sterrenstelsel zelfs niet meer dan een vage lichtvlek omdat ze zo ver weg staan. Desondanks willen we de eigenschappen van sterrenstelsels begrijpen. Daarom bestuderen we H ɪɪ gebieden in ons eigen sterrenstelsel waar we ze makkelijk kunnen waarnemen. Vervolgens proberen we deze informatie te generaliseren naar sterrenstelsels in het algemeen.

Iets dergelijks doen in wij in Hoofdstuk 4, waar we twee H ɪɪ gebieden in het dichtbijzijnde sterrenstelsel NGC 6822 bestuderen. We bestuderen en modelleren de H ɪɪ gebieden in het sterrenstelsel en gebruiken deze informatie om duizenden sterrenstelsel in het heelal te begrijpen. Eigenschappen van H ɪɪ gebieden, zoals leeftijd, straal of afmeting en dichtheid van het omliggende medium, zijn belangrijk om te begrijpen hoe hoge massa sterren hun omgeving beïnvloeden, welke mechanismen verantwoordelijk zijn voor de uitdijing van het geïoniseerde gas en de link tussen stervormende sterrenstelsels en individuele H ɪɪ gebieden. We selecteren twee H ɪɪ gebieden in het sterrenstelsel NGC 6822 die in het verleden uitgebreid zijn bestudeerd: Hubble V en Hubble X.

Sterrenstelsels op grote afstand

Licht heeft een constante snelheid. Het licht dat afkomstig is van sterrenstelsels die zeer ver weg staan, heeft daarom een lange tijd nodig om ons te bereiken. Deze sterrenstelsels zien wij daarom zoals zij waren toen het licht bij hen vertrok. Het is daardoor mogelijk om de geschiedenis van het heelal waar te nemen door naar deze sterrenstelsels te kijken. Door dit te doen kunnen wij veel leren over de formatie en evolutie van sterrenstelsels, een onderwerp waar veel sterrenkundigen een grote hoeveelheid tijd en energie in stoppen. Het begrijpen van de eigenschappen van sterrenstelsels die ver weg staan en het begrijpen van overeenkomsten en verschillen met lokale sterrenstelsels is essentieel om de evolutie van sterrenstelsels te begrijpen en verklaren.

In Hoofdstuk 5 en 6 doen we een poging om deze overeenkomsten en verschillen te begrijpen door middel van simpele principes en modellen. De verhoudingen tussen specifieke emissielijnen in het spectrum van een sterrenstelsel zijn hierbij belangrijke hulpmiddelen. De emissielijn ratios [O ɪɪɪ]/Hβ en [N ɪɪ]/Hα worden vaak gebruikt als een empirische methode om verschillende ionisatiemechanismen te kunnen onderscheiden. Bij de interpretatie van deze diagnostieken is het echter noodzakelijk om berekeningen te maken voor de interne structuur van de H ɪɪ gebieden. Deze berekeningen zijn op hun beurt weer afhankelijk van de aannames die gemaakt worden over de relatieve bijdrages van stralingsdruk en stellaire winden.

Wij maken modellen van individuele H ɪɪ gebieden zowel met als zonder stralingdruk en stellaire winden in Hoofdstuk 5. In Hoofdstuk 6 wordt vervolgens een populatie synthesecode beschreven die deze modellen gebruikt om een sterrenstelsel te simuleren met een verscheidenheid aan H ɪɪ gebieden met verschillende eigenschappen. We laten zien dat emissielijn ratios op sterrenstelsel niveau sterk afhankelijk zijn van de exacte waarden voor de verschillende bepalende parameters. In sommige gevallen zijn emissielijn ratios te produceren die voorheen gestelde theoretische limieten overschrijden.

Een stukje van de puzzel

Dit proefschrift, net als vele andere werken in de wetenschap, heeft niet de verwachting dat het alle grote onopgeloste vragen in de sterrenkunde op zal lossen. Tot de volgende Galileo, Newton of Einstein opstaat om de natuurkundewereld te revolutioneren zal een simpele astronoom, zoals ikzelf, de grote problemen moeten opbreken in kleine vraagstukken. Het is echter altijd van belang het grotere geheel te blijven zien. Daarom hier een aantal van de belangrijkste vraagstukken in de sterrenkunde die te maken hebben met dit werk. Hoe vormen sterrenstelsels zich en hoe evolueren ze zich naar wat wij nu waarnemen in onze directe omgeving? Hoe vormen sterren zich in een sterrenstelsel? Wat bepaalt de massa van sterren?

Meer specifiek gerelateerd aan het werk beschreven in dit proefschrift is de vraag hoe zware sterren zich vormen en hoe ze hun omgeving beïnvloeden gedurende de geschiedenis van het heelal. Mijn kleine bijdrage bestaat uit het bestuderen van sommige aspecten van deze kosmische stervorminggeschiedenis en de manier waarop zware sterren de evolutie van sterrenstelsels sturen. We analyseerden hiervoor optische waarnemingen van stervormende sterrenstelsel en bepaalden de fysische eigenschappen van het gas in H II gebieden rond massieve sterren. Ook hebben wij de dynamische uitdijing van de H II gebieden door stralingsdruk en stellaire winden op numerieke wijze gesimuleerd. We hebben vergelijkingen gemaakt tussen voorspellingen op basis van theorie en numerieke simulaties en waarnemingen van zowel H II gebieden en interstellaire bellen.

Modelli di bolle interstellari: vicino e lontano

La vita delle stelle

Le stelle sono gli elementi fondanti dell'universo. Contribuiscono alla maggior parte della luce che vediamo nel cielo stellato e sono raggruppate in galassie. Una galassia, come la nostra Via Lattea, contiene tipicamente cento miliardi di stelle e nell'universo sono presenti cento miliardi di galassie.

Le stelle sono sfere di gas tenuto insieme dalla forza di gravità. Ciascuna stella ha un proprio ciclo di vita: nasce ed evolve fino a che non arriva alla sua morte. Per la maggior parte della loro vita le stelle bruciano idrogeno nel loro interno per produrre energia che viene emessa come luce. La stessa luce che ci permette di vedere le stelle nel cielo stellato o che durante il giorno illumina e permette la vita sulla Terra. Gli astronomi classificano le stelle a seconda della loro massa, in quanto essa determina molte delle loro proprietà, come la durata della loro vita e l'evoluzione. Vengono raggruppate in stelle di piccola massa, più conosciute, e di grande massa, sulle quali abbiamo ancora molto da scoprire.

Stelle di piccola massa, come il nostro Sole, hanno una vita lunga e stabile che dura più di 10 miliardi di anni. Al contrario, le stelle massive, nonostante abbiano tanto più carburante da bruciare (possono avere da decine fino a centinaia di volte la massa del Sole) riescono a raggiungere un'età molto inferiore. Questo succede perché emettono molta più luce rispetto alle stelle di piccola massa bruciando il loro carburante energetico molto più velocemente. Il risultato è una vita di 'solo' qualche milione di anni.

Le stelle di grande massa ionizzano il gas presente nei loro dintorni creando un plasma che emette a lunghezze d'onda ultraviolette, infrarosso e radio. Inoltre durante la loro vita arricchiscono il mezzo interstellare (il materiale presente fra le stelle in una galassia) rilasciando materiale nei loro dintorni, prima attraverso forti venti stellari e alla fine del loro ciclo di vita con esplosioni di supernove. Le stelle di grandi massa e l'impatto che esse hanno nell'ambiente che le circonda sono il soggetto di questa tesi.

La nascita di una stella

Le stelle si formano da una nube tiepida di gas, chiamata *nube molecolare*, che consiste principalmente di idrogeno e una piccola quantità di molecole. Queste nubi molecolari sono supportate da forze termiche, di turbolenza o magnetiche che agiscono contro la forza di gravità, mantenendo la nube in uno stato di equilibrio. Quando questo equilibrio

viene a mancare a favore della gravità, si creano delle instabilità che innescano il collasso gravitazionale della nube.

Questo processo genera un nucleo di materia denso, dove la stella verrà a formarsi, che continua ad attrarre parte del gas circostante. Il restante materiale si distribuisce in un disco o viene espulso attraverso getti di gas perpendicolari a ciascuna faccia del disco. Una volta che il nucleo della stella ha raggiunto la densità necessaria ad iniziare la fusione dell'idrogeno nel suo centro, una nuova stella si è formata.

Questo scenario descrive gli stadi iniziali di evoluzione delle stelle di piccola massa, ma non è ancora chiaro se la stessa sequenza di eventi si applichi anche alle stelle di grande massa. A causa della loro breve vita e alla loro presenza in minor numero sono infatti più difficili da osservare e quindi da studiare e capire. Inoltre, quando nascono, si trovano al centro di una nube molto densa che non permette alla luce emessa dalla stella di passare, celandole alla nostra vista.

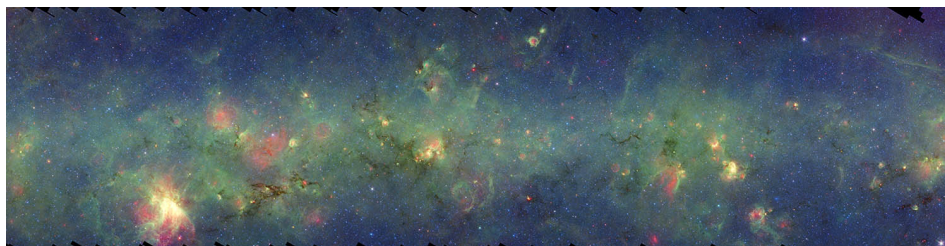## Regioni H II e bolle interstellari

Figura 1 – Immagine infrarossa di polvere e radiazione stellare dell'interno della Via Lattea. In blu PAH (IRAC 3.6 μm), in verde PAH (IRAC 8 μm), e in rosso grani di polvere caldi (MIPSGAL 24 μm). Crediti: NASA/JPL-Caltech/Univ. of Wisconsin.

Nonostante queste difficoltà, esiste uno stadio osservabile nella formazione delle stelle di grande massa, ovvero quando la stella nascente emette una frazione considerevole di fotoni ultravioletti ad alte energie capace di ionizzare una parte del gas circostante. Gli astronomi chiamano questo oggetto regione H II (pronunciato *regione acca secondo*). Queste regioni sono composte principalmente da idrogeno, pertanto il nome (il termine H II si riferisce all'idrogeno ionizzato: un atomo di idrogeno senza un elettrone), con una temperatura di circa 10,000 K. La luce emessa dalle regioni H II fornisce un indizio diretto sull'ambiente in cui stelle di grande massa di formano.

Oltre a ionizzare l'idrogeno (e altri elementi) nei loro dintorni, la radiazione ultravioletta proveniente dalla stella eccita gli idrocarburi policiclici aromatici (PAH, dall'acronimo inglese) rendendoli fluorescenti nell'infrarosso. I PAH sono molecole composte da atomi di carbonio legati in anelli esagonali organizzati in strutture a nido d'ape e circondati da atomi di idrogeno. La stessa radiazione scalda anche i grani di polvere (minuscole pezzi di particelle solide composte principalmente da carbonio, silicio e ossigeno) che a

loro volta irradiano l'energia assorbita a lunghezze d'onda maggiore. Entrambi PAH e polvere si trovano nel mezzo interstellare insieme all'idrogeno.

I risultati di questi processi fisici si possono ammirare nelle spettacolari immagini del piano galattico fatte dallo *Spitzer Space Telescope* (vedi Figura 1). Una caratteristica di rilievo è la complessità e varietà delle strutture presenti attorno alle stelle di grande massa. Mentre alcune regioni si presentano spazialmente estese e con morfologie complesse, altre sono più piccole con forme più regolari. Le regioni H II di cui parlavamo prima sono contenute dentro queste strutture tridimensionali che prendono il nome di bolle essendo vuote al centro. Grazie al *Milky Way Project*, un'iniziativa di partecipazione del pubblico nella ricerca scientifica, le bolle conosciute nell'infrarosso sono arrivate a circa 5100, un numero dieci volte maggiore rispetto a quelle precedentemente conosciute dagli astronomi.

Espansione di regioni H II come palloncini

Una delle domande a cui si cerca di dare una risposta in questa tesi riguarda l'evoluzione nel tempo delle regioni H II. L'espansione di una regione H II è simile al gonfiarsi di un palloncino: più aria si soffia nel palloncino, più esso cresce. In termini fisici, la pressione all'interno del palloncino aumenta rispetto all'ambiente. In maniera simile, una stella, aumentando la pressione nei suoi dintorni, accumula il gas circostante in un guscio che si espande (la bolla).
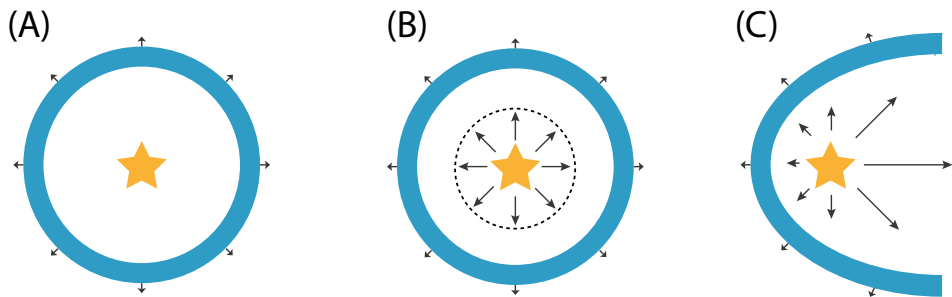

Figura 2 – Rappresentazione schematica di regioni H II: (A) dovute ad una sovrimpressione del gas ionizzato; (B) dovute ai venti stellari; e (C) in presenza di un gradiente di densità nel mezzo (chiamato modello a flusso di champagne). Crediti: Bram Ochsendorf.

L'origine di tale incremento di pressione intorno alla stella è ancora in discussione. Secondo alcuni è la conseguenza diretta della sola radiazione della stella, mentre altri dicono che sia dovuto ai venti stellari. In Figura 2 vengono mostrate, in maniera schematica, le possibili soluzioni proposte negli anni per spiegare la fisica delle regioni H II. Se il gas che circonda la stella è omogeneo, la forma della regione H II risulterà sferica; come nei casi (A) e (B) di Figura 2. (A) mostra il caso più semplice in cui la stella ionizza il mezzo attorno ad essa. Il gas ionizzato, essendo a temperature e pressione maggiore rispetto all'ambiente circostante, si espande. Tale espansione avviene sotto forma di un

fronte d'onda che spazza il materiale circostante. (B) mostra la struttura di una regione H II in presenza di un vento stellare. La velocità del vento è circa 2000 km s^{-1}. Una velocità così alta crea un secondo fronte d'onda all'interno della regione H II. (C) illustra il caso in cui il mezzo interstellare ha un gradiente di densità (la densità è maggiore in una direzione rispetto alla stella e diminuisce gradualmente verso l'altra). In questo caso, la regione H II non è più sferica ma ha una forma simile ad una cometa (tipo paraboloide). Il gas all'interno della regione H II viene rilasciato verso l'apertura, dando il nome modello a flusso di champagne.

Regioni H II UltraCompatte

Il primo stadio di evoluzione di una regione H II viene chiamato UltraCompatto. Il Capitolo 2 di questa tesi si basa su uno studio di questi oggetti. Analizzando in dettaglio la regione H II G29.96-0.02, creata da un vento stellare esaminando la mancanza di emissione di raggi X. Osservazioni dell'emissione di raggi X e dello spettro della stella vengono usate come parametri per la creazione di modelli idrodinamici con lo scopo di capire la fisica di queste regioni. Questi modelli includono gli effetti dovuti alla foto-ionizzazione del mezzo interstellare, al vento stellare, ai processi radiativi, all'iniezione di massa e all'onda d'urto dovuta al movimento della stella.

I nostri risultati mostrano che i modelli a flusso di champagne sono i migliori per spiegare la morfologia e la dinamica del gas. Inoltre, l'iniezione di massa nel gas caldo è necessaria per raffreddare il gas fino alle temperature osservate nei raggi X.

Regioni H II polverose

Nel Capitolo 3 presentiamo una classe di regioni H II che si formano secondo il modello a flusso di champagne. Il nostro scopo è spiegare la forma ad arco dell'emissione dei grani di polvere osservata all'interno delle regioni H II. Proponiamo che questa struttura osservata a 24 μm sia il risultato dell'interazione fra la pressione di radiazione dalla stella con la polvere contenuta nel flusso di gas ionizzato, chiamiamo questa struttura *onda di polvere*. Mostriamo che nel caso del modello a flusso di champagne il gas ionizzato raggiunge velocità grandi abbastanza per creare le condizioni adatte alla formazione di una *onda di polvere*. Tali modelli riescono anche a riprodurre la varietà di morfologie di regioni H II osservate e i tipici profili di emissione.

Da stelle a galassie

Le galassie sono composte da miliardi di stelle. Esistono due tipi principali di galassie, ellittiche e a spirale. In questa tesi prendiamo in analisi le galassie a spirale in quanto formano continuamente stelle, per questo vengono chiamate in inglese galassie *star-forming*. Siccome le stelle di grande massa hanno una vita breve, è importante che siano in formazione continua in una galassia per poterle osservare e studiare. La Figura 3 mostra M51, una tipica galassia a spirale. È composta da un centro (detto *bulge*) e da un disco in cui
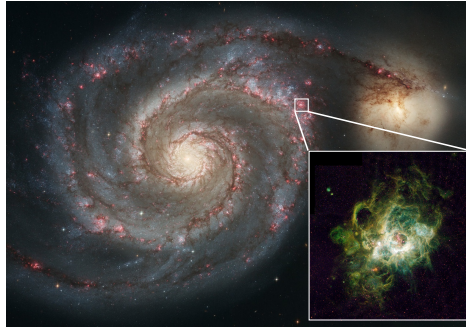
Figura 3 – Composizione artistica della relazione fra una galassia a spirale e una regione H II. La galassia a spirale sullo sfondo è M51, le zone in rosso sono regioni H II. L'immagine piccola è NGC 604, una regione H II gigante in M33.

si estendono i bracci di spirale. Lungo i bracci di spirale ci sono numerose stelle in formazione e molte regioni H II. Nella stessa figura c'è anche NGC 604, una una regione H II gigante in M33, un'altra galassia più vicina a noi. Lo zoom della figura non è reale, ma dà un'idea della relazione fra una galassia a spirale e una regione H II e delle loro grandezze. Le regioni H II sono responsabili della maggior parte della luce proveniente da galassie *star-forming*. Essendo la maggior parte delle galassie molto lontane da noi è impossibile risolverle come in Figura 3 e appaiono quindi come delle macchie di luce. Per capire le caratteristiche principali delle galassie è importante studiare regioni H II nella nostra galassia e in galassie vicine, estrapolando le informazioni trovate localmente ai casi lontani.

Nel Capitolo 4 prendiamo in esame due regioni H II in NGC 6822, una galassia vicina. Le osservazioni e i modelli di queste regioni possono essere utilizzate per capire milioni di galassie nell'universo. Le informazioni che deriviamo sono delle proprietà fisiche, come l'età, la dimensione e la densità dell'ambiente. Questi parametri sono importanti per capire l'interazione delle stelle di grande massa con il loro ambiente, i meccanismi di espansione del gas ionizzato e il collegamento fra galassie *star-forming* e regioni H II.

Galassie lontane

Poiché la luce viaggia a una velocità costante, la luce proveniente da galassie molto lontane impiega molto tempo a raggiungerci. Osservare queste galassie lontane significa quindi guardare indietro nel tempo e vedere la storia dell'universo. È così che gli astronomi studiano la formazione ed evoluzione delle galassie, un argomento molto caro agli scienziati. È quindi cruciale per spiegare l'evoluzione delle galassie capire le proprietà delle galassie lontane e paragonarle a quelle vicine individuando somiglianze e differenze.

Nei Capitoli 5 and 6 cerchiamo di studiare queste somiglianze e differenze usando dei principi e dei modelli semplici. I rapporti di emissione di linee, quali [O III]/Hβ and [N II]/Hα, vengono adottati in maniera empirica per distinguere diversi meccanismi

di ionizzazione nelle galassie. Tuttavia, per avere un'interpretazione dettagliata di questi diagnostici sono necessari dei calcoli che tengano in considerazione la struttura interna delle regioni H II. I risultati cambiano a seconda delle assunzioni fatte sull'importanza relativa della pressione di radiazione e dei venti stellari all'interno delle regioni H II. Abbiamo, quindi, costruito dei modelli di regioni H II includendo ed escludendo la pressione di radiazione e i venti stellari. Inoltre, utilizzando un codice che genera popolazioni sintetiche di regioni H II abbiamo creato delle galassie che possono essere confrontate con le osservazioni.

Da questa analisi possiamo concludere che la scelta dei parametri fisici ha un ruolo principale nel determinare il valore finale dei rapporti delle linee di emissione.

Un passo più vicini per risolvere il grande puzzle

Questa tesi, come ogni altro lavoro scientifico, non ha alcuna aspettativa di risolvere tutte le grandi domande ancora irrisolte in astronomia. Aspettando che arrivi il prossimo Galileo, Newton o Einstein a rivoluzionare il mondo della fisica, un semplice astronomo, come me, deve essere in grado di dividere i grandi problemi in piccoli lavori. È comunque importante avere in mente il grande puzzle. Ecco le grandi domande dell'astronomia moderna collegate a questo lavoro: come si formano le galassie e come si sviluppano fino a diventare le galassie che osserviamo oggi? Come si formano le stelle nelle galassie? Cosa ne determina la loro massa?

Questo lavoro mira, in maniera più specifica, a capire la formazione di stelle di grande massa e la loro influenza sull'ambiente circostante durante l'evoluzione dell'universo. Il mio piccolo contributo consiste nello studio della storia della formazione stellare e nel modo in cui stelle di grande massa determinano l'evoluzione delle galassie. In particolare, ho analizzato osservazioni ottiche di galassie *star-forming* derivando le condizioni fisiche del gas nelle regioni H II associate con stelle di grande massa. Inoltre, ho simulato numericamente l'espansione dinamica delle regioni H II dovuta a venti stellari e alla sovra-pressione del gas ionizzato. Infine ho paragonato varie teorie con osservazioni di regioni H II e bolle interstellari per determinare quale sia più appropriata a descrivere questi oggetti.

Publications

1. *Line Emission from Radiation-Pressurized H II Regions*
   I: Internal Structure and Line Ratios
   S. C. C. Yeh, **S. Verdolini**, M. R. Krumholz, C. D. Matzner,
   A. G. G. M. Tielens
   2013, ApJ, 769, 11

2. *Line Emission from Radiation-Pressurized H II Regions*
   II: Dynamics and Population Synthesis
   S. Verdolini, S. C. C. Yeh, M. R. Krumholz, C. D. Matzner,
   A. G. G. M. Tielens
   2013, ApJ, 769, 12

3. *X-ray emission from stellar wind driven bubbles: An observational and theoretical*
   study of the prototypical UltraCompact H II region, G29.96-0.02
   S. Verdolini, M. Raicevic, F. Tramper, A. Bik, A. de Koter, L. K. Townsley, P. S.
   Broos, E. D. Feigelson, A. G. G. M. Tielens
   to be submitted

4. *A study of H II regions in NGC6822 and the distribution of SDSS starforming galaxies*
   in the emission line diagnostic diagram
   S. Verdolini, L. R. Carlson, S. C. C. Yeh, M. Galametz, V. Lebouteiller, J. Brinch-
   mann, A. G. G. M. Tielens
   to be submitted

5. *Radiation pressure-driven dust wave inside bursting interstellar bubbles*
   B.B. Ochsendorf, **S. Verdolini**, N.L.J. Cox, O. Berné, L. Kaper,
   A. G. G. M. Tielens
   to be submitted

6. *A class of champagne flow bubbles with radiation pressure-driven dust wave*
   S. Verdolini, B.B. Ochsendorf, A. G. G. M. Tielens
   to be submitted

Curriculum Vitae

I was born on May 7, 1984. I was raised in the beautiful countryside around the little town Cupramontana (Ancona, Italy). I went to the Liceo Scientifico Leonardo da Vinci in Jesi, where I realized that physics and math were fun.

In 2003 I began my bachelor study in astronomy at Università di Bologna (Laurea Triennale). In the summer of 2006 I graduated with a thesis on analytical studies of self-similar fluids. The following fall I began a Master degree (Laurea Specialistica) in astrophysics and cosmology at the same university. In 2007 I won a merit-based selection to study abroad, and spent the second year of the Master at University of California Santa Cruz. There I finished the compulsory courses, worked on my thesis of planet formation with Prof. Doug Lin, and learned how to surf. In March 2009 I received my degree at Università di Bologna.

In late 2009, I started a PhD in astronomy at the Sterrewacht Leiden (Leiden University) under supervision of Prof. A. G. G. M. Tielens. My research has been dedicated to the twofold investigation of the interaction of massive stars with their surroundings: I have analyzed observations of emission lines in H II regions to determine the physical conditions surrounding the formation of massive stars both in the near and far Universe; and I have studied the hydrodynamical evolution of these regions numerically. I developed and tested a radiative transfer code as implemented in the hydrodynamic code FLASH. I used the code to study the hydrodynamical evolution and resulting X-ray emission of a prototypical UltraCompact H II region.

During my PhD I participated in the NOVA fall school (Dwingeloo) and I spent the summer of 2010 at the ISIMA Summer School in Santa Cruz where I worked with Prof. dr. M. Krumholz, this resulted in two chapters for this thesis and inspiration for a third. I presented my research at international conferences in the Netherlands, Switzerland, Italy, and United States.

Ringraziamenti

It has been four terrible, yet fantastic, years! An incredible journey that thought me a lot – not just astronomy, luckily – and made me a better person (I hope). If I can say *I am done*, it is only thanks to the support of many people. All of you helped. Thanks!

All of this would not have been possible without Xander. Thanks for the encouragement and the enthusiasm for science. Thanks to the ISM group. In particular, I thank Alessandra for the many good advises, Lynn for the hard work we did together, and Francisco for constantly explaining observations to me. I would like to thank Chael for the great support he gave me in the first year of PhD. Thanks to Milan for guiding me through the intricacies of a code too big and complex for me to understand.

Once again, in the process of moving around the world, I found real friendship. I have never felt lonely from the first day I was in the Netherlands. Thanks Carina for your contagious laugh and for your unlimited energy and wisdom. Ernst, it is my time now to say that you are awesome! Thanks for keeping the promise we would stay in touch. Niruj, when you left there was a huge emptiness around. Thank you for unforgettable day you took me shopping in Amsterdam.

Un ringraziamento specialissimo alla mia "famiglia" a Leiden. Irene, grazie per il supporto in tutte quelle giornate da *goma del butano*, grazie per le passeggiate all'undicesimo piano e grazie per riuscire sempre a farmi ridere! Matteo, grazie per avermi insegnato l'estetica del plot e grazie per non esserti mai arrabbiato delle mie battute. Nicola, grazie per tutte quelle volte (tante) che sono entrata nel tuo ufficio con un problema numerico e ne sono uscita con una soluzione. Grazie per avermi ascoltata, capita ed essermi stato accanto in momenti difficili. Grazie ragazzi, per le *movies nights*, per i *birra crucis*, per le serate passate insieme a chiacchierare, e per tutti i momenti indimenticabili degli ultimi anni.
Thanja, thanks for dragging me to the gym, for the chats, and for sharing your cooking passion with me! Ringrazio Fabio per aver condiviso con me il suo hobby in numerose occasioni! Ringrazio Alessandra per le torte e per le giornate di shopping. Ringrazio Marco per il *better green*. Berenice and Mattia, thanks for the microwaves! Pedro, thanks for introducing me to the fascinating world of outreach. Jaya, thanks for the yummy Indian food and for your positive energy. Carolina, Kevin, and Xavier, each time you visit you bring sunshine with you!

Sahar, most of this thesis is your "fault", I guess I should thank you for it. You are like a sister. Even if so far away, you are always with me. Thank you for constantly encouraging me.

Un grazie di cuore a tutti coloro che mi sono venuti a trovare nella fredda Olanda in questi quattro anni e ai tanti che verranno per vedermi diventare dottoressa. Grazie mille a tutti! Madda, Giacomo e Andrea, grazie mille per esserci da sempre!

Grazie di cuore alla mia famiglia. Babbo, mamma, Giulia, questa tesi è per voi. Siete la mia forza. Grazie per avermi rimesso in piedi più di una volta. Non sarei mai riuscita a finire questa tesi se non avessi avuto la certezza di trovarvi sempre al mio fianco. Grazie ai nonni, agli zii, ai cugini, al nipotino più bello che ci sia e a quello che verrà.